SEARCH FOR RANDALL-SUNDRUM GRAVITONS IN DILEPTON AND DIPHOTON FINAL STATES WITH 1 fb^{-1} OF DATA

AMITABHA DAS

Dissertation submitted in partial fulfillment
of the requirements for the degree of
Doctor of Philosophy

BOSTON
UNIVERSITY

BOSTON UNIVERSITY

GRADUATE SCHOOL OF ARTS AND SCIENCES

Dissertation

SEARCH FOR RANDALL-SUNDRUM GRAVITONS IN DILEPTON AND DIPHOTON FINAL STATES WITH 1 fb^{-1} OF DATA

by

AMITABHA DAS

B.Sc., Presidency College, University of Calcutta, India
M.Sc., Presidency College, University of Calcutta, India

Submitted in partial fulfillment of the

requirements for the degree of

Doctor of Philosophy

2008

Approved by

First Reader

Ulrich Heintz
Associate Professor of Physics

Second Reader

Edward T. Kearns
Associate Professor of Physics

DEDICATION

To my daughter Devina.

Acknowledgments

This thesis is the end of a long journey and it is my pleasure to thank all the people who have made this journey possible.

First and foremost, I would like to thank my supervisor and thesis advisor, Prof. Ulrich Heintz. I attribute my degree to his continuous support and guidance from the very early stage of the research till the completion of the thesis. Working with him was an invaluable learning experience for me. His ability to approach any physics problem in various possible ways always fascinated me. His enormous enthusiasm and the thirst to achieve a goal worked as a driving force for me and enriched me as a student, a researcher and a scientist. It is needless to mention the various aspects of high-energy physics that I learned from him. However, the most valuable lesson that he taught me is the value of hard work.

I would also like to express my gratitude to my high school mathematics teacher Sudhanya babu. He may not be aware of this but he has a very big influence on me. I am also thankful to everyone at the Physics department of University of Oklahoma. My experience as a student in that university played an important role in shaping my career.

I really appreciate all the help and advice that I got from Prof. Meenakshi Narain and Prof. John Butler. I have been blessed with a friendly and helpful group of fellow members of the BU group. Lorenzo and Lars spent a lot of their valuable time to help me learn the D0 software. Kevin helped me immensely with STT and was always there to clarify things whenever I had any doubt. I would also like to mention Jason, Dan, Dookee, Shabnam, Vivek, Samvel, Norik and Monica. Thank you all.

It was an enjoyable experience to work with the members of the STT group as well - Tulika, Sinjini, Huishi, Ken, David, Ashish and Junjie. My sincere thanks to you, too.

I would like to thank Arnd Meyer, Greg Landsberg and Dmitri Denisov for their guidance and suggestions. I was also fortunate to have Junjie who was always available to help and answer my questions. My sincere thanks goes to the NP group conveners J.F. Grivaz and Yurii and all in the NP group who have sent their valuable comments on this work, to

the members of my EB - Michel Jaffre, Amber Boehnlein, Ray Hall, Bob Kehoe and Eric Varnes and also to Prof. Ed Kearns for being my second reader and for all his valuable comments.

I would also like to mention some friends whom I met in these years - Xiabo, Wei, Alfonso, Pradeep, Samit, Kaushik at BU and Dhiman Chakraborty, Sudeshna Banerjee, Subhendu, and Prolay at Fermilab. I would specially mention Nirmalya Parua whom I am fortunate enough to have as a friend and guide. Also many thanks to my friend Santosh Rai who spent lot of his valuable time to explain the theory.

I am also fortunate to come from a family where I was given the freedom to choose my career and always got love, support and encouragement. I express my sincere gratitude to my mother, Dr. Reba Dasgupta, my father, Dr. Manas Mohan Das, my sister and my extended family.

I am also very fortunate to have my wife Rituparna beside me during the ups and downs of my graduate student life. She was always there to support me and boost my moral. One of the best experiences that we lived through in this period was the birth of our daughter, Devina, who provided another joyful dimension to our life.

SEARCH FOR RANDALL-SUNDRUM GRAVITONS IN DILEPTON AND DIPHOTON FINAL STATES WITH 1 fb^{-1} OF DATA

(Order No.)

AMITABHA DAS

Boston University, Graduate School of Arts and Sciences, 2008

Major Professor: Ulrich Heintz, Associate Professor of Physics

ABSTRACT

The work presented in this thesis is the search for Randall-Sundrum (RS) gravitons from an analysis of approximately 1 fb^{-1} data collected with the DØ detector at Fermilab.

The standard model has been a great success in explaining all experimental observations in particle physics. However, we also know that it has fundamental problems. One of these problems, called the hierarchy problem, is related to the large difference between the electroweak scale and the Planck scale.

The model proposed by Randall and Sundrum presents a possible solution to the hierarchy problem by introducing physics beyond the standard model. Randall and Sundrum's theory postulates the existence of a 4th spatial dimension in addition to the conventional (3+1)-dimensional space. Gravity is localized on a 3+1 dimensional subspace, called a brane (Planck brane) that is separated in this new 4th spatial dimension from the standard model brane. As one moves away from this Planck brane, gravity is exponentially suppressed and this explains why gravity appears so weak at the standard model brane.

In the simplest RS model, the only particles that propagate in the extra dimension are gravitons. The graviton manifests itself on the standard model brane as a series of excited states that couple to standard model particles with similar strength as the electroweak interaction. The ground state is the massless graviton and the order of magnitude of the mass of the lowest excited state is expected to be one TeV. The first excited mode of the graviton might be produced resonantly at the Tevatron. Gravitons can decay into fermion-antifermion or diboson pairs. Here I search for gravitons through their decay to e^+e^- and $\gamma\gamma$ final states. These final states have similar signatures in our detector and can thus be treated together. After analyzing the data I do not find any excess over standard model expectations and set an upper limit on the production rate of such gravitons. I compare this limit to the production rate predicted by the theory for a range of possible couplings and set mass limits on the lowest excited gravitons state of up to 898 GeV.

Contents

List of Tables

List of Figures

List of Abbreviations

ADC	....	Analog to Digital Converter
CC	....	Central Calorimeter
CDF	....	Collider Detector at Fermilab
CFT	....	Central Fiber Tracker
CH	....	Coarse Hadronic
CP	....	Charge and Parity
CPF	....	Central Preshower
DAQ	....	Data Acquisition
DY	....	Drell-Yan
EC	....	End Calorimeter
EM	....	Electromagnetic
EMF	....	Electromagnetic Fraction
eV	....	Electron Volt
FAMUS	....	Forward Angle Muon Spectrometer
FH	....	Fine Hadronic
FPS	....	Forward Preshower
GeV	....	Giga-Electron Volts (10^9 Electron Volts)
Hz	....	Hertz($\frac{1}{\text{second}}$)
KHz	....	Kilo-Hertz(10^3 Hertz)
KK	....	Kaluza-Klein

LHC	Large Hadron Collider
L1FW	Level 1 Framework
LINAC	Linear Accelerator
LO	Leading order
L1	Level 1
L2	Level 2
L2CAL	Level 2 Calorimeter Trigger
L3	Level 3
MC	Monte carlo
MeV	Mega-Electron Volt(10^6 Electron Volts)
MHz	Mega-Hertz (10^6 Hertz)
NLO	Next to leading order
QED	Quantum Electrodynamics
QCD	Quantum Chromodynamics
RS	Randall-Sundrum
SM	Standard Model
SMT	Silicon Microstrip Tracker
VLPC	Visible Light Photon Counter
WAMUS	Wide Angle Muon Spectrometer

Chapter 1

INTRODUCTION AND PHENOMENOLOGY

The quest of mankind to understand the universe has a long history. We try to understand and explain different aspects of the nature that surrounds us. Particle physics is a discipline where we try to find the answer to the most fundamental question: What is the universe made of? What are the forces that bind it together? We have come a long way in answering many such questions and at present we have the knowledge and understanding, supported by experimental proof, to describe the physical world in terms of the most fundamental building blocks of nature. Most of the advances in the field of particle physics was achieved in a short span of time, primarily in the last century. However we can not claim to have a full understanding yet and scientists are still working for better understanding.

1.1 The Standard Model

The Standard Model (SM)(1)(2)(3) is the theoretical basis of modern particle physics. It was formulated by S.L.Glashow(1961), S.Weinberg(1967) and A.Salam(1969) (4) and since then this model withstood almost four decades of experimental tests. The Standard Model gives a very good description of all currently observed phenomena at the distance scales of $\sim 10^{-18}$m.

According to the Standard Model, our universe is made of two classes of fundamental particles: the spin 1/2 fermions, which are the building blocks of matter, and the spin 1 gauge bosons, which are the carriers of different forces between the fermions. All the different fermions are listed in Table 1.1. As shown in the table the fermions are grouped in three generations. The particles in the first generation, including electron, up and down quarks, constitute all the ordinary matter that we are familiar with. The two other

Generation	Leptons (spin=$\frac{1}{2}$)			Quarks (spin=$\frac{1}{2}$)		
	Flavors	Charge (e)	Mass (MeV)	Flavors	Charge	Mass (MeV)
1	e	-1	0.511	u	$+2/3$	~ 3
	ν_e	0	$< 3 \times 10^{-6}$	d	$-1/3$	~ 5
2	μ	-1	105.7	c	$+2/3$	$\sim 1.2 \times 10^3$
	ν_μ	0	< 0.19	s	$-1/3$	~ 100
3	τ	-1	1777	t	$+2/3$	$\sim 178 \times 10^3$
	ν_τ	0	< 18.2	b	$-1/3$	$\sim 4.5 \times 10^3$

Table 1.1: Three generations of elementary particles.

generations are replications of the first generation but with higher masses. The fermions are further classified into leptons and quarks. There are two fundamental differences between the quarks and the leptons.

- quarks carry fractional charges unlike the leptons
- only quarks feel the strong interaction

In the Standard Model, there are three types of forces: strong force, electromagnetic force and weak force. The interaction between two particles is viewed as a process in which these two particles exchange a virtual gauge boson. In Table 1.2, the different forces, their carriers and some of their properties are listed.

Force	Gauge Boson	Charge (e)	Spin	Mass (GeV)	Range
Strong	Gluon (g)	0	1	0	$10^{-15}m$
Electromagnetic	Photon(γ)	0	1	0	∞
Weak	$W^\pm$	±1	1	80.4	$10^{-18}m$
	Z^0	0	1	91.2	
Gravity	Graviton (G)	0	2	0	∞

Table 1.2: Fundamental forces and gauge bosons.

The photon is the carrier of the electromagnetic force. The electromagnetic interactions are described by the theory of quantum electrodynamics (QED). These interactions take place between electrically charged particles. Since the photon is massless, the electromagnetic interaction is long range and falls off as $\frac{1}{r^2}$.

The weak interactions are mediated by three massive gauge bosons, $W^{\pm}$ or Z^0. Since these gauge bosons are massive ($\sim$ 100GeV), the weak interactions have short range. In the Standard Model, the electromagnetic and weak interactions have been unified and are together known as 'Electroweak' interactions.

The mediator of the strong interactions is the gluon and these interactions are described by Quantum Chromodynamics (QCD). Analogous to the electromagnetic force, which couples with electrically charged particles, the strong force couples with 'color' charged particles. There are three types of color charges: red(r), green(g) and blue(b) and the corresponding anti-color charges $\overline{r}$, $\overline{g}$ and $\overline{b}$. Unlike the photons, which themselves do not carry any electrical charge, the gluons carry color charge and hence can interact with each other through the strong force. This is the reason for the strong interaction to be short ranged and this also leads to the phenomenon of confinement of quarks into hadrons. Because of this individual quarks are not seen in nature. At large interaction energies between the quarks (typical of modern high energy experiment with E$\sim$10GeV) the quarks behaves like free particles but only inside hadrons - thus asymptotically free and not really free. This is known as "asymptotic freedom".

The quarks that are created in high energy collisions do not remain free for a very long time. Within a time scale typical of strong interactions ($\sim 10^{-24}$ s), quark anti-quark pairs are pulled out of the vacuum which bind with the quarks from the hard scattering to form composite particles. This process is referred to as fragmentation and hadronization. As a result, although quarks and gluons are produced due to hard scattering, the experimenters can only look at the composite hadrons.

The other force in nature is the gravitational force. The graviton is the mediator of the gravitational force. The Standard Model does not include gravity.

Apart from the fermions and bosons listed in Table 1.1 and Table 1.2, there is one more particle predicted by the Standard Model: the Higgs particle which is associated with the

Higgs field, discussed in section 1.2.

Finally, the SM depends on 21 parameters which are 3 gauge couplings, 2 parameters which determine the mass and self-interactions of the Higgs bosons, the 9 quark and charged lepton masses, 3 quark mixing angles, 1 weak CP violating phase δ, 1 strong CP violating parameter θ_{QCD}, the analogous parameter of SU(2) and the electroweak mixing angle θ_w.

1.2 Spontaneous Symmetry Breaking

The Standard Model is developed on the principles of least action and local gauge invariance. In this model, the Lagrangian of the matter fields is required to be invariant under local gauge transformations. Each type of interaction (strong, weak or electromagnetic) corresponds to a particular type of gauge transformation and hence forms a mathematical group or gauge group. In the Standard Model, the electromagnetic and weak interactions are combined under $\mathrm{SU}(2)_L \times \mathrm{U}(1)_Y$ group. The $\mathrm{SU}(2)_L$ group corresponds to the conservation of the weak isospin quantum number T_3. $\mathrm{U}(1)_Y$ represents the conservation of weak hypercharge quantum number Y. These quantum numbers are related to the electric charge Q as :

$$Q = T_3 + \frac{1}{2}Y. \tag{1.1}$$

This $\mathrm{SU}(2)_L \times \mathrm{U}(1)_Y$ gauge theory results in massless gauge fields, namely the weak isotriplet W^i_μ with i=1,2,3 for $\mathrm{SU}(2)_L$ and the hypercharge boson singlet B_μ for $\mathrm{U}(1)_Y$. The unified electroweak theory thus requires all of the four gauge bosons to be massless, which is ruled out by experiment and we know that the weak gauge bosons, $\mathrm{W}^\pm$ and Z, are massive.

The SM explains this by the Higgs mechanism and one of the most important ingredients of this mechanism is the concept of spontaneous symmetry breaking. As a simple example we can consider a theory with one scalar field governed by the Lagrangian:

$$L = \frac{1}{2}(\partial^\mu \phi)(\partial_\mu \phi) - \frac{1}{2}\mu^2\phi^2 - \frac{\lambda}{4}\phi^4. \tag{1.2}$$

This Lagrangian is symmetric under the transformation:

$$\phi \to -\phi. \tag{1.3}$$

This produces a discrete symmetry group. However if we now look at the potential which is given by:

$$V(\phi) = \frac{1}{2}\mu^2\phi^2 + \frac{1}{4}\lambda\phi^4, \tag{1.4}$$

for λ >0 and μ^2 <0, it gives two minima at:

$$\phi_{min} = \pm\sqrt{\frac{-\mu^2}{\lambda}}. \tag{1.5}$$

This phenomenon, when the ground state is not invariant under a symmetry of the Lagrangian, is called spontaneous symmetry breaking. In Higgs mechanism, a scalar field, called Higgs field, is introduced which leads to a non-zero vacuum expectation value and spontaneously breaks the SU$(2)_L$ × U$(1)_Y$ symmetry to U$(1)_{EM}$ symmetry. The weak gauge bosons related to the SU$(2)_L$ symmetry aquire mass as a consequence of the broken symmetry. However, the U$(1)_{EM}$ symmetry is not broken and hence photon is massless.

1.3 Problems with the Standard Model

All the particles in the Standard Model have been observed experimentally, except the Higgs particle. Despite the success of the Standard Model, it is still not a complete theory of fundamental particles and interactions. The Standard Model still leaves us with many unresolved theoretical issues. Some of these issues are:

- why do all the particles have charges which are multiples of e/3, where 'e' is the charge of an electron?
- what is the role played by the heavier copies of the first generation fermions?
- there are too many arbitrary parameters in the theory.
- gravity is not included in the Standard Model.

As mentioned earlier, the Standard Model proposed the Higgs mechanism. For this model to be consistent, the Higgs mass should be < 1 TeV. This constraint on the Higgs mass is due to the fact that if the Higgs mass is too heavy, its self coupling becomes strong and then the theory no longer remains perturbative. A detailed discussion on the contraints on Higgs mass can be found in reference (5). However, the tree-level Higgs mass receives quadratically divergent corrections. The Higgs mass is expressed by(6) :

$$M_H^2 \sim \left(M_H^{bare}\right)^2 + \frac{\lambda}{4\pi^2}\Lambda^2 + \delta M_H^2 \tag{1.6}$$

Here M_H^{bare} is the tree level (or 'bare') Higgs mass, Λ is the cutoff for the theory and δM_H^2 is the mass counterterm. Now if the Standard Model is the ultimate theory including gravity then the cutoff $\Lambda = M_{Pl} \sim 10^{16}$ TeV ($M_{Pl}-$Planck scale) and the natural scale for the Higgs mass is of the order 10^{16} TeV. However such a high mass Higgs makes the Standard Model internally inconsistent. In order to bring down the Higgs mass within the allowed Higgs mass region (< 1 TeV), cancellation of this quadratic divergence is required. In the Standard Model framework, where there is no new physics, this cancellation is accidental. This is regarded by most theorists as unacceptable fine tuning of parameters, also known as the 'fine tuning problem'. The origin of this problem is the large difference between the electroweak scale (~ 1 TeV) and the Planck scale ($\sim 10^{16}$ TeV). This is known as the 'hierarchy' problem.

1.4 Beyond the Standard Model

There are different theoretical models that extend beyond the Standard Model and try to address the different physics issues mentioned in section 1.3. The problem that is relevant to the topic of this thesis is the 'hierarchy' problem. Recently theories with extra dimensions have attracted enormous attention as possible solutions to the hierarchy problem.

1.4.1 Idea of Extra Dimensions

The idea of extra dimensions originates from superstring theories which include extra dimensions, the basic idea being that the extra dimensions are compact. For example, an extra dimension can be finite so that travelling along this dimension brings us back to our original locations, as travelling around a circle would. This means that at every point in spacetime, there exists an additional circle of radius R_c, orthogonal to all the four spacetime dimensions. One important consequence of this compactification is the quantization of the momentum component along the extra dimension. For the above example of one extra dimension, the volume of the extra dimension is $2\pi R_c$ and so all the wavefunctions should be periodic under $y \to y + 2\pi R_c$:

$$\Phi(x^\mu, y) = \frac{1}{\sqrt{2\pi R_c}} \sum_{n=-\infty}^{n=\infty} \phi_n(x^\mu) e^{\frac{iny}{R_c}}. \tag{1.7}$$

Now this five-dimensional massless field satisfies the Klein-Gordon equation:

$$\Box_5 \Phi(x^\mu, y) = (\partial_t^2 - \nabla^2 - \partial_y^2)\Phi(x^\mu, y) = 0. \tag{1.8}$$

Combining these two equations we get:

$$(\partial_t^2 - \nabla^2 + \frac{n^2}{R_c^2})\Phi(x^\mu) = 0. \tag{1.9}$$

This is a Klein-Gordon equation for a scalar field with mass $M_n = n/R_c$. Here ‘n’ is the discrete quantum number corresponding to the quantized momentum in the compactified fifth-dimension. This gives us an example of a ‘Kaluza-Klein reduction’(7). The ideas of compactification and Kaluza-Klein reduction form the basis of all extra dimension models.

1.4.2 The Large Extra Dimension Model

In recent years, a new type of model with extra dimensions, called the “Large Extra Dimension” model, has been pioneered by N. Arkani-Hamed, S. Dimopoulos and G. Dvali (ADD model)(8). According to this model there is a (1+3+d)-dimensional spacetime (bulk) and the Standard Model fields are confined on a (1+3)-dimensional subspace of this bulk. The d extra dimensions are compactified, typically on a d-torus of radius R_c. The gravitational field can propagate in this d-dimensional bulk. When the higher dimensional theory is matched with the 4-dimensional effective theory, the following relation is obtained:

$$M_{Pl}^2 = M_*^{d+2} V_{(d)} = M_*^{d+2} (R_c)^d. \tag{1.10}$$

Here, M_* is the fundamental Planck scale in the bulk, M_{Pl} is the observed (3+1)-dimensional Planck scale ($\sim 10^{16}$TeV) and $V_{(d)}$ is the volume of the extradimensional space. From this we get

$$R_c \sim \frac{1}{M_*} \left(M_{Pl}/M_*\right)^{2/d}. \tag{1.11}$$

Assuming that the fundamental Planck scale $M_* \sim 1$TeV, we get different values for the radius R_c corresponding to different values for the number of extra dimensions ‘d’. For d=1 we get a radius $R_c \sim 10^8$km. An extra dimension of this size would modify Newtonian gravity at astronomically observable distance scale. This is not the case and therefore the number of extra dimension d=1 is ruled out. For d=2, we get $R_c \sim 1$ mm and some recent experiments have produced tighter limit on the radius upto 160 μm(9). However, for $d \geq 3$ the radius $R_c < 0.1\mu$m, a distance scale not probed by experiments based on Newtonian gravity and where we expect to see the effect of extra dimension. Hence, with $d \geq 3$, the hierarchy problem is resolved by bringing down the cutoff value for the Standard Model to the TeV scale. However, there are some drawbacks of this model. One of them is that quantum corrections shrink the radius of the extra dimension (R_c) resulting in the fundamental Planck scale M_* to go up, which brings us back to the original problem(10).

1.4.3 The Randall-Sundrum Graviton Model

The Randall-Sundrum (RS) model, proposed by Lisa Randall and Raman Sundrum in 1999(11) has evolved out of the Large Extra Dimension model. It is an alternate approach, based on the idea of extra dimensions, to address the hierarchy problem. According to this model, there is only one extra dimension in addition to our (1+3)-dimensional spacetime.

There are two 4-dimensional subspace (or brane) sitting in a 5-dimensional bulk with a 'warped' geometry. One of them is the 'visible' brane which contains all the Standard Model fields and the other is the 'invisible' brane where gravity is strong and only gravitons can propagate in the extra dimension. The extra dimension forms a circle which is folded about a diameter and the two branes are placed at $\phi = 0$ (invisible brane) and $\phi = \pi$ (visible brane). The solution to the 5-dimensional Einstein equation is :

$$ds^2 = e^{-2\kappa R_c \phi} g_{\mu\nu} dx^\mu dx^\nu + R_c^2 d\phi^2. \tag{1.12}$$

Here, ds is a line element in the 5-dimensional bulk, $g_{\mu\nu}$ is the (3+1)-dimensional metric, R_c the radius of curvature and $e^{-2\kappa R_c \phi}$ is the 'warp' factor. The relation between the 4-dimensional Planck scale M_{Pl} and fundamental Planck scale M_5 obtained from this 5-dimensional model is :

$$M_{Pl}^2 = \frac{M_5^3}{k}\left[1 - e^{-2kR_c\pi}\right]. \tag{1.13}$$

In the RS model, the scale 'κ' is of the order of the Planck scale ($\sim 10^{16}$ TeV) and equation 1.13 tells us that the fundamental 5-dimensional Planck scale is of the order of the Planck scale ($M_{Pl} \sim M_5$). The effective interaction Lagrangian on the visible brane is given by :

$$L = -\frac{1}{\overline{M}_{Pl}} T^{\alpha\beta}(x) h^0_{\alpha\beta}(x) - \frac{1}{\Lambda_\pi} T^{\alpha\beta}(x) \sum_{n=1}^{\inf} h^n_{\alpha\beta}(x). \tag{1.14}$$

The Lagrangian consists of two parts. The first part corresponds to the 'zero mode' which describes the gravitational interaction that we experience. The second part is the sum over the Kaluza-Klein(KK) excitation modes and corresponds to the interaction of the KK excited modes of the graviton with Standard Model fields. Here :

$$\Lambda_\pi \sim e^{-\kappa\pi R_c} M_{Pl}. \tag{1.15}$$

From this equation we see that a value of $\kappa R_c \sim$12 makes $e^{-\kappa R_c \pi} \sim 10^{-16}$, which brings down the energy scale in the TeV range. So the 'zero mode' in equation 1.14 is suppressed by a factor of '$1/M_{Pl}$' with $M_{Pl} \sim 10^{16}$ TeV, as a result of which the gravity that we experience is so weak. However, the KK excited states are suppressed only by a factor of '$1/\Lambda_\pi$' with $\Lambda_\pi \sim$ 1TeV. So for the KK excited states, the gravity actually interacts with the matter in the weak ($\sim$ 1Tev) scale. This exponential factor, $e^{-\kappa\pi R_c}$, thus explains the hierarchy between the weak and Planck scales. Experimentally, we try to find the effects of these KK excited states on SM by looking for the production of a KK excited state of the graviton in the weak scale and hence within the energy range of the present experiments.

1.5 Phenomenology of the RS Model

The experimental test for the RS model is performed by searching for the KK excitation of the gravitons. This can be done by looking at the graviton exchange contributions to processes with final states of two fermions or two bosons. Some of the possible final states to look for are $e^+e^-, \mu^+\mu-, \gamma\gamma, W^+W^-, ZZ, b\bar{b}, t\bar{t}$, etc. The signal for excited Graviton is expected to be a resonance in the invariant mass distribution of the final state. Figure 1·1 shows the branching fraction for the different graviton final states as a function of the graviton mass. The branching fraction to $\mu^+\mu-$ and $\tau^+\tau^-$ are also same as e^+e^-(12). The two channels which are explored in this particular analysis are

$$p + \overline{p} \rightarrow G^* \rightarrow e^+e^-$$

$$p + \overline{p} \rightarrow G^* \rightarrow \gamma\gamma$$

These channels provide a clean signal as opposed to other channels which have large background. Due to poor detector resolution, the choice of di-muon final state is not favourable for this search. In this analysis, both the final states $G^* \rightarrow \gamma\gamma$ and $G^* \rightarrow e^+e^-$, are combined to increase the sensitivity as the branching ratio to two photons is twice of that of to two electrons. There are two free parameters in the RS model which govern the phenomenology: the first excited graviton mass 'M_1' and the coupling to the Standard Model 'κ/M_{Pl}'.

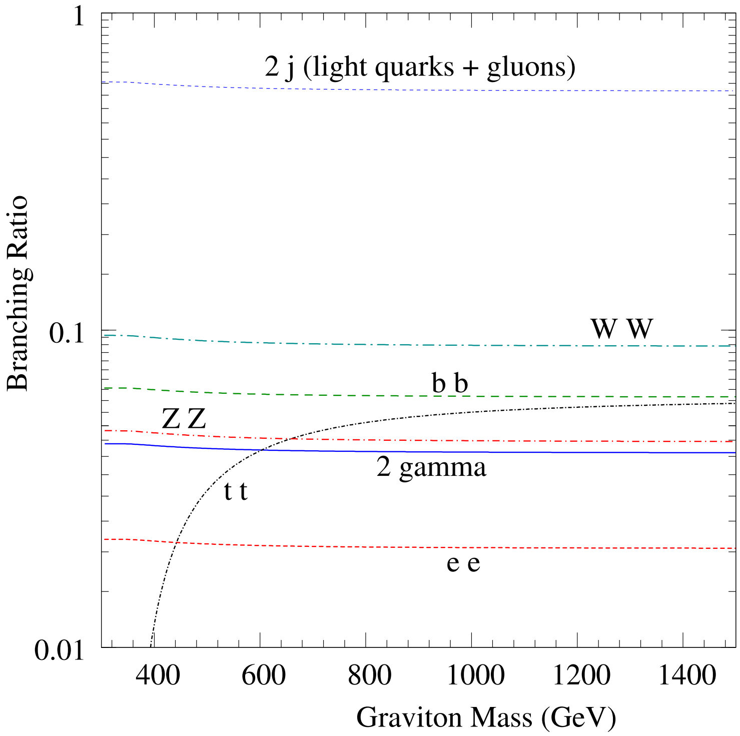

Figure 1·1: Branching ratio of graviton to different final states as a function of graviton mass. This plot was taken from reference (13).

Mass of the graviton

In the RS model, the KK excited states of the graviton have a mass which is given by

$$M_n = x_n \kappa e^{-\kappa r_c \pi} \equiv x_n m_0 \tag{1.16}$$

Here, m_0 is the graviton mass scale and x_n are the zeros of the Bessel function $J_1(x)$ with values, e.g, $x_1 \sim 3.83, x_2 \sim 7.02, x_3 \sim 10.17, x_4 \sim 13.32$(15). This results in a discrete set of possible graviton masses in the invariant mass distribution for different values of 'n' which are not equally spaced. It should be mentioned here that if a graviton is discovered, it will have only one value for m_0. Figure 1·2 shows the graviton resonance production in excess of Drell-Yan (SM process with e^+e^- final state) events for 700 GeV graviton at the

Tevatron. Figure 1·3 shows the same for 1500 GeV graviton along with the subsequent tower members at the LHC.

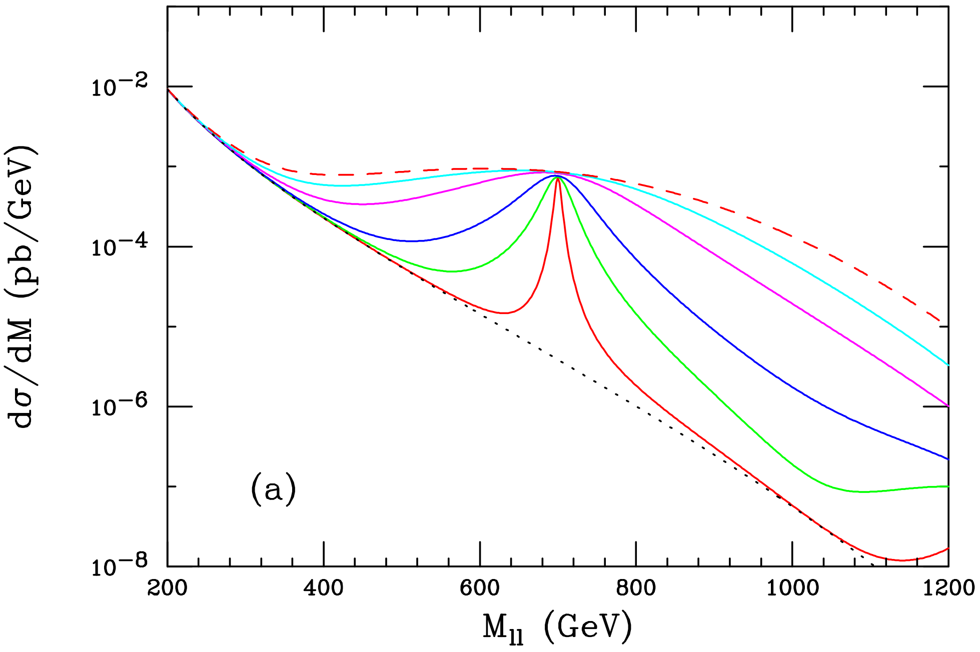

Figure 1·2: The invariant mass distribution for 700 GeV graviton in excess of Drell-Yan events at Tevatron with $\kappa/\overline{M}_{Pl}$=1,0.7,0.5,0.3,0.2 and 0.1 respectively from top to bottom. This plot was taken from reference (14).

Coupling to the Standard Model

The KK excited states of the graviton couple to matter and the coupling is given by $\kappa\sqrt{8\pi}/M_{Pl}$, κ being the curvature of the extra dimension. In this model the curvature κ is assumed to be less than, but of the same order as the Planck scale $\sim 10^{16}$TeV. This requires the coupling $\kappa\sqrt{8\pi}/M_{Pl}$ to be small. The graviton production cross-section is proportional to this coupling as $\sigma \sim \left(\kappa\sqrt{8\pi}/M_{Pl}\right)^2$(15). Figure 1·4 summarizes the different theoretical and experimental constraints. The value of this coupling between 0.01 and 0.1 is probed

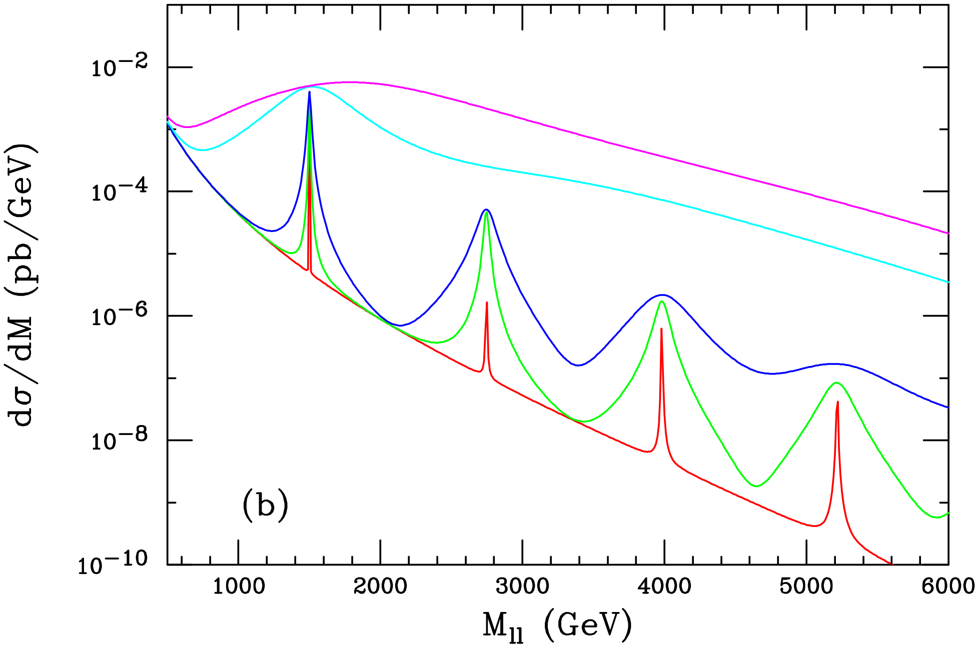

Figure 1·3: The invariant mass distribution for 1500 GeV graviton and the subsequent towers in excess of Drell-Yan events at LHC with $\kappa/\overline{M}_{Pl}$=1,0.5,0.1,0.05 and 0.01 respectively from top to bottom. This plot was taken from reference (14).

experimentally. The lower bound on the coupling (0.01) comes from string theoretic arguments(15). The upper bound (0.1) comes from the constraint on the curvature of the extra dimension, $R_c = 20\kappa^2 < M_5^2$ as shown in Figure 1·4(16).

1.6 Previous searches for RS Gravitons

The Randall-Sundrum model being a very recent model (proposed in 1999), very few dedicated searches for RS Gravitons have been carried out to date. The main effort has been at the Tevatron where both the DØ and CDF experiments are involved in this search. RS Graviton searches have been carried out in di-electron, di-photon and di-muon channels both at the CDF and DØ experiments. The publised result from DØ was based on analyzing

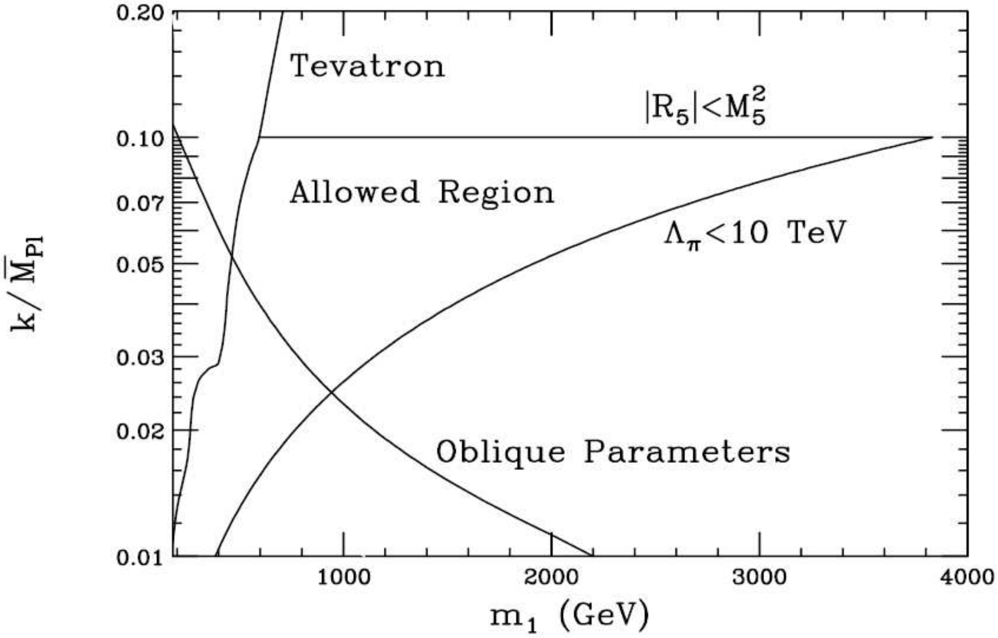

Figure 1·4: Summary of the experimental and theoretical constraints on the RS model. The experimental constriant comes from lepton and jet pair production analysis at the Tevatron. Constraint from the oblique parameter comes from a global fit to the electroweak oblique parameters S and T. The constraint $\Lambda_\pi < 10$ TeV is to make sure that no new hierarchy appears between EW scale and Λ_π. The $R_5 < M_5^2$ is a higher dimensional curvature bound. This plot was taken from reference (16).

~ 300 pb^{-1} of data collected by the DØ detector(18). Figure 1·5 shows the result from the CDF experiment(17) and Figure 1·6 shows the DØ result. The published result from DØ excluded graviton masses $M_1 < 785(250)$GeV for a coupling $\kappa/\overline{M}_{Pl}$ of 0.1(0.01).

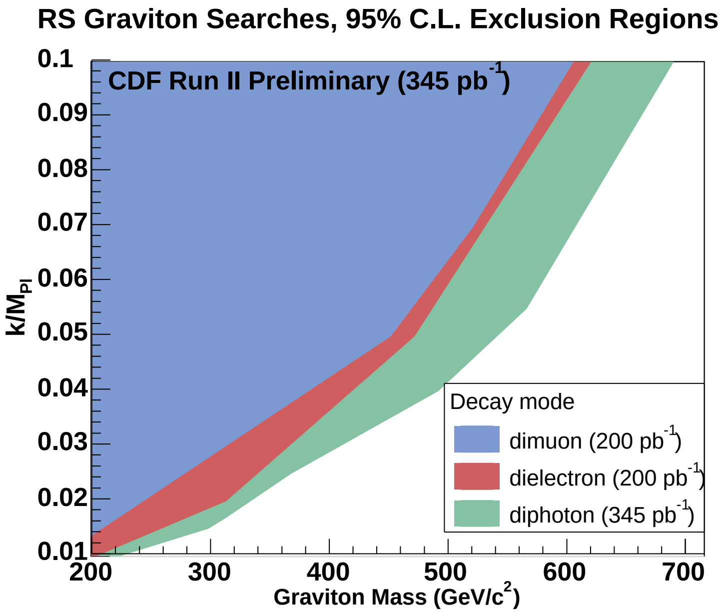

Figure 1·5: 95% confidence level upper limit on $\kappa/\overline{M}_{Pl}$ versus graviton mass M_1 from the previous CDF preliminary result. This plot was taken from reference (17).

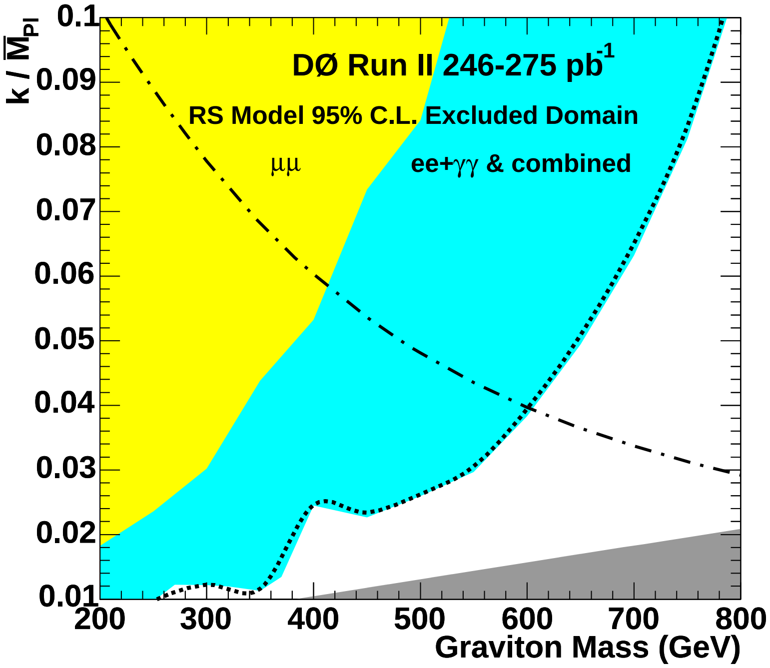

Figure 1·6: 95% confidence level upper limit on $\kappa/\overline{M}_{Pl}$ versus graviton mass M_1 from the previous DØ published result. This plot was taken from reference (18).

Chapter 2

EXPERIMENTAL APPARATUS

The Fermi National Accelerator Laboratory, located near Chicago,IL has the world's highest energy particle accelerator, the Tevatron. Here, protons and anti-protons collide at a center of mass energy, $\sqrt{s}$=1.96 TeV. They collide at the center of two particle detectors situated at two points along the ring: the Collider Detector at Fermilab (CDF) and the DØ detector.

The "first" stage of the DØ experiment, Run I took place between 1992-1996, at a center of mass energy $\sqrt{s}$=1.8 TeV. The next stage of the DØ experiment, Run II, following an upgrade of the Tevatron, started in March 2001 at a center of mass energy, $\sqrt{s}$=1.96 TeV.

The work presented in this thesis was done using data collected by the DØ detector in Run II between 2002 and 2006. In this chapter, we will give a short overview of the Tevatron and the DØ detector.

2.1 Accelerator

The accelerator generates protons and anti-protons and then accelerates them and collides them at a center of mass energy of $\sqrt{s}$=1.96 TeV. This is done in different stages.

First, hydrogen gas is ionized via a magnetron source to H^- ions. These ions are then accelerated to 750 KeV using the Crockroft-Walton accelerator. Next a 150 m long linear accelerator (LINAC) is used to accelerate the H^- ions to 400 MeV. They are then passed through a carbon foil that strips off the electrons, giving bare protons. The stripping occurs (just) after injection into the Booster Synchrotron in which the protons are accelerated to 8 GeV. The Booster injects its 8 GeV proton beam into the Main Injector, which is a synchrotron $\sim$ 1.9 mile in circumference. The main injector then makes a single highdensity bunch of $\approx 5 \times 10^{12}$ protons. These bunches of protons are then accelerated to 120 GeV to be used for anti-proton production and to 150 GeV to be injected into the Tevatron.

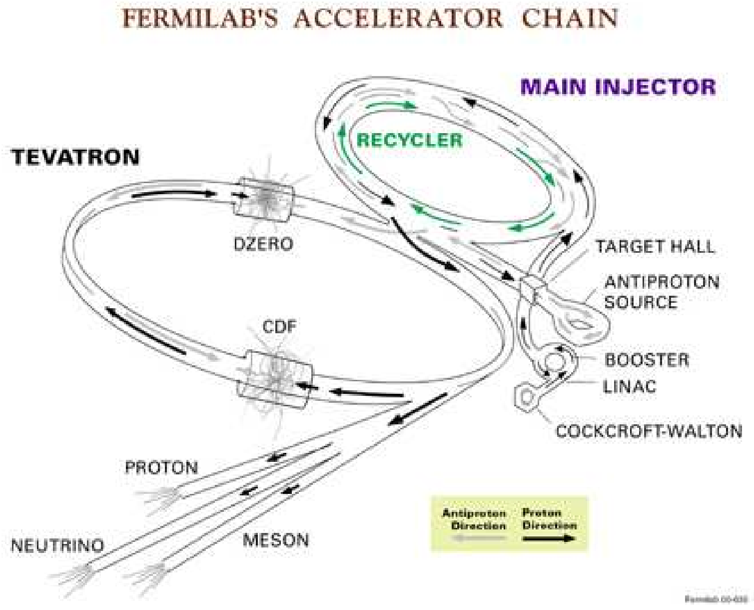

Figure 2·1: Schematic of the Fermilab accelerator chain(20).

In the antiproton source, the 120 GeV proton bunches from the main injector are focused on a nickel target. Antiprotons are produced at a rate of approximately 15 anti-protons for every million protons on the target. The anti-protons are then stored in the Accumulator until a sufficient number ($1.5 - 2 \times 10^{12}$) of anti-protons accumulates.

The Tevatron is the final level of acceleration. It is a synchrotron ring with ~ 4 mile circumference. The Main Injector delivers 36 bunches of protons (about 2.7×10^{11} protons per bunch) to the Tevatron. Next, anti-protons are transferred from the Accumulator to the Main Injector, accelerated to 150 GeV and injected into the Tevatron. In the Tevatron, 36 bunches of protons and 36 bunches of anti-protons are then accelerated in two counterrotating beams up to a final energy of 980 GeV. Finally the protons and anti-protons collide at two interaction region at an interval of 396 ns, DØ being one of the interaction regions.

2.2 DØ Detector

The DØ detector consists of three primary detector systems as we move from inside to outside and they are all symmetric about the Tevatron beam line. Figure 2·2 shows the schematic side view of the Run II DØ detector. The three main detector systems are tracking system, calorimeter and muon spectrometer.

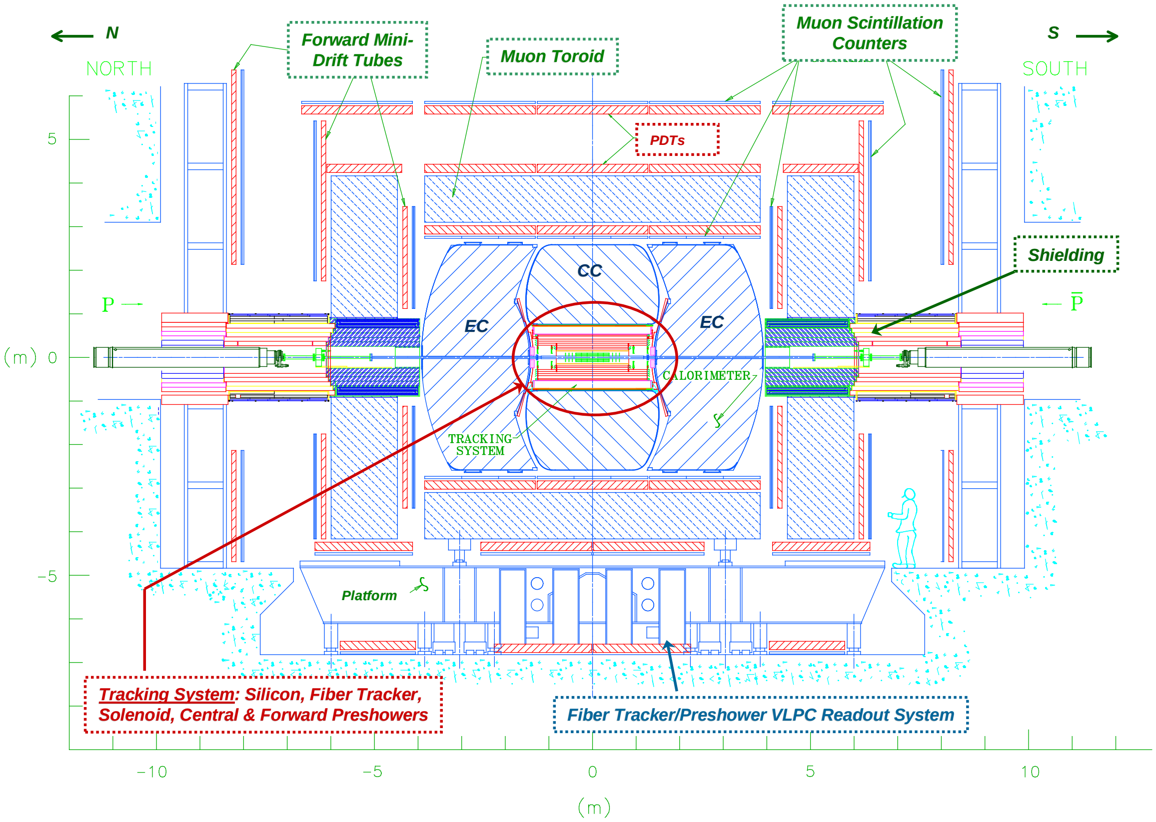

Figure 2·2: Side view of the DØ detector (25).

2.3 Coordinate system and some variables

Before we talk about the different detector systems, it is good to explain some of the commonly used variables. The DØ detector uses standard right-handed coordinate system.

The collision point is the center of the detector with coordinate (0,0,0). The direction of the proton is the positive $+z-$axis. The $+x-$axis is horizontal pointing towards the center of the ring. The $+y-$axis points vertically upwards. Then there are two angles. The polar angle, θ, is defined such that $\theta = 0$ lies along the beam pipe in the $+z$ direction. The azimuthal angle, ϕ, is defined such that $\phi = 0$ points along $-x-$axis, away from the center of the ring. In high energy physics we deal with relativistic particles and so it is convenient to use a variable 'pseudo-rapidity' which is a measure of the polar angle θ. The pseudo-rapidity 'η', is defined as

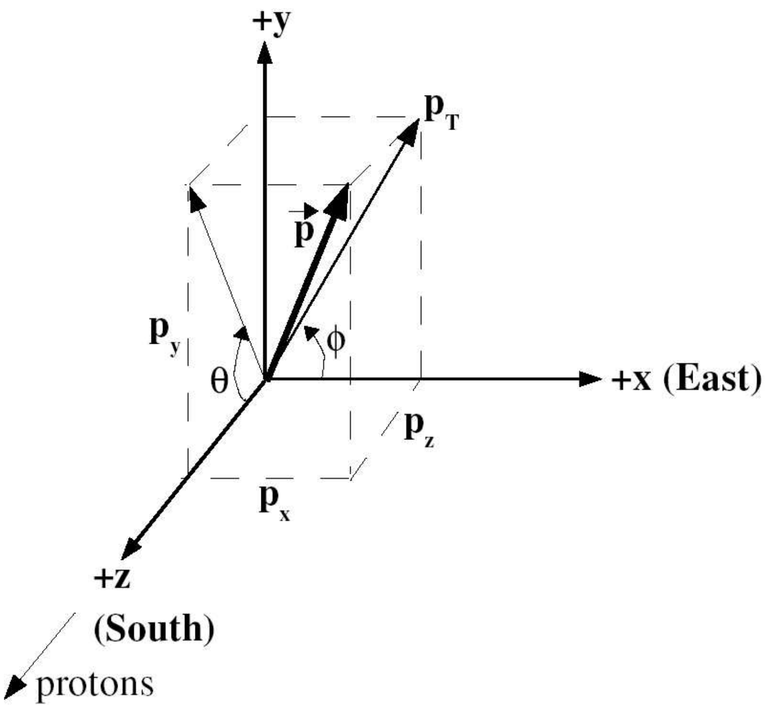

Figure 2·3: Diagram of p_T in the DØ coordinate system(19).

$$\eta = -\ln \tan\left(\frac{\theta}{2}\right). \tag{2.1}$$

The pseudo-rapidity is a high energy approximation of rapidity y, defined as

$$y = \frac{1}{2} \ln \left(\frac{E + p_z}{E - p_z} \right). \tag{2.2}$$

Here the energy of the particle is E and the longitudinal momentum is p_z. The advantages of using η are:

- The interval in η is Lorentz invariant.
- As a consequence of this Lorentz invariance, the particle multiplicity is almost constant in rapidity.

Another variable used is the 'transverse momentum' which is the component of the particle momentum vector normal to the z axis.

$$p_T = p \sin \theta. \tag{2.3}$$

The transverse momentum is used because the partons initially do not have any transverse (x-y plane) component of momentum and hence it is easy to apply the conservation of transverse momentum. On the contrary, since the partons initially do have z-component of momentum (along the beam pipe), applying the conservation of the total momentum becomes complicated.

2.4 Tracking System

The tracking system of the DØ detector is the innermost part surrounding the beam pipe. The tracking system consists of four parts:

- Silicon Microstrip Tracker (SMT);
- Central Fiber Tracker (CFT);
- Solenoid magnet;
- Preshower.

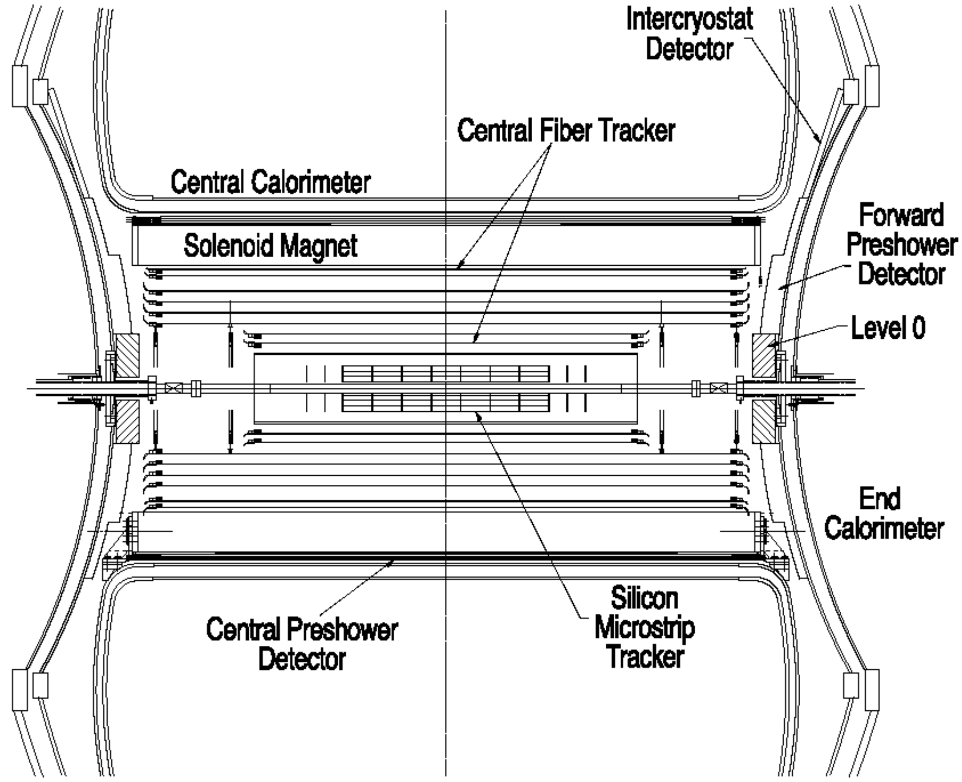

Figure 2·4: The DØ tracking system (25).

Figure 2·4 shows the different parts of the DØ tracking system. The main function of the tracking system is reconstruction of trajectories of the charged particles. As a charged particle moves through the different layers of the tracking system, signals are generated at different layers. The trajectory of the charged particle is reconstructed by joining these signals at different layers. In addition, the tracking system being inside a strong magnetic field, the momentum of the charged particle is measured from the curvature of its trajectory.

2.4.1 Silicon Microstrip Tracker (SMT)

The Silicon Microstrip Tracker (SMT) was installed in the DØ detector during the Run II upgrade. It consists of 6 barrels, 12 F-disks and 4 H-disks as shown in figure 2·5. The barrels are made of four layers and each layer is made of multiple ladders. The ladders are segmented into parallel strips, which can be parallel to the beam pipe (axial) or at an angle with respect to the beam (2° or 90°). The functionality of this detector utilizes the properties of the semiconductor. The bulk silicon is doped to be an n-type semiconductor and the strips are doped to be a p-type semiconductor. Between them a p-n junction forms. This junction is reverse biased. As charged particles pass through silicon, they generate electron-hole pairs, resulting in a small current across the junction which is detected as the source of the signal. The SMT detector provides a spatial resolution of approximately 10 μm in $r-\phi$ and 100 μm in $r-z$ and covers $|\eta| < 3$.

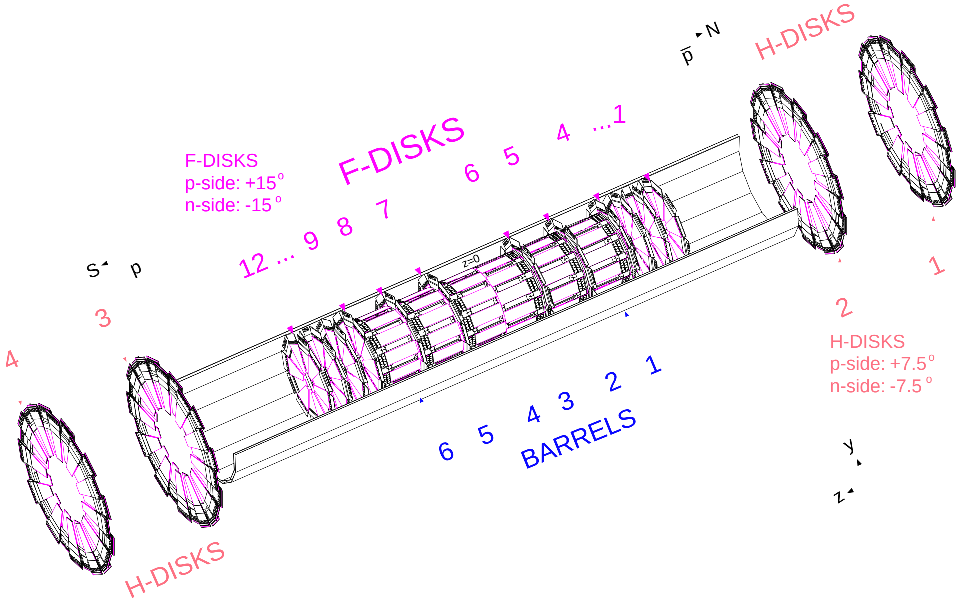

Figure 2·5: DØ Run II Silicon Microstrip Tracker detector(20).

2.4.2 Central Fiber Tracker (CFT)

The Central Fiber Tracker (CFT) surrounds the SMT. It consists of eight concentric carbon fiber barrels holding layers of scintillating fibers. Figure 2·6 shows a cross-section view of the CFT. It is divided into 80 sectors in phi for readout. As the charged particles pass through these fibers, photons are produced. These are then converted into electrical pulses using Visible Light Photon Counters (VLPC). The CFT covers $|\eta| < 2$. The position resolution of the CFT is $\sim 100\mu$m.

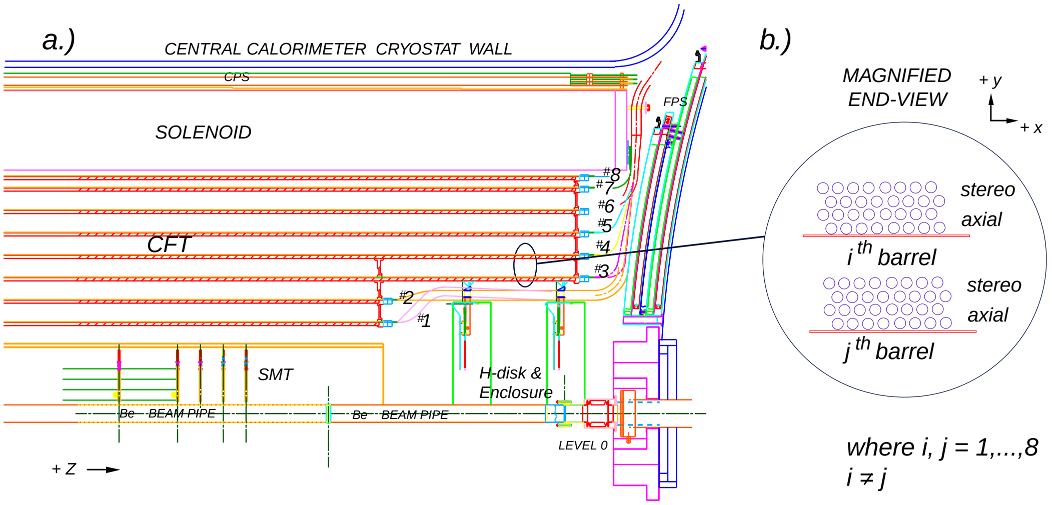

Figure 2·6: (a) A quarter r-z view of the CFT detector showing the nested eight barrel design. (b) A magnified r-ϕ end view of the two doublet layer configuration for two different barrels(21).

2.4.3 Solenoid

The solenoid surrounds the CFT. It provides a 2 Tesla uniform axial magnetic field. This magnetic field bends the trajectory of the outgoing charged particles. The radius of curvature is used to calculate the momentum of the charged particles. The equation is given by:

$$p = q \times B \times R, \tag{2.4}$$

where 'p' is the momentum of the charged particle, 'q' is the charge of the particle, 'B' is the solenoid magnetic field and 'R' is the radius of curvature of the particle trajectory.

2.4.4 Preshower Detector

The preshower detectors are located between the solenoid and the calorimeters. The three preshower detectors are the Central Preshower (CPS) for $|\eta| < 1.2$ and the two forward preshower (FPS) for $1.4 < |\eta| < 2.5$. The solenoid around the tracking system provides unintrumented material ($\sim$ 0.8 to 2 radiation length) for the outgoing particles to interact with and lose energy. This makes the energy resolution of the calorimeter worse. The function of the preshower is energy sampling of particles coming out of the solenoid (before entering the calorimeter) to improve overall energy resolution. The central preshower detector is made of one layer of lead and three layers of scintillating strips. The lead with varying thickness makes the total radiation length around 2 for the particles coming out in all angles. The function of the forward preshower is to improve electron identification in the forward region. It is made of two layers of scintillators followed by a layer of lead ($\sim$2 radiation length) and then followed by another two layers of scintillators.

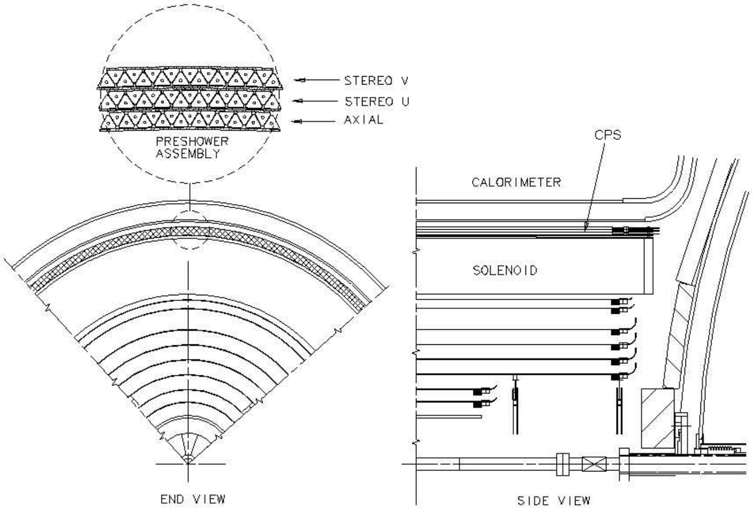

Figure 2·7: Cross-sectional end view (left) and side-view (right) of the Central Preshower detector (25).

2.5 Calorimeter

The calorimeter consists of three parts, the central calorimeter (CC) with a coverage of $|\eta| < 1.1$ and two end calorimeters (EC) with a coverage of $1.5 < |\eta| < 4.5$ (Figure 2·8). The function of the calorimeter is to measure the energy of the particles. As the particles pass through the different layers of the calorimeter, they interact with the material and generate electromagnetic or hadronic showers.

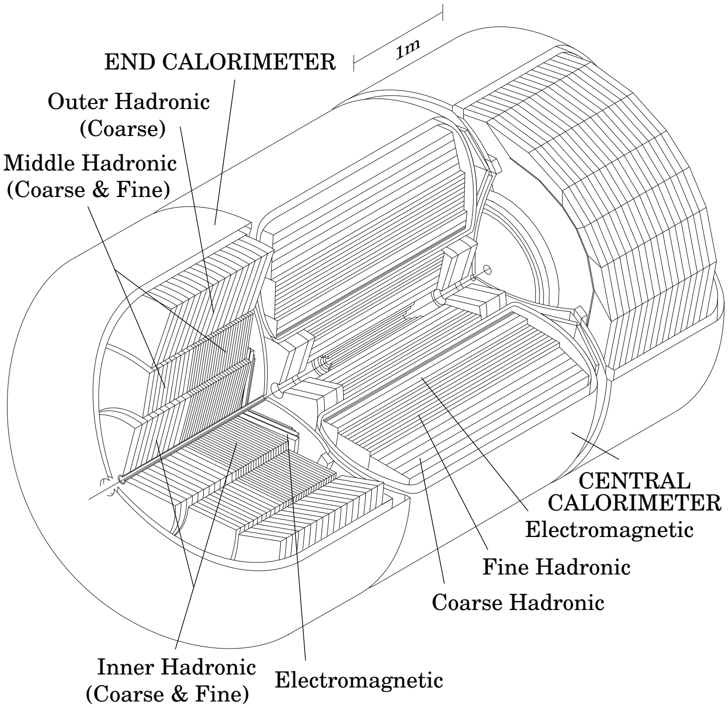

Figure 2·8: Overall view of the DØ calorimeter system(25).

The calorimeter is made of a large number of modules. Each module is made of a series of unit cells. Figure 2·9 shows the schematic view of a calorimeter unit cell. The unit cell consists of an absorber plate and a signal board. Liquid argon, the active material of the calorimeter, fills the gap.

The calorimeter modules are segmented into three distinct sections as shown in figure 2·8:

- electromagnetic (EM)
- fine-hadronic (FH)
- coarse-hadronic (CH)

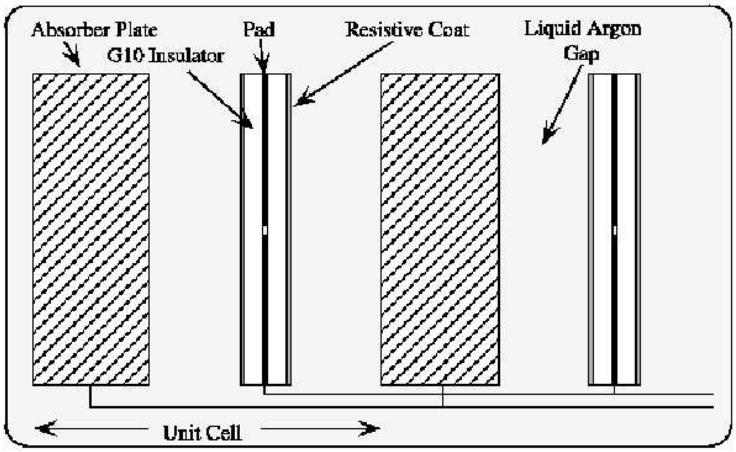

Figure 2·9: Unit Cell in the Calorimeter(22).

The central calorimeter consists of 4 EM layers, 3 FH layers and 1 CH layer. The end calorimeter consists of 4 EM layers, 4 FH layers and 3 CH layers. In the central calorimeter, the transverse segmentation of the cells is $\Delta\eta \times \Delta\Phi = 0.1 \times 0.1$ in all the EM layers except in the third EM layer where it is $\Delta\eta \times \Delta\Phi = 0.05 \times 0.05$. In the EC, the segmentation is also $\Delta\eta \times \Delta\Phi = 0.1 \times 0.1$. For $|\eta| > 3.2$, it is 0.2×0.2. Typical transverse size of the EM shower is $1-2$ cm which is comparable to the cell size in $\eta - \phi$. The maximum of the shower is expected to occur in the third layer of the EM calorimeter. Hence, the segmentation is finer in the third EM layer for more precise location of the EM shower centroid. The different parameters of the calorimeter are summarized in Table 2.1.

Module	EM	FH	CH
Rapidity	±1.2	±1.0	±0.6
Number of modules	32	16	16
Type of absorber	Ur	U-Nb	Cu
Thickness of absorber in mm	3	6	46.5
Gap of Argon in mm	2.3	2.3	2.3
Radiation length	20.5	96	3.2
Nuclear absorption length	0.76	3.2	3.2

Table 2.1: Different parameters of the DØ central calorimeter(CC).

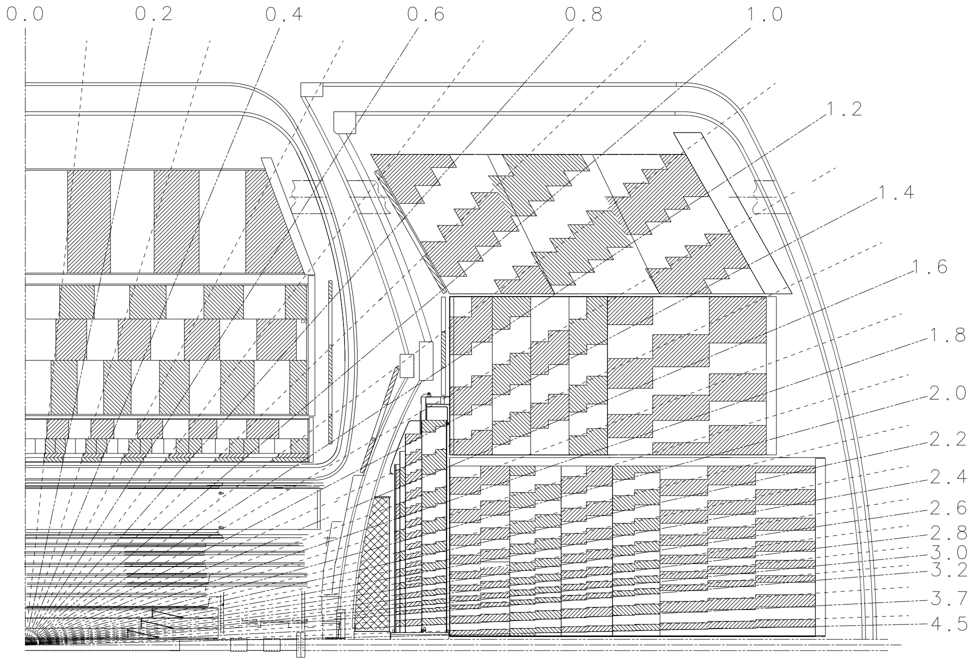

Figure 2·10: A quarter of the calorimeter in the $r-z$ plane of the detector showing the tower geometry(22).

When high energy electrons or photons pass through the calorimeter, they interact with the material. For example, an electron passing through the calorimeter radiates a photon, the photon, in turn, makes an electron-positron pair. With this process being repeated, an electromagnetic shower is generated. When a photon enters the calorimeter, the showering process starts primarily through pair production ($\gamma \rightarrow \mathrm{e}^{+}\mathrm{e}^{-}$). The electrons primarily lose energy by ionization and bremsstrahlung. There is a critical energy E_c for the electrons approximated by the equation:

$$E_c = \frac{800MeV}{Z+1.2}. \tag{2.5}$$

where Z is the atomic number of the interacting material. Electrons with energy greater than E_c mainly lose energy through bremsstrahlung. The energy of the electron or photon is expected to drop exponentially as

$$E(x) = E_0 e^{-x/X_0}. \tag{2.6}$$

Here E_0 is the original energy of the particle, 'x' is the distance traveled by the particle and X_0 is called the radiation length of the material through which the particle passed. A particle travelling one radiation length thus loses $\sim$ 63% of its original energy on average.

The hadronic shower is initiated when hadronic particles passing through the calorimeter interact inelastically with the nuclei of the absorbing layers. Pions and nucleons are produced from these interactions which in turn interact with other nuclei resulting in a shower. The hadronic calorimeter depth is expressed in terms of nuclear interaction length λ_I, which is given by:

$$\lambda_I = 35gcm^2 A^{1/3}, \tag{2.7}$$

where "A" is the atomic weight of the material. When the electromagnetic or hadronic showers are generated, the particles lose energy by interacting with the heavy absorber layers of the unit cell and then ionize the liquid argon medium while passing through them. The number of charged particles traversing the argon gap is counted by measuring the ionization. This number is proportional to the energy lost by the incident particle. Since only a part of the particle energy is 'sampled' for energy measurement, this is called "sampling calorimeter". The electromagnetic section of the calorimeter being $\sim$20 radiation length, most of the energy from electromagnetic objects is deposited in the EM calorimeter.

The resolution of the calorimeter is described by:

$$\frac{\sigma_E}{E} = \sqrt{C^2 + \left(\frac{S}{\sqrt{E}}\right)^2 + \left(\frac{N}{E}\right)^2}. \tag{2.8}$$

Here C correspond to calibration error and energy leakage, S represents the sampling fluctuations and N is the noise term. The values for the central electrons are : C = 0.0408, S = 0.15 $\sqrt{\mathrm{GeV}}$ and N = 0.29 GeV(26).

2.6 Muon Detector

The muon system is the outermost part of the DØ detector. Due to their large mass, muons lose very little energy through bremsstrahlung as they pass through the tracking system and the calorimeter. Muons primarily lose energy through ionization and excitation of the detector media. The muons generated at DØ are primarily minimum ionization particle (MIP) with an energy of few GeV. Hence, they pass through the tracking system and the calorimeter, loosing very little energy. The muon system is made of the following components:

- Wide Angle MUon Spectrometer (WAMUS) covering $|\eta| < 1$
- Forward Angle MUon Spectrometer (FAMUS) covering $1 < |\eta| < 2$

The WAMUS and FAMUS, both are made of two types of detectors, drift tubes and scintillators. The WAMUS and the two FAMUS consists of three layers (A,B and C) and between layer A and layer B, there is a 1.8 T toroidal field.

2.7 Trigger

With protons and anti-protons colliding at an interval of 396 ns, the collision rate is about 2.5 MHz. Out of these 2.5×10^6 events generated per second at DØ a very small fraction is of interest. Also, technically it is difficult to read and process events at this high rate. So through a fast selection, only those events which have properties matching the characteristics of physics events of interest are saved. This is done in three stages through a combination of hardware and software, called "Trigger". Figure 2·11 is an over view of the DØ trigger system. The trigger system at DØ consist of:

- Level 1 (L1)- Hardware based selection.
- Level 2 (L2)- Selection based on combination of hardware and software
- Level 3 (L3)- Software based selection

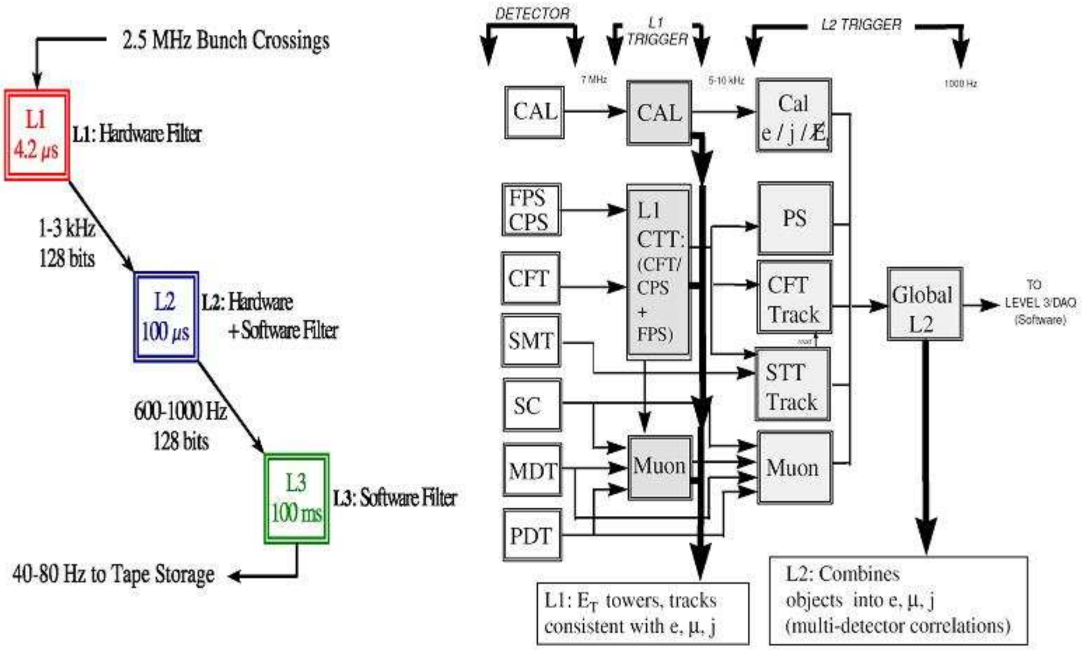

Figure 2·11: Overview of the DØ trigger system(20).

L1 Trigger

The first level of the trigger system (L1) takes a very fast decision for each bunch crossing (event), based on the raw detector information and simple algorithms. Information from the CFT, preshower, calorimeter and muon system is processed in parallel. The L1 framework (L1FW) gets the information from all the detector parts and takes the decision. If accepted by L1, the event is sent to L2.

The calorimeter trigger is based on energy deposited in trigger towers. A trigger tower is formed by summing up the energy deposited in the different layers of the calorimeter. Calorimeter trigger towers cover $\Delta\eta \times \Delta\Phi = 0.2 \times 0.2$. For this analysis, only events with electromagnetic(EM) objects were used. The current accept rate for L1 is between 1 to 3 KHz.

L2 Trigger

In the second level of the trigger (L2), different physics objects (e.g. electrons, muons, jets, etc.) are reconstructed by using the information from the L1 trigger and the different subdetector systems. This is mainly done in software using different processor boards which collects information from the different L1 triggers. From hardware perspective, a processor board is part of a level 2 trigger system unit running Linux and based on Compaq PC164 design (23).

The calorimeter preprocessor (L2CAL) gets the information from L1 trigger towers and reconstructs L2 EM cluster. Then events are selected that have an EM cluster above a certain energy threshold. The accept rate of L2 is $\sim$ 1kHz.

L3 Trigger

The final level of the trigger system is the L3/Data Acquisition System (DAQ). This is a software based selection system running in a farm of parallel PCs (also called nodes). After an event is accepted by L2, all the information from the different readout crates for that particular event is routed to one of the nodes. Here a more sophisticated reconstruction of the physics objects is carried out and a more detailed algorithm can be applied to select events.

For electromagnetic objects, a fast version of the offline electron identification algorithm is used and cuts are applied on various parameters such as energy, shower shape, fraction of energy deposited in the electromagnetic calorimeter, etc.

The L3 accept rate is approximately 50 Hz. Finally, the events accepted by L3, are stored on a tape for offline event reconstruction.

Chapter 3

OBJECT RECONSTRUCTION AND IDENTIFICATION

The data that are collected by the DØ detector are a collection of digitized signals. For physics analysis, the physics objects in each event need to be identified. The reconstruction and identification of physics objects are accomplished by the DØ offline reconstruction software package, DØRECO. Since this analysis is based on the reconstruction of electrons and photons, in this chapter the reconstruction and identification of the electromagnetic objects are discussed.

3.1 Object reconstruction in calorimeter

The calorimeter readout is in terms of ADC (Analog to Digital Converter) count. The real ADC count is read if it is greater than 2.5σ above the pedestal value (i.e. calorimeter readout without any beam), where σ is the width of the pedestal distribution. This is called zero-suppression. The conversion of the ADC count to energy is done by calibration. A pulse of known energy is sent through the calorimeter electronics and the corresponding ADC count is read out which gives the ADC count to energy conversion factor. Next the energy of all the cells having the same η and ϕ are added which makes the calorimeter tower. The total energy E and the position in $\eta - \phi$ is obtained from the calorimeter. With the approximation that the particles are massless, the four momentum (E, p_x, p_y, p_s) are obtained.

$$p_x = E \sin\theta \cos\phi, \tag{3.1}$$

$$p_y = E \sin\theta \sin\phi, \tag{3.2}$$

$$p_z = E\cos\theta. \tag{3.3}$$

3.2 Electromagnetic object reconstruction

The showers originating from the electromagnetic objects (electrons and photons) are concentrated clusters of energy deposited mainly in the electromagnetic calorimeter. There are standard algorithms used for reconstruction of the electromagnetic objects at DØ . One of them is the “Simple Cone Algorithm”. The electromagnetic tower is constructed by adding the energies in the four EM calorimeter layers and the first hadronic layer. Starting with the highest transverse energy EM tower, the towers around that are added, within a cone of radius $R = \sqrt{\Delta\eta^2 + \Delta\phi^2} < 0.2$ and with transverse energy $E_T > 50$ MeV. This forms an EM cluster in the central calorimeter (CC) region. In endcap (EC) calorimeter, the cells forming a cluster should have a transverse distance less than 10cm from the highest transverse energy EM tower.

3.3 Electromagnetic object identification

Various parameters are used to characterize an electromagnetic shower. The parameters used for event selection in this analysis are discussed in detail.

Electromagnetic Fraction

The electromagnetic shower is expected to deposit most of the energy in the EM calorimeter. This is expressed by:

$$f_{em} = \frac{E_{em}}{E_{total}}. \tag{3.4}$$

Here, E_{em} is the energy deposited in the EM layers of the calorimeter and E_{total} is the total energy deposited in the four EM and first hadronic layer of the calorimeter.

Isolation Fraction

The electromagnetic objects from gravitons tend to be isolated in the calorimeter $\eta - \phi$ space. Isolation fraction gives a quantitative measure of the degree of isolation of a given electromagnetic object. The isolation fraction is defined by:

$$f_{iso} = \frac{E_{tot}(R < 0.4) - E_{em}(R < 0.2)}{E_{em}(R < 0.2)}. \tag{3.5}$$

$E_{tot}(R < 0.4)$ is the total energy deposited in the tower within a cone of radius $R = 0.4$ around the direction of the cluster. $E_{em}(R < 0.2)$ is the energy deposited in the EM calorimeter within a cone of radius R=0.2 around the direction of the cluster.

H-Matrix

The shower shape of an electron or a photon has a distinctive profile different from that originating from a hadronic particle. The shower shape originating from an EM object is characterized by using several parameters.

- The fraction of shower energy in each of the four EM calorimeter layers EM1, EM2, EM3 and EM4. This characterizes the longitudinal development of the EM shower → 4 parameters.
- Total energy deposited in the EM calorimeter → 1 parameter .
- Consistency of the shower with the vertex z position → 1 parameter.
- The lateral development of the shower. This is characterized by the width in ϕ in the third layer of the EM calorimeter (EM3) with the best granularity → 1 parameter.

The H-matrix χ^2 with these seven parameters (7×7 H-matrix χ^2) gives a measure of how much the shower shape from an EM candidate matches with the MC detector simulation of EM shower shape. It is defined by:

$$\chi^2 = \sum_{i,j=1}^{7} (x_i^{'} - \overline{x}_i) H_{ij} (x_j^{'} - \overline{x}_j) \tag{3.6}$$

Here the sum is over the seven parameters and $\overline{x}$ is the average for each parameter obtained from the MC. H is the inverse of the covariance matrix and H_{ij} are the elements of the matrix. A smaller value of the χ^2 indicates better agreement of the shower with an EM shower.

Track Match

In this analysis, no track match was required for event selection. However, for some studies (e.g. systematics), a track match was required. The trackmatch is required to identify electrons. With information from the EM calorimeter, we can reconstruct an EM object with several variables as described above. Electrons are charged particles and interact with the central tracking system so that their trajectory can be reconstructed as a track. It is expected that the track should point to an EM object reconstructed in the calorimeter. The quality of the match is expressed in terms of a χ^2 defined as:

$$\chi^2 = \left(\frac{\delta\phi}{\sigma_{phi}}\right)^2 + \left(\frac{\delta z}{\sigma_z}\right)^2 + \left(\frac{\frac{E_T}{P_T} - 1}{\sigma_{\frac{E_T}{P_T}}}\right)^2 \tag{3.7}$$

Alternately the quality of track match is also expressed in terms of a spatial χ^2 defined as:

$$\chi^2_{spatial} = \left(\frac{\delta\phi}{\sigma_{phi}}\right)^2 + \left(\frac{\delta z}{\sigma_z}\right)^2 \tag{3.8}$$

Track Isolation

In the calorimeter, the electromagnetic objects from gravitons are expected to be isolated. No track is expected around an EM object. The track isolation cut is based on this idea. The steps to calculate the track isolation are as follows:

- Select tracks which originate close (<2cm) to the primary vertex.
- Calculate the ΔR between these tracks and the EM object in $\eta - \phi$ space.

$$\Delta R = \sqrt{(\Delta\phi)^2 + (\Delta\eta)^2}$$

- Calculate the sum of the p_T of all the tracks within a cone with $0.05 < \Delta R < 0.4$ around the EM object.

For isolated particles, this sum should be small. For the EM object selection, a cut is applied on this sum.

ID 10 or 11

The electromagnetic objects with ID 10 or 11 are with loose selection criteria. ID 10 corresponds to a calorimeter EM cluster with a transverse energy $E_T > 1.5$ GeV and electromagnetic fraction $f_{em} > 0.9$. Electromagnetic objects with ID 11 is a loose electron candidate with a track match. The requirement for loose electron is a calorimeter tower matched with a track with a minimum transverse energy $E_T > 0.5$ GeV and electromagnetic fraction $f_{em} > 0.7$.

Chapter 4

DATA AND SIMULATION

In this chapter the data and the simulated events used for this analysis are discussed.

4.1 Data

The data used for this analysis were taken between October 2002 and February 2006. All the data have been reconstructed with version p17 of the DØ reconstruction program. The starting point for this analysis was the dataset with two high-p_T electromagnetic (EM) clusters, the so-called "2EMhighpt skim" that consists of approximately 34M events. The 2EMhighpt skim requires both the EM objects to pass the following selection cuts:

- ID = 10 or 11
- $p_T > 15$ GeV

It was further reduced with the following selections:

- bad runs and bad luminosity blocks were removed to account for the data quality
- the events were required to pass the logical OR of a set of ~80 triggers requiring one or two electromagnetic clusters
- duplicate events were removed
- events were selected with two electromagnetic objects where both satisfy the following loose cuts:
  - ID = 10 or 11

- contained in the fiducial region of the central calorimeter. The fiducial region of the calorimeter excludes all gaps, both in η (1.1< detector $|\eta|$ <1.5) and in ϕ (total 32 gaps in ϕ, each with width = 0.02 radian).
- $p_T > 25$ GeV
- fraction of energy in electromagnetic calorimeter $f_{em} > 0.9$
- fraction of energy in isolation cone $\frac{E_{Tot}(0.4)-E_{EM}(0.2)}{E_{EM}(0.2)} = f_{iso} < 0.2$

About 1.4M events were left after these cuts.

4.2 Trigger

From the list of ~80 triggers, eight triggers were shortlisted. A logical OR of these eight triggers passed 97% of the 1.4M data. These eight triggers, their corresponding trigger versions and the integrated luminosity corresponding to each of these triggers, are listed in Table 8.1. The final analysis was done using data triggered by a logical OR of these eight triggers.

Trigger	Trigger name	Trigger version	Integrated luminosity pb^{-1}
Single-EM	EM_MX_SH	V8 to V11	122
	E1_SH30	V12 and V13	596
	E1_SHT22	V13	377
	E1_SH35	V14	350
Di-EM	2EM_HI	V8 to V11	122
	E1_2L15_SH15	V12 and V13	596
	E1_2L20	V12 and V13	596
	E1_2L20_L25	V14	350

Table 4.1: List of triggers.

4.3 Simulation

For this analysis, simulated events (Monte Carlo) were used for both background prediction and to get the signal efficiency. The advantage of using simulated events is getting a clean sample for some physics process that is of interest. Although the simulation does not represent the data exactly, it is very close to real data. The event simulation was done in several steps. The first step is event generation. There are several standard programs (event generators) used for generating simulated events at the hard scattering level. For this analysis, all the simulations were done using PYTHIA(27). At the Tevatron, proton and anti-proton collide which actually results in a quark anti-quark interaction. The quark (anti-quark) taking part in the collision carry only a fraction of the total proton (anti-proton) energy. The parton distribution functions (PDF) gives the probability a quark (anti-quark) will carry a certain fraction of the total proton (anti-proton) energy. There are different PDF's available. All the simulated samples used for this analysis were generated using the PDF CTEQ6L1(39). The quark or gluon produced from the hard scattering develops into a hadronic shower forming a jet, which is also called hadronization. A different program is used to simulate the hadronization.

The next step is to model the DØ detector. The detector model is implemented using the GEANT3 package(28). This package models the effect of the magnetic field and detector material. This also models the interactions of the particles with the detector material like ionization, secondary particle production etc.

The third stage of the simulation was done by using the DØ sim package. The function of this package is to model the response of the detector. At this stage the noise due to different detector subsystems is simulated and digitized. This completes the simulation. The output of this simulation is the equivalent of raw data from the detector. Finally the DØ reconstruction program was run to reconstruct the physics objects. The object reconstruction is described in detail in chapter 3.

Signal sample

The signal sample for this analysis is a 2→2 process with final states, e^+e^- and $\gamma\gamma$. The initial particles are a quark-antiquark pair or a pair of gluons and the mediator is the graviton. The two free parameters for the RS model are the mass of the first excited graviton state M_1 and the coupling to the standard model $\kappa/\overline{M}_{Pl}$. Signal samples for different graviton masses but with the same coupling $\kappa/\overline{M}_{Pl}$=0.1 were generated. Table 4.2 shows all the signal samples generated along with their corresponding leading order (LO) cross-section.

RS Graviton Mass (GeV)	LO Cross-Section × Branching Ratio $p\overline{p} \to G + X$, $G \to e^+e^-$ or $\gamma\gamma$(pb)	Number of Events
200	28.7	10000
220	17.6	10000
240	11.6	10000
250	9.9	10000
270	6.7	10000
300	4.2	10000
320	3.1	10000
350	2.0	10000
370	1.5	10000
400	1.1	10000
450	0.58	10000
500	0.33	10000
550	0.19	10000
600	0.12	10000
650	0.07	10000
700	0.041	10000
750	0.025	10000
800	0.015	10000
850	0.0087	10000
900	0.0051	10000
950	0.0029	10000
1000	0.0016	10000

Table 4.2: List of RS graviton MC samples used for this analysis.

Background samples

The two major irreducible background for this analysis are Drell-Yan (DY) with final states e^+e^- and direct diphoton production. Simulated events for these two SM physics processes were used. The samples were generated with different mass windows. The details of the different sets of simulated samples are listed in Table 4.3.

Process	Mass Window (GeV)	LO Cross-Section (pb)	Number of Events
DY	60-130	178	264750
	130-250	1.3	27500
	250-500	0.11	27000
	>500	0.0045	25500
$\gamma\gamma$	50-130	42.7	50500
	130-250	3.1	51500
	250-500	0.49	26750
	>500	0.034	25500

Table 4.3: List of DY and $\gamma\gamma$ MC samples used in this analysis.

Chapter 5

EVENT SELECTION

5.1 Selection Cuts

For this analysis events were selected that have two high p_T objects consistent with electromagnetic showers. In order to accept both $\gamma\gamma$ and ee decay channels no track match was required for the objects. The following set of cuts defines an electromagnetic shower for the final event selection:

- ID = 10 or 11
- contained in the eta fiducial region of the central calorimeter. The eta fiducial region of the calorimeter excludes the gap in η (1.1< detector $|\eta|$ <1.5).
- detector $|\eta|$ <1.1
- $p_T > 25$ GeV
- fraction of energy in electromagnetic calorimeter $f_{em} > 0.97$
- fraction of energy in isolation cone $f_{iso} < 0.07$
- consistency with electromagnetic shower shape : 7×7 H-matrix $\chi^2 < 12$
- sum of transverse momentum (p_T) of tracks in isolation cone [$0.05 < \triangle$ R < 0.4 with $\triangle R = \sqrt{(\triangle\eta)^2 + (\triangle\phi)^2}$ around the object direction] $p_{iso} < 2$ GeV

With these selection criteria, events were selected from both DATA and MC.

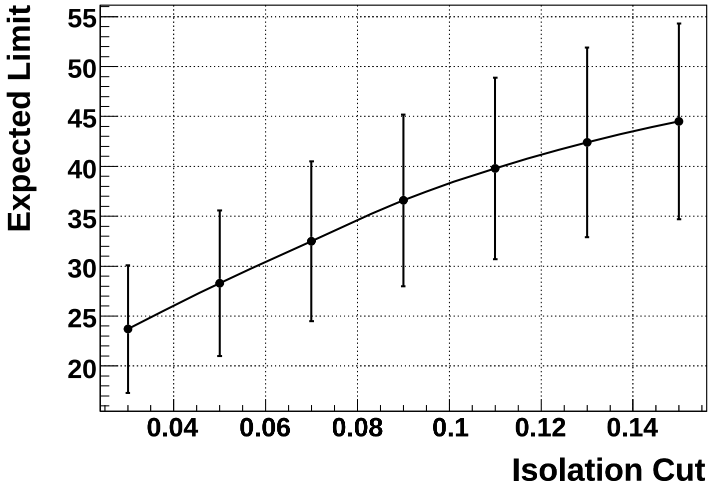

Figure 5·1: Expected limit at 95% confidence level as a function of Isolation cut for graviton mass of 200 GeV. The error bars on the expected limit show the standard deviation.

5.2 Cut Optimization Study

The selection cuts applied here are the optimized cuts suggested by the algorithm group based on independent studies done at DØ (30). For my analysis, I carried out an independent cut optimization study with respect to the expected limit at 95% confidence level to check the possibility of improving the result (i.e. better limit). The optimization study was done for the 'isolation' and 'shower shape' cuts only. More details on limit and limit calculation will be discussed in Chapter 7. Figure 5·1 and 5·2 show the expected limit calculated for graviton masses 200 GeV and 500 GeV respectively for different values of the isolation cut. Figures 5·3 and 5·4 show the expected limit calculated for graviton masses 200 GeV and 500 GeV respectively for different values of the shower shape (7×7 H-matrix) cut. The error bars on the expected limit show the standard deviation. From these plots, we do not see any minima for 'isolation' and 'shape' cuts (with the error band) that give a significantly better limit. Hence we conclude that the isolation and shower shape cuts used ($f_{iso} < 0.07$ and 7×7 H-matrix $\chi^2 < 12$) are at least very close to the optimal settings.

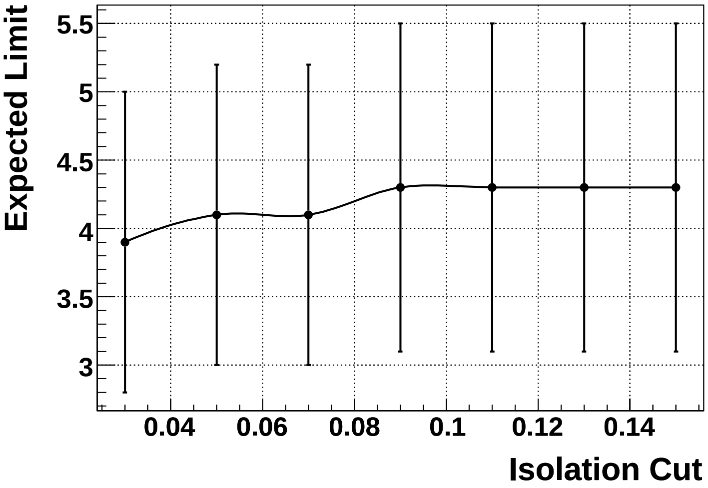

Figure 5·2: Expected limit at 95% confidence level as a function of Isolation cut for graviton mass of 500 GeV. The error bars on the expected limit show the standard deviation.

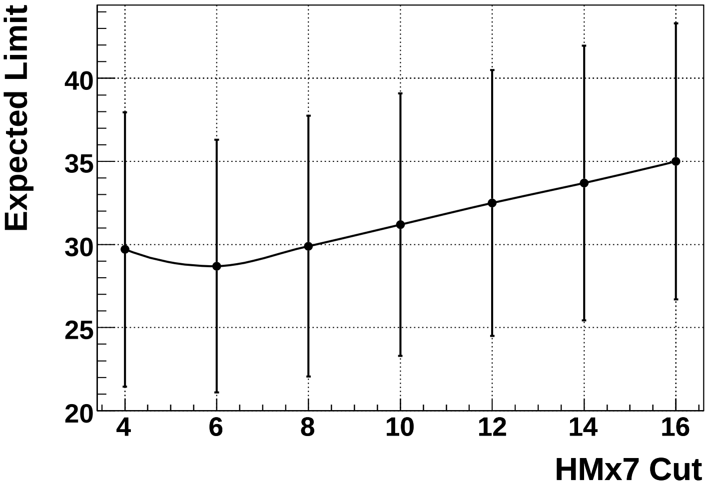

Figure 5·3: Expected limit at 95% confidence level as a function of HMx7 cut for graviton mass of 200 GeV. The error bars on the expected limit show the standard deviation.

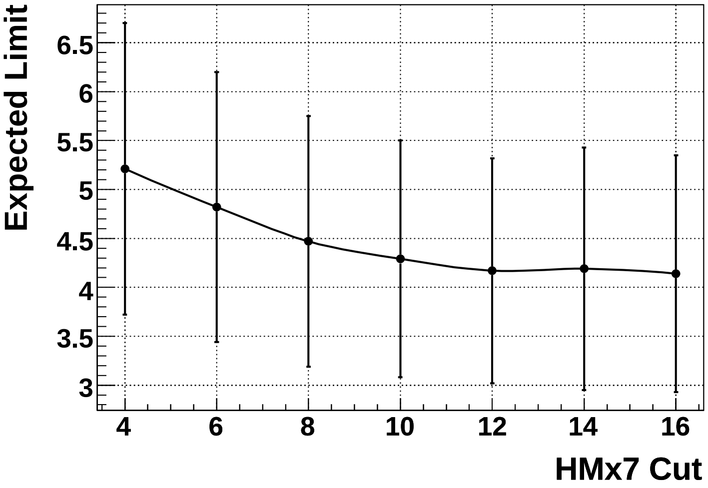

Figure 5·4: Expected limit at 95% confidence level as a function of HMx7 cut for graviton mass of 500 GeV. The error bars on the expected limit show the standard deviation.

Chapter 6

BACKGROUND ESTIMATION

6.1 Sources of Background

The total background is made up of irreducible backgrounds with genuine e^+e^- and $\gamma\gamma$ final states and misidentification backgrounds in which one or both of the electromagnetic objects are misidentified.

The sources of irreducible backgrounds are Drell-Yan production of e^+e^- and direct $\gamma\gamma$ production. The contribution from irreducible background is estimated from the MC samples. In order to predict the shape of the invariant mass spectrum from the irreducible backgrounds, the spectra from the four Drell-Yan and the four $\gamma\gamma$ MC samples are added according to their NLO cross sections. The NLO cross-section is obtained by multiplying the LO cross-section (Table 4.3) by a mass independent k-factor of 1.34(41). Here is a detailed description of how the total invariant mass spectrum is made for Drell-Yan MC:

- Apply the full selection cuts to each of the four Drell-Yan MC samples.
- For each sample, fill two sets of invariant mass plots for the selected events.
    - Low mass spectra with invariant mass between 50 and 250 GeV with a bin size of 1 GeV.
    - Full mass spectra with invariant mass between 50 GeV and 1000 GeV with a bin size of 10 GeV.
- The mass spectrum for each MC sample is scaled to the corresponding NLO cross-section. For example, the DY MC sample with $60 < M < 130$ GeV is scaled by 178 pb $\times$ $1.34/N_{generated}$, where $N_{generated} = 264750$ from Table 4.3.

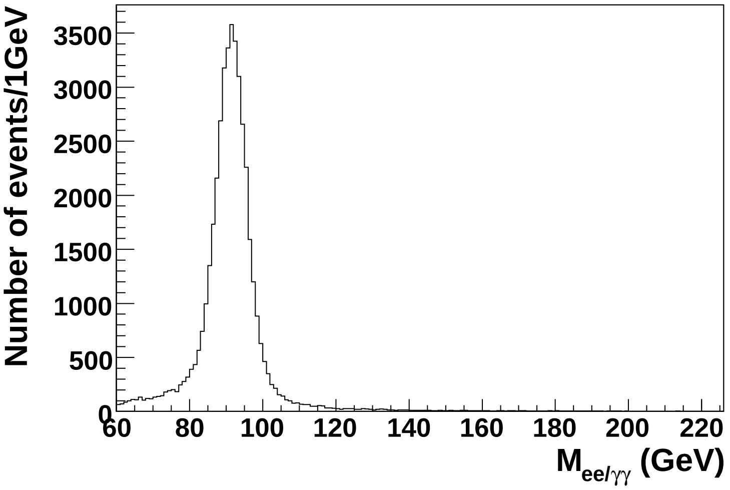

Figure 6·1: Invariant mass spectrum from total irreducible background (number of event is not important).

- All the four MC samples are individually scaled in this way and then added to get the Drell-Yan background shape.

Similarly, the direct diphoton background shape is also obtained. Then the Drell-Yan and diphoton total mass spectra are added to get the total irreducible background shape (Figure 6·1).

The misidentification background is estimated from a sub sample of the preselected data sample from section 4.1 in which at least one electromagnetic object is inconsistent with an electromagnetic shower. The selection cuts are:

- ID = 10 or 11
- detector $|\eta| < 1.1$
- $p_T > 25$ GeV
- 7×7 H-matrix $\chi^2 > 20$

This rejects events with genuine electrons or photons and provides us with an estimate of

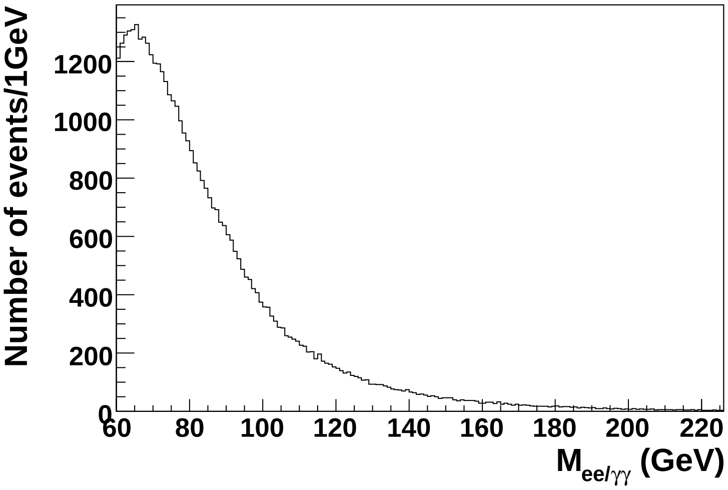

Figure 6·2: Invariant mass spectrum from misidentification background (number of event is not important).

the shape of the invariant mass spectrum of events with misidentified electrons and photons (Figure 6·2). To study the sensitivity to the specific cut values, two alternate sets of cuts were also studied in addition to the default cut above.

- Alternate cut 1 (set 1) : At least one electromagnetic object with 7 × 7 H-matrix $\chi^2 > 35$
- Alternate cut 2 (set 2) : Both electromagnetic objects with 7 × 7 H-matrix $\chi^2 > 20$
- Default cut (set 3)

It was found that the change in the total background prediction between these samples is negligibly small (Table 6.1). Figure 6·3 shows the misidentification background distribution for the three different selections. Figure 6·4 shows the ratios of the misidentification background spectra.

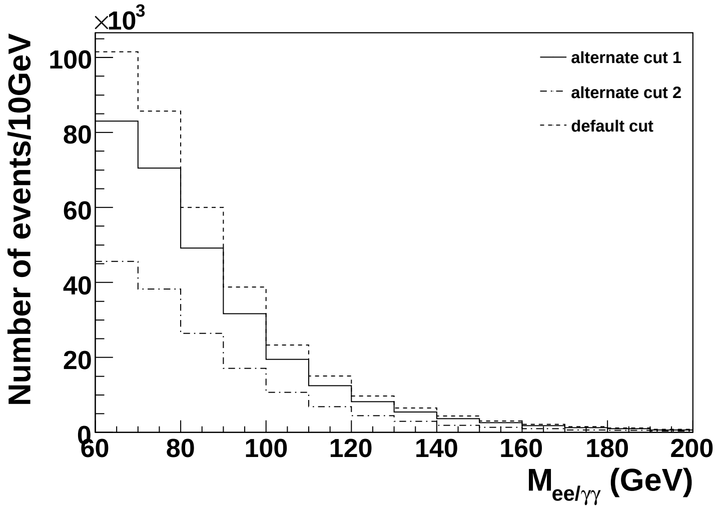

Figure 6·3: misidentification background distribution for the three different selections.

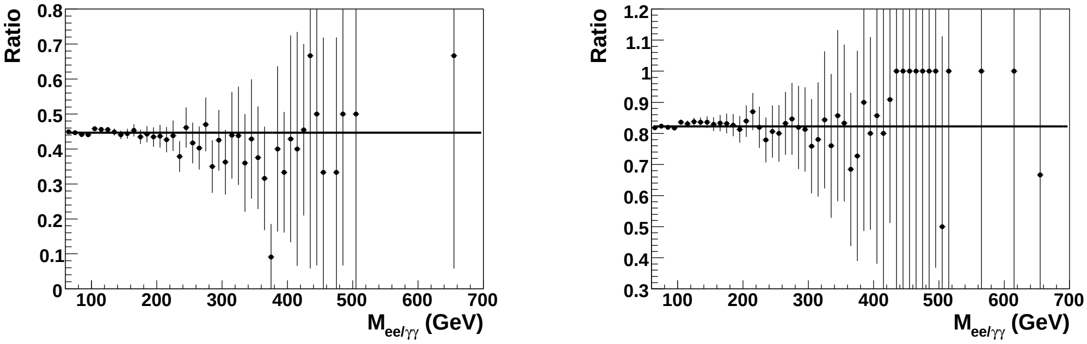

Figure 6·4: Ratio of the misidentification background spectra for Set2/Set3 (left) and for Set1/Set3 (right).

Graviton Mass (GeV)	Mass Window (GeV)	background events		
		alternate cut 1	alternate cut 2	default cut
200	190-210	82.2	88.1	83.8
300	280-320	26.6	26.0	26.9
400	380-420	5.9	5.8	5.9
500	450-550	5.5	5.4	5.3
600	550-650	1.9	1.9	1.8
700	620-780	0.8	0.9	0.8

Table 6.1: Total number of predicted background events for different selections of misidentification background.

6.2 Fit to the Low Mass Region

In order to fix the background shape, we fit the invariant mass spectrum observed in collider data around the Z peak (Figure 6·5) in the interval $60 < m(ee) < 140$ GeV with a superposition of the irreducible background shape and the misidentification background shape. Around the Z peak no new physics is expected. Therefore the total data should be well represented by a weighted sum of the total irreducible background and the misidentification background.

$$h_{bkg} = f \times h_{inst} + (1-f) \times h_{phys}. \tag{6.1}$$

Here h_{inst} and h_{phys} are the normalized invariant mass spectra from misidentification and irreducible background respectively. The parameter f is varied to minimize the χ^2 between h_{bkg} and the invariant mass spectrum from the collider data, h_{data}. The minimization is done with root using TMinuit. The χ^2 is calculated as follows

$$\chi^2 = \sum_i \frac{(n_i - \mathrm{N}(f \times a_i + (1-f) \times b_i))^2}{\delta^2}, \tag{6.2}$$

where

$$\delta^2 = n_i + \left(\frac{\mathrm{N}f}{\mathrm{N}'}\right)^2 n_i' + \left(\frac{\mathrm{N}(1-f)}{\mathrm{N}''}\right)^2 n_i''. \tag{6.3}$$

.

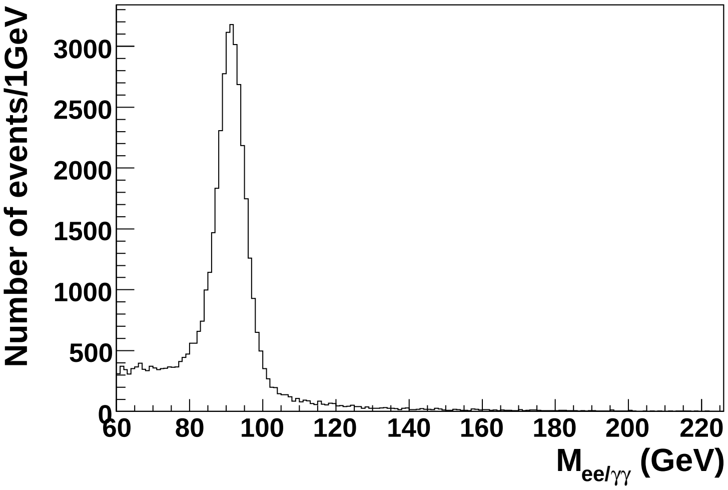

Figure 6·5: Invariant mass spectrum from data (number of event is not important).

- number of data events in bin $i = n_i$
- total number of data events within the fit range = N $= \sum_i n_i$
- number of misidentification background events in bin $i = n'_i$
- total number of misidentification background events within the fit range = N$'$ $= \sum_i n'_i$
- contents of bin i of the normalized misidentification background spectrum $= a_i = n'_i/\mathrm{N}'$
- number of irreducible background events in bin $i = n''_i$
- total number of irreducible background events within the fit range $= \mathrm{N}''_i = \sum_i n''_i$
- contents of bin i of the normalized irreducible background spectrum $= b_i = n''_i/\mathrm{N}''$

Here, the sum is over the number of bins i within the fit range 60 GeV $<$ mass $<$ 140 GeV. It is found that the best agreement is reached for $f = 0.199 \pm 0.004$. Figure 6·6 shows

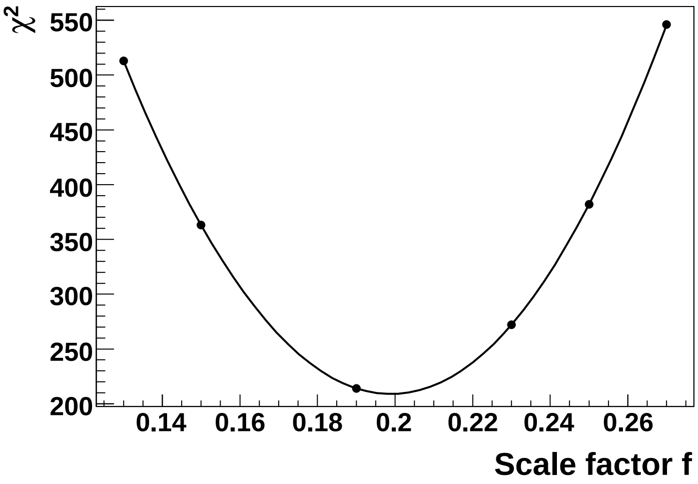

Figure 6·6: χ^2 vs scale factor f for misidentification background.

the plot of χ^2 vs f. Figures 6·7 and 6·8 show the invariant mass spectra for data and the fitted background composition superimposed.

6.3 Full Mass Spectrum

Finally, having normalized the physics and misidentification background contributions, we can predict the shape of the invariant mass spectrum above 140 GeV and compare to collider data. This is done by applying the same scale factor $f = 0.199$ to the full invariant mass spectrum of misidentification background and a scale factor of (1-f) to the full invariant mass spectrum of irreducible background. Adding these two weighted mass distributions gives the total background spectrum. Figure 6·9 shows the full mass spectra for data, the total background and the misidentification background contributions. Table 6.2 lists the number of events expected and observed above a number of invariant mass thresholds.

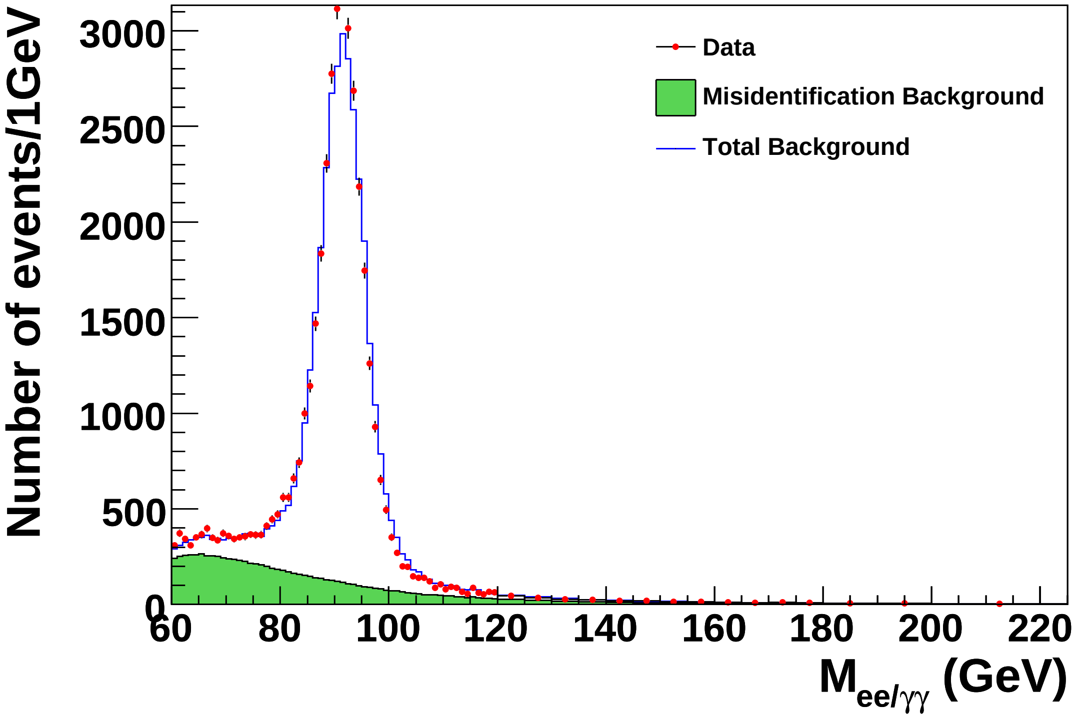

Figure 6·7: Invariant mass spectrum from data (points) with the fitted total background shape (open histogram) and the fitted contribution from misidentification backgrounds (shaded histogram) superimposed.

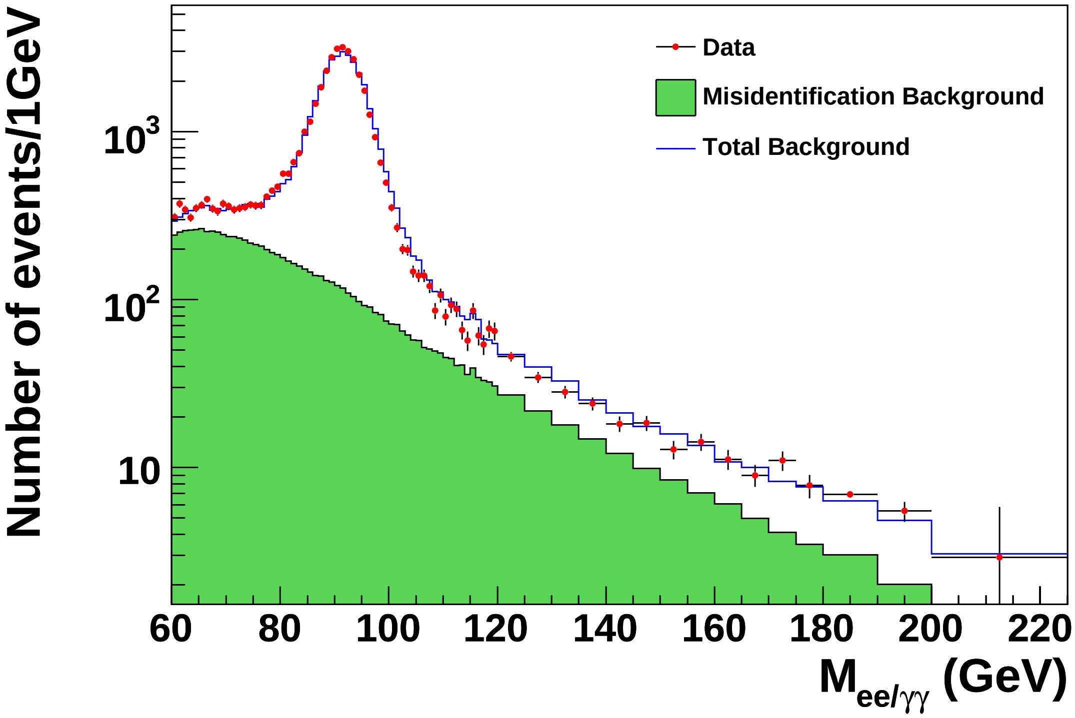

Figure 6·8: Invariant mass spectrum from data (points) with the fitted total background shape (open histogram) and the fitted contribution from misidentification backgrounds (shaded histogram) superimposed.

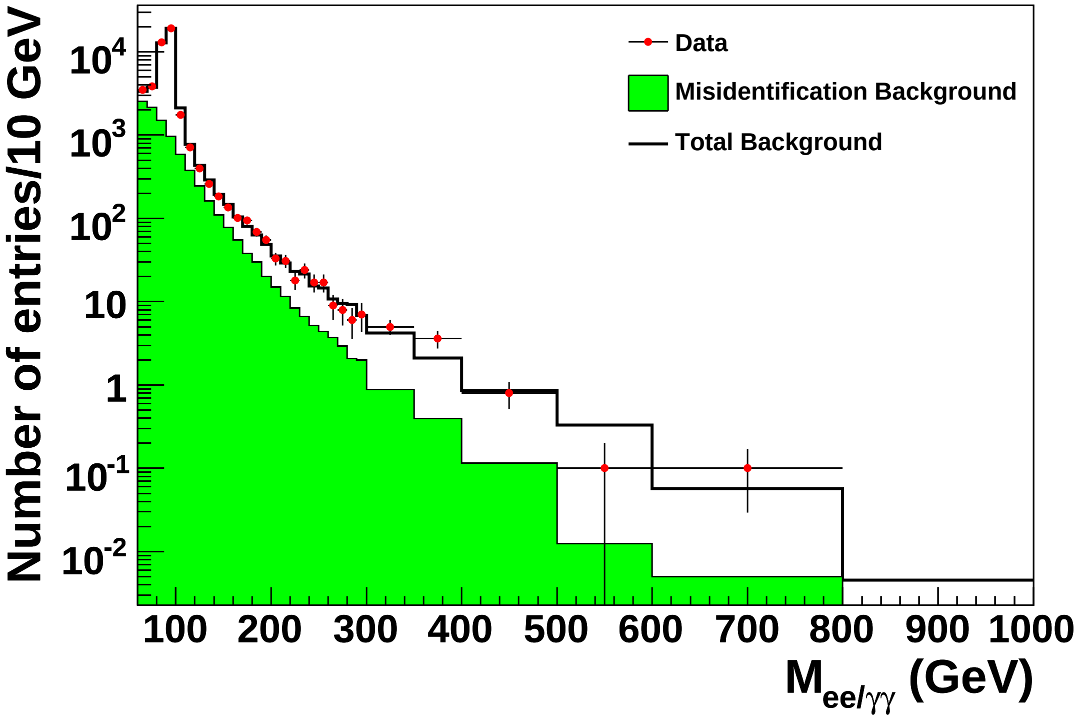

Figure 6·9: Invariant mass spectrum from collider data (points) with expected total background (open line histogram) and misidentification background (shaded histogram) superimposed.

M(GeV) >	60	100	140	150	200	250	300	350	400	450	500
Data	43639	3994	861	678	224	101	54	29	11	5	3
Total Background	43641	4513	863	667	221	95.7	44.7	23.5	13	7.5	4.5

Table 6.2: Number of data and background events above a mass threshold for the full mass spectra.

6.4 Smearing Monte Carlo

The energy of the simulated electromagnetic object is required to be smeared to have better agreement to the data. This is due to the fact that the energy obtained for a simulated object does not properly describe the different detector effects. For this analysis, already smeared monte carlo samples were used. However an independent study was also done for the smearing. The relation between the smeared energy (E') and the energy of an object from the simulated events (E) is given by the equation:

$$E' = E \times [\alpha + Gauss(0, \alpha\beta)] \tag{6.4}$$

The set of parameters used for this smearing are α and β. This study was done to find the set of parameters that will result in the best match between data and MC. First the invariant mass plots around the Z peak for MC and data were compared without any smearing. The agreement was as good as shown in Fig. 6·10. Next the Z/DY MC sample was smeared using α and β corresponding to the p14 DØ reconstruction version. The p14 parameters are $\alpha = 1.007$ and $\beta = 0.042$. With these values, the agreement between data and MC was also not very good as shown in Fig 6·11.

Optimization of Parameters

Next, a systematic study was done to optimize the values for the two parameters using data and MC reconstructed with DØ reconstruction version p17. The MC sample was smeared with a set of values for α and β and the corresponding χ^2 was calculated. First α was kept fixed at 1.001 and β was changed and a plot of χ^2 vs β was obtained (Fig 6·12).

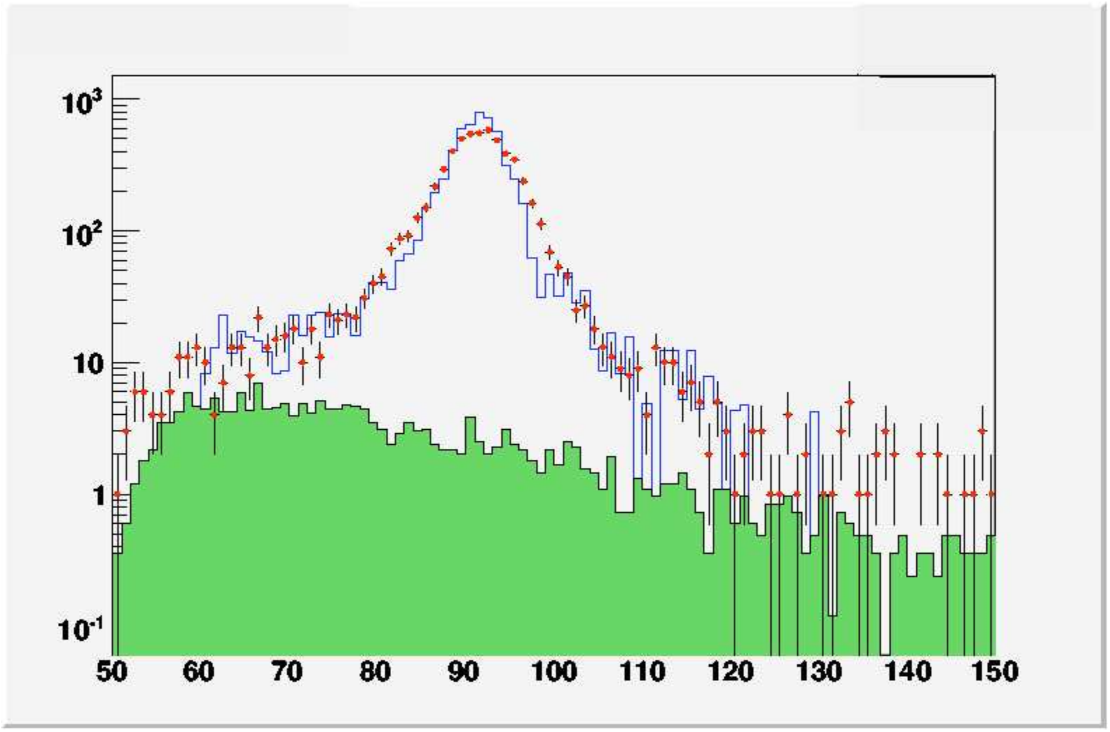

Figure 6·10: Invariant mass spectrum from data (points) with the fitted total (DY+Instrumental) background shape (open histogram) and the fitted contribution from misidentification backgrounds (shaded histogram) superimposed without smearing.

From this plot the value of β=0.024, corresponding to the minimum χ^2 was chosen. Next the value for β was kept fixed at 0.024 and α was varied. From the plot of χ^2 vs α the best value for α was obtained (Fig 6·13). The values of α and β that provided best MC-data agreement were found to be $\alpha = 1.003$ and $\beta = 0.024$.

Smearing the MC with these set of parameters shows good agreement between data and MC (Fig 6·14). The official DØ parameters $\alpha = 1.004$ and $\beta = 0.03$, are comparable to the values obtained by this study. In this analysis, the official DØ parameters were used.

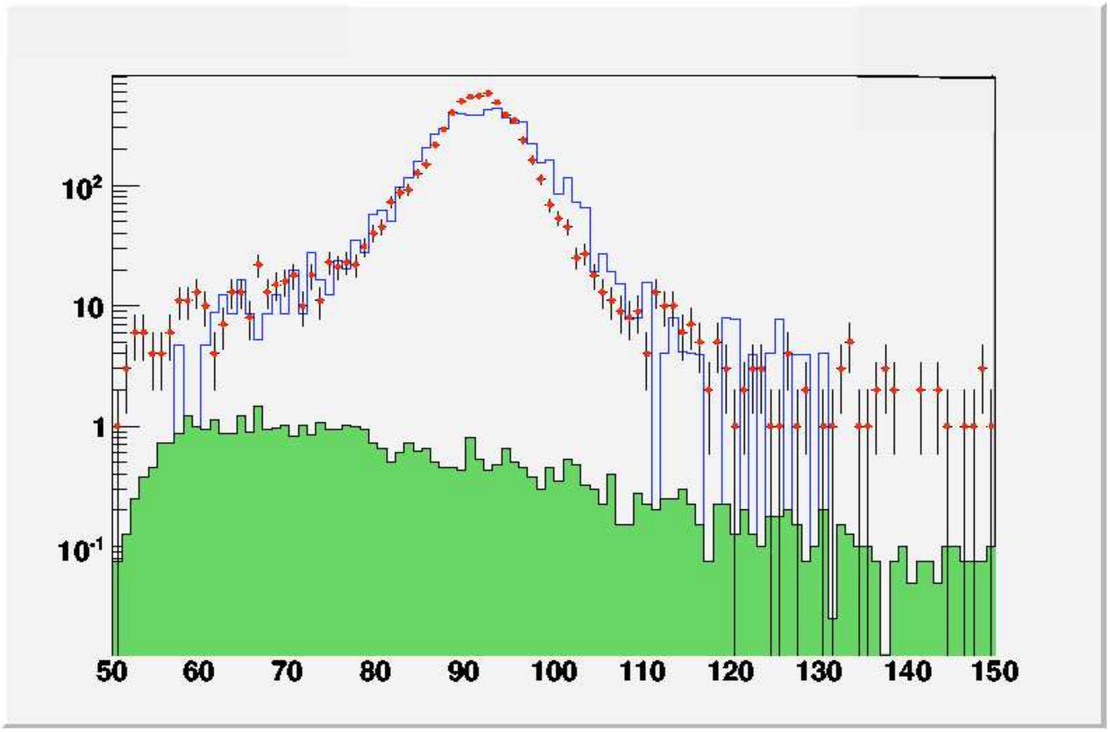

Figure 6·11: Invariant mass spectrum from data (points) with the fitted total (DY+Instrumental) background shape (open histogram) and the fitted contribution from misidentification backgrounds (shaded histogram) superimposed smeared with p14 parameters.

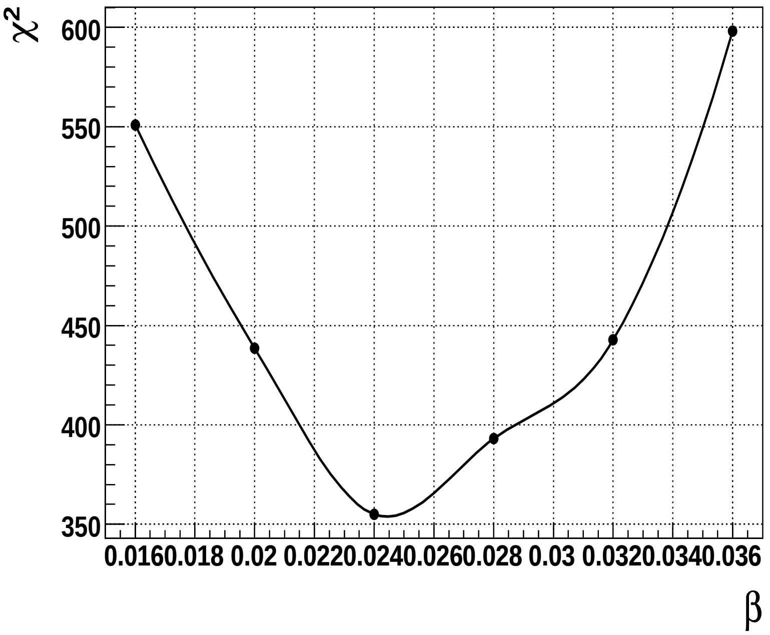

Figure 6·12: χ^2 vs β with α=1.001(fixed).

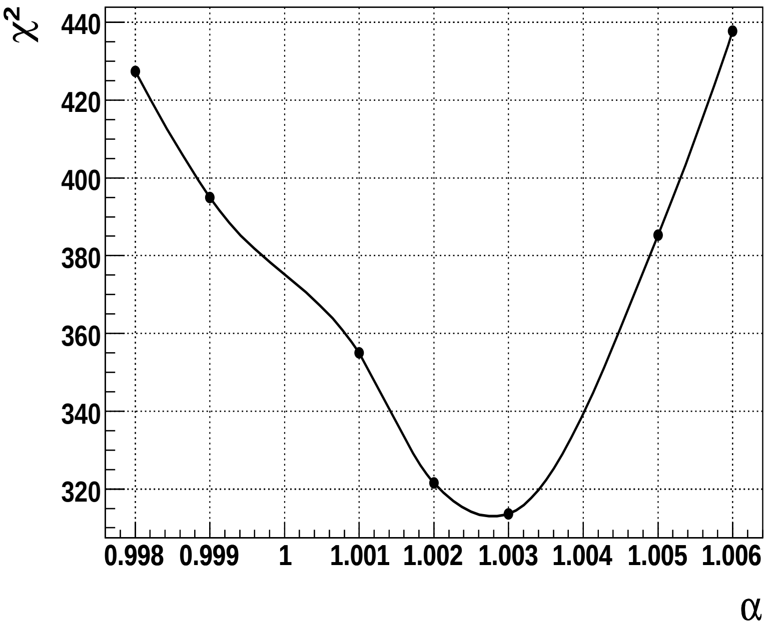

Figure 6·13: χ^2 vs α with β=0.024(fixed).

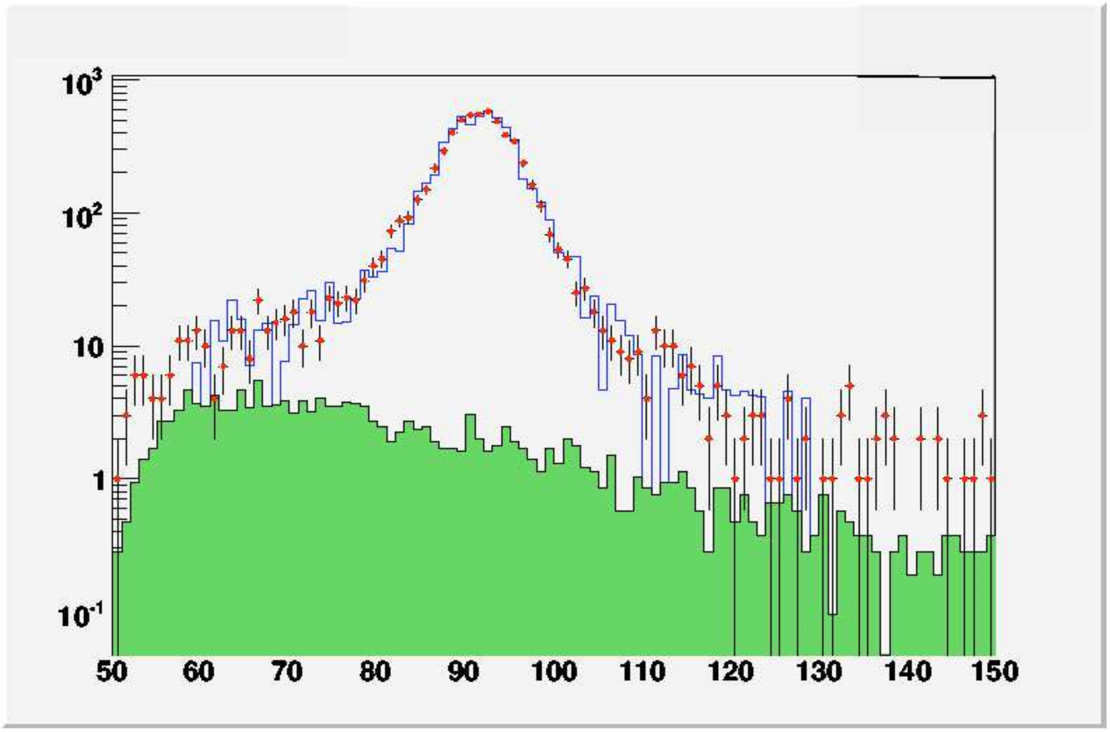

Figure 6·14: Invariant mass spectrum from data (points) with the fitted total (DY+Instrumental) background shape (open histogram) and the fitted contribution from misidentification backgrounds (shaded histogram) superimposed smeared with p17 parameters.

Chapter 7

LIMIT CALCULATION AND RESULT

The integrated luminosity of our data sample was extracted from the scale factor for the DY spectrum determined in section 6.2. The number of SM (irreducible) background events (DY+diphoton) is equal to N (equation 7.1), where we use the following definitions.

- Number of generated Drell-Yan MC events (Sample generated with invariant mass between 60 and 130 GeV) : N_{DY}
- Number of generated Diphoton MC events (Sample generated with invariant mass between 50 and 130 GeV): $N_{\gamma\gamma}$
- Drell-Yan NLO cross-section : σ_{NLO}^{DY}
- Diphoton NLO cross-section : $\sigma_{NLO}^{\gamma\gamma}$
- Number of data events with invariant mass between 60 GeV and 140 GeV : A
- Number of Drell-Yan Monte Carlo events with invariant mass between 60 GeV and 140 GeV : B
- Number of diphoton Monte Carlo events with invariant mass between 60 GeV and 140 GeV : C
- The total number of Drell-Yan and diphoton events in data is $N = A \times (1 - f)$ where f is the scale factor from section 6.2.
- The correction factor 'r' to account for the difference in efficiency between MC and data (detail in section 8.3).

$$N = \mathcal{L} \times \frac{1}{r^2} \left(\sigma_{NLO}^{DY} \times \frac{B}{N_{DY}} + \sigma_{NLO}^{\gamma\gamma} \times \frac{C}{N_{\gamma\gamma}} \right). \tag{7.1}$$

The leading order (LO) cross section listed in Table 4.3 was taken and a mass independent k-factor of 1.34 was assumed(41) to get the next to leading order (NLO) cross-section. The integrated luminosity ($\mathcal{L}$) is calculated solving equation 7.1 for $\mathcal{L}$. The calculated integrated luminosity with the numbers listed in Table 7.1 is 0.985 ± 0.035 fb^{-1}.

N_{DY}	$\sigma_{NLO}^{DY}(pb)$	B	$N_{\gamma\gamma}$	C	$\sigma_{NLO}^{\gamma\gamma}(pb)$	A	f	r
264750	178×1.34	40732	50500	923	42.7×1.34	42778	0.199	0.96

Table 7.1: Values for integrated luminosity calculation.

The signal acceptance was obtained from RS graviton MC. For a given graviton mass, the acceptance is defined by:

$$\epsilon_{total} = \frac{N_{pass}}{N_{total}}, \tag{7.2}$$

where N_{total} is the total number of MC events generated for a given graviton mass, and N_{pass} is the number of MC events that pass all the selection cuts and mass window cuts. This efficiency is further corrected to account for the difference between data and Monte Carlo by a correction factor of r=0.96 (detail in section 8.3). The mass window cuts applied for the different mass points are listed in the Table 7.2. These mass windows are optimized based on the prescription described in(31). In the first step, the invariant mass spectrum for each graviton mass sample is fitted with a gaussian and from that fit the width σ is obtained. Then the optimum mass window, following the prescription (31) is $2 \times \sigma$. If the expected number of background events is less than 1, the mass window used is $3 \times \sigma$. The window size has been rounded to match the histogram bin size of 10 GeV. As a cross check, we also carried out a separate study by trying different mass windows and calculating the corresponding expected limits. Figure 7·1 and 7·2 shows the expected limit as a function of the width of the mass window for $M_1 = 200$ GeV and 500 GeV respectively and supports the mass window obtained following the prescription (31) (±10 for 200 GeV and ±50 GeV

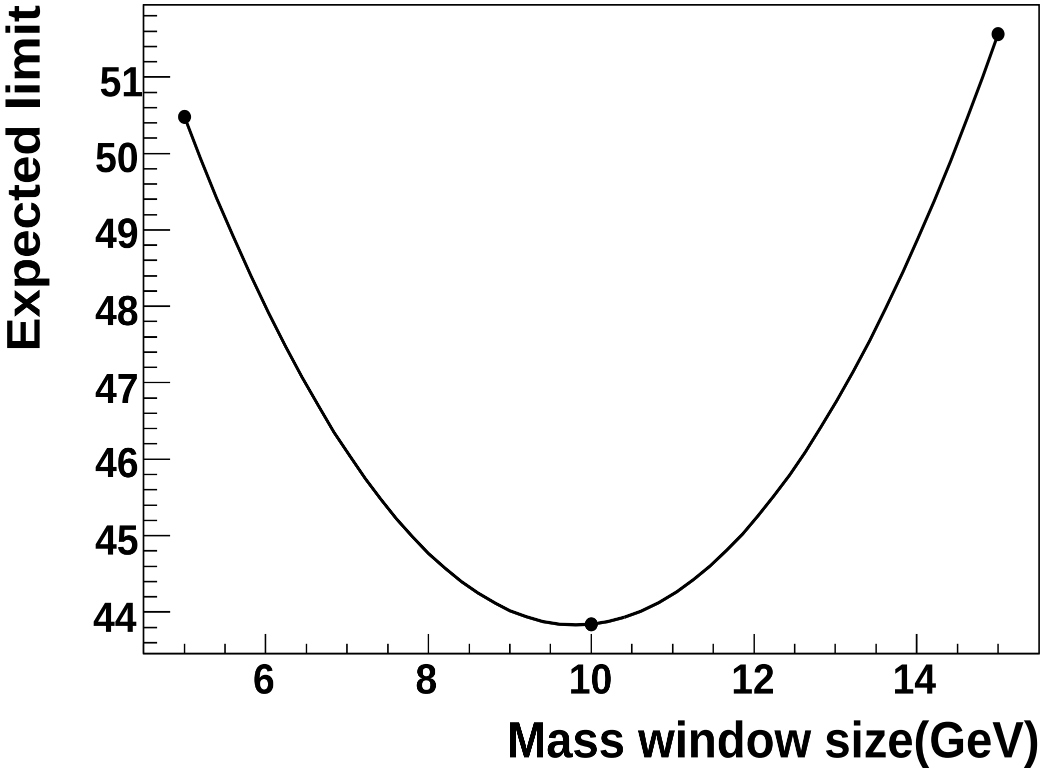

Figure 7·1: Expected limit as a function of mass window for mass point 200 GeV.

for 500 GeV graviton). The error bars on the expected limit show the standard deviation.

The number of data and expected background events were calculated by integrating the invariant mass spectra (Fig. 6·9) for data and total background over different mass windows corresponding to each graviton mass. The results are listed in Table 7.2. The systematic uncertainties used for the limit calculation are listed in Table 7.3 and the details are discussed in chapter 8.

The Bayesian Limit calculator (a computer code used to calculating limit at DØ)(32), was used to calculate the lower limit on the cross section × branching fraction at 95% confidence level. The inputs for the Bayesian limit calculator for a given graviton mass are:

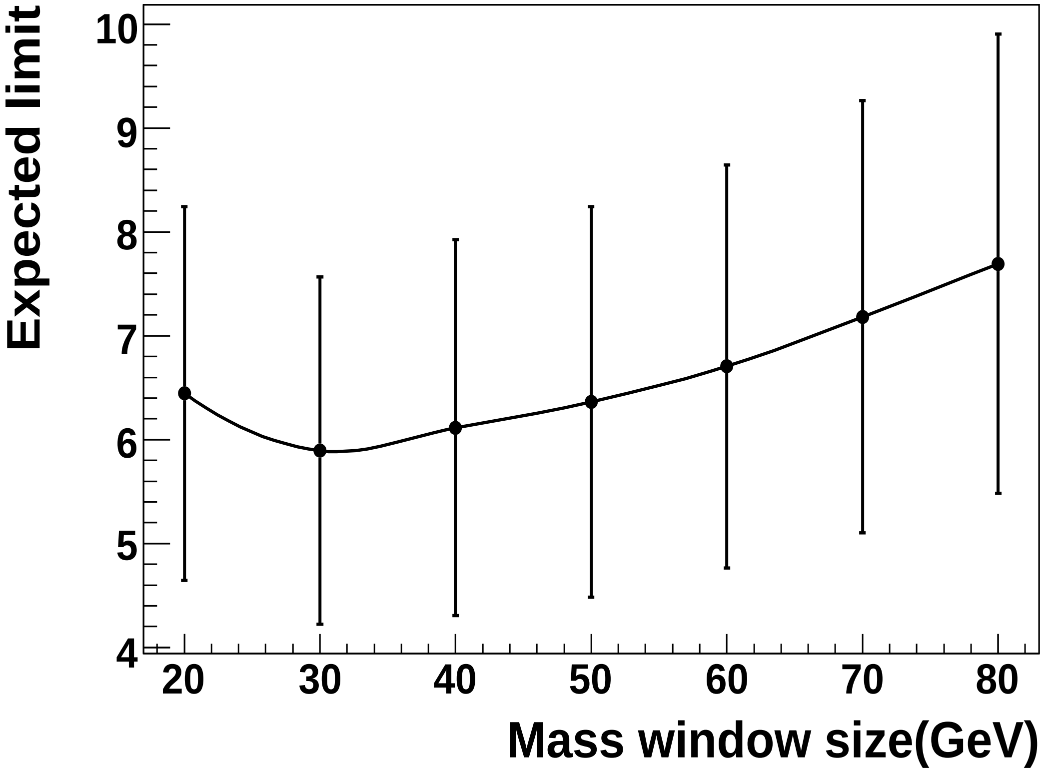

Figure 7·2: Expected limit as a function of mass window for mass point 500 GeV.

- Number of observed events within the mass window : n
- Number of expected (background) events within the mass window : b
- Signal acceptance : ϵ
- Integrated luminosity : $\mathcal{L}$
- Systematic uncertainties on b and ϵ

With these inputs, the limit calculator calculates the observed 95% confidence level upper limit on the cross-section. The expected limit for a given graviton mass is calculated by equating the number of observed events with the number of background events (i.e. $n = b$). For graviton masses for which the predicted number of background events is less then 5, we compute the poisson averaged expected limit

$$< \sigma_{95} >= \frac{\sum_{n=n_{min}}^{n=n_{max}} P_n \times \sigma_{95}^n}{\sum_{n=n_{min}}^{n=n_{max}} P_n} \tag{7.3}$$

Here P_n is the poisson probability to observe n events when b events are expected, $n_{min} = b - 2\sqrt{b}$, $n_{max} = b + 2\sqrt{b}$, and σ_{95}^n is the 95% confidence level upper limit on the cross section computed assuming n observed events.

Since we accept e^+e^- and $\gamma\gamma$ final states we obtain a limit on the sum of these two decay channels. The branching fraction to $\gamma\gamma$ is twice that to e^+e^-. We quote a limit on $\sigma(p\overline{p} \to G + X) \times B(G \to e^+e^-)$ which is therefore a third of the limit on $\sigma(p\overline{p} \to G + X) \times [B(G \to e^+e^-) + B(G \to \gamma\gamma)]$.

The results of the limit calculation are listed in Table 7.2. Figure 7·3 shows the 95% confidence level upper limit on $\sigma(p\overline{p} \to G + X) \times B(G \to e^+e^-)$ versus the graviton mass compared to the theoretical prediction. Here we use the LO cross section obtained with PYTHIA(33), multiplied by a mass independent k-factor of 1.34(41). Based on data from 0.985 fb^{-1}, we can thus exclude the existence of RS gravitons with masses upto 898(303) GeV at 95% confidence level for $\kappa/\overline{M}_{Pl} = 0.1(0.01)$. The published limit based on 275 pb^{-1} was 785(250) GeV for $\kappa/\overline{M}_{Pl} = 0.1(0.01)$. Figure 7·4 shows the upper limit on the coupling parameter $\kappa/\overline{M}_{Pl}$ as a function of graviton mass M_1. The total cross-section (graviton production cross-section × branching fraction) is proportional to the square of the coupling, $(\sigma \sim \left(\kappa/\overline{M}_{Pl}\right)^2)$. Using this relation, the following equation is obtained:

$$\frac{\left(\kappa/\overline{M}_{Pl}\right)_{95\%CL}}{0.1} = \sqrt{\frac{\sigma_{95\%CL}}{\sigma_{0.1}}} \tag{7.4}$$

With $\sigma_{0.1}$, the theoretical cross-section (graviton production cross-section × branching fraction) for coupling 0.1 and $\sigma_{95\%CL}$, the calculated 95% confidence level upper limit on the total cross-section, the 95% confidence level upper limit on coupling, $\left(\kappa/\overline{M}_{Pl}\right)_{95\%CL}$, is calculated as a function of the graviton mass.

Mass (GeV)	Mass Window (GeV)	Data	Total Background	ϵ_{Total} for signal	Cross Section (fb)			Coupling	
					theory	expected limit	observed limit	expected limit	observed limit
200	190-210	88	83.8±7.3	0.208±0.030	12730	43.9	51.0	0.0058	0.0063
220	210-230	49	52.3±4.7	0.214±0.033	7861	32.5	28.7	0.0064	0.0060
240	230-250	41	37.1±3.7	0.211±0.038	5181	28.1	34.3	0.0073	0.0081
250	240-260	34	30.1±3.1	0.215±0.038	4417	24.7	31.0	0.0074	0.0083
270	250-290	40	44.0±4.5	0.297±0.026	2988	21.6	18.0	0.0085	0.0077
300	280-320	29	26.9±3.0	0.310±0.029	1885	15.2	18.2	0.0089	0.0098
320	300-340	22	18.3±2.0	0.318±0.036	1371	12.6	16.9	0.0095	0.0110
350	330-370	15	11.4±1.2	0.311±0.034	902	10.2	14.8	0.0106	0.0128
370	350-390	16	8.7±0.96	0.316±0.039	688	8.6	18.8	0.0111	0.0165
400	380-420	7	5.8±0.69	0.319±0.042	473	7.0	9.3	0.0122	0.0140
450	420-480	6	4.8±0.58	0.366±0.021	259	6.5	7.6	0.0158	0.0171
500	450-550	3	5.3±1.01	0.419±0.014	147	5.6	4.2	0.0196	0.0168
550	500-600	1	3.3±0.89	0.434±0.015	84.9	4.8	3.1	0.0238	0.0193
600	540-660	1	1.84±0.22	0.454±0.017	53.6	3.8	3.1	0.0266	0.0242
650	590-710	2	1.04±0.13	0.437±0.013	31.3	3.4	4.5	0.0334	0.0381
700	620-780	2	0.84±0.10	0.458±0.013	18.3	3.1	4.4	0.0412	0.0493
750	660-840	1	0.51±0.06	0.473±0.015	11.2	2.7	3.4	0.0491	0.0551
800	700-900	1	0.32±0.04	0.474±0.015	6.2	2.6	3.4	0.0647	0.0746
850	750-950	0	0.18±0.02	0.481±0.013	3.9	2.4	2.2	0.0799	0.0768
900	790-1010	0	0.108±0.02	0.475±0.014	2.3	2.3	2.3	0.1010	0.1010
950	840-1060	0	0.059±0.01	0.474±0.012	1.3	2.3	2.3	0.1340	0.1340

Table 7.2: Number of expected and observed events in different mass windows, signal acceptance and upper limit on cross section × branching ratio.

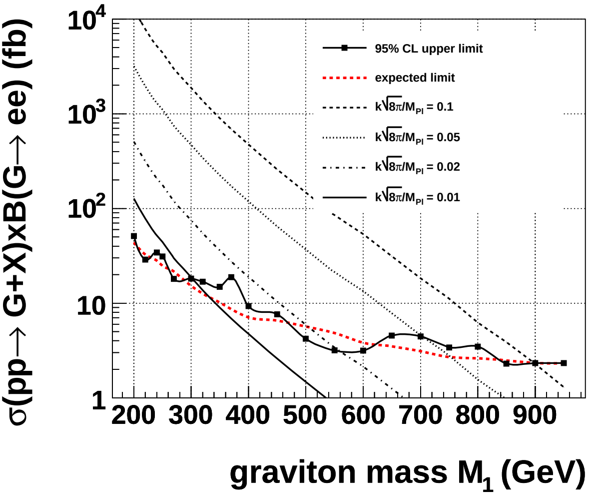

Figure 7·3: 95% confidence level upper limit on $\sigma(\overline{p} \rightarrow G+X) \times B(G \rightarrow e^+e^-)$ from 1 fb^{-1} of data compared with the sensitivity and the theoretical predictions for different couplings $\kappa/\overline{M}_{Pl}$.

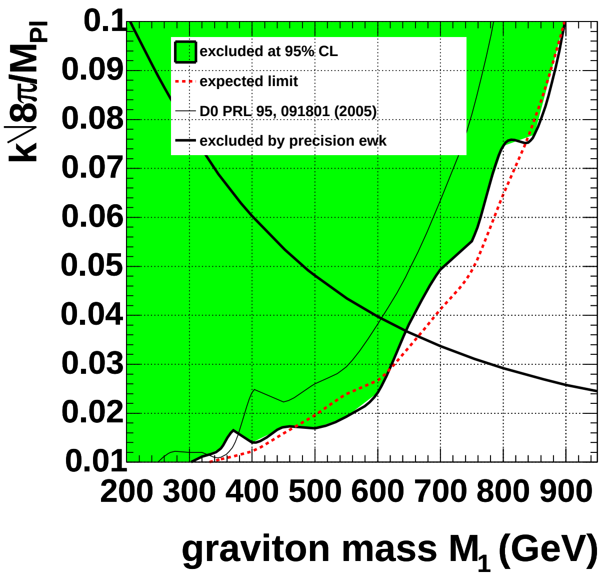

Figure 7·4: 95% confidence level upper limit on $\kappa/\overline{M}_{Pl}$ versus graviton mass M_1 from 1 fb^{-1} of data compared with the expected limit and the previously published exclusion contour(18).

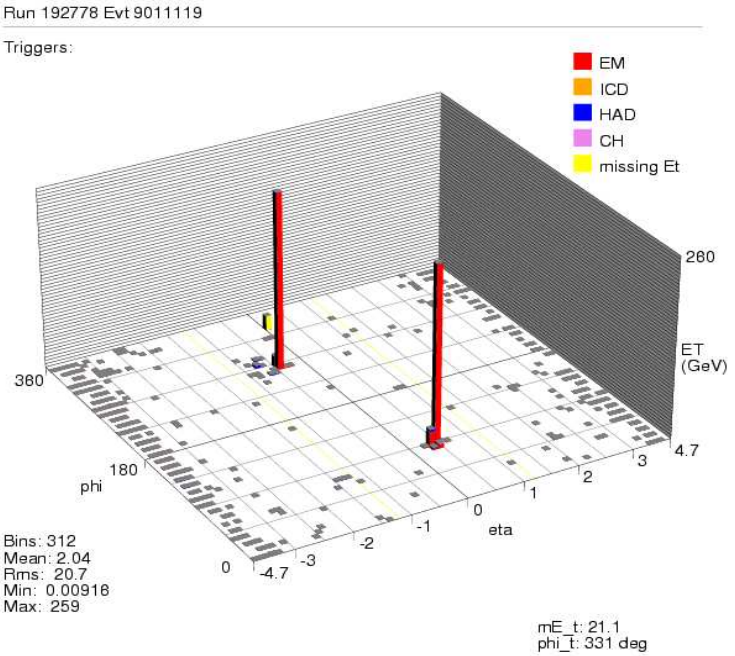

Figure 7·5: Second-highest mass candidate event (Mass = 653.4 GeV) for RS graviton decay to $e^+e^-/\gamma\gamma$ from this analysis. Event display shows calorimeter energy in $\eta - \phi$ plane.

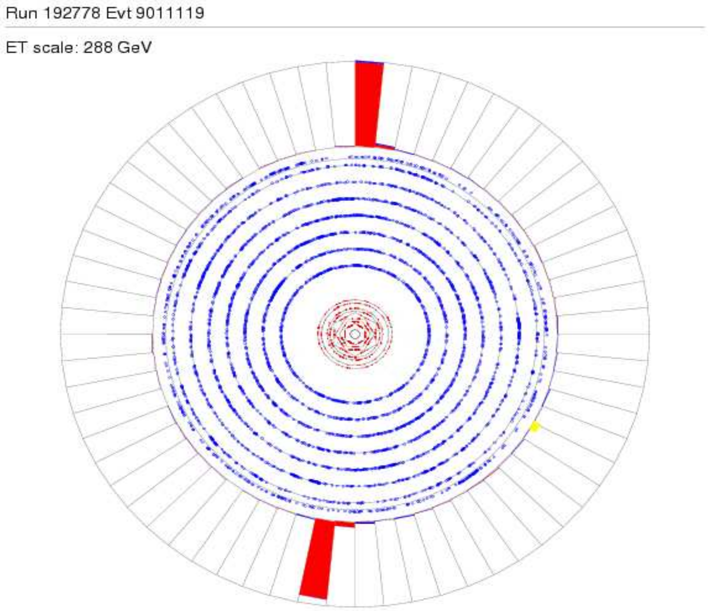

Figure 7·6: Second-highest mass candidate event (Mass = 653.4 GeV) for RS graviton decay to $e^+e^-/\gamma\gamma$ from this analysis. Event display shows calorimeter energy in $X-Y$ plane.

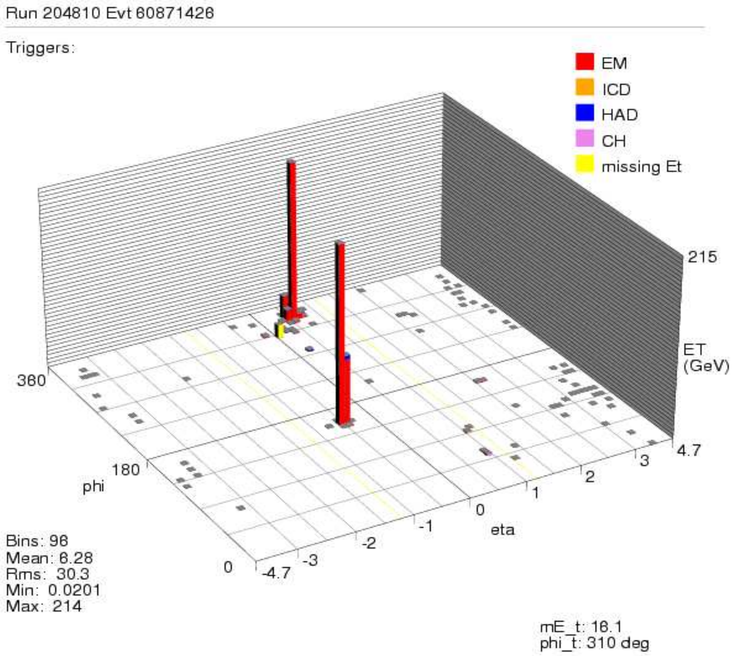

Figure 7·7: Highest mass candidate event (Mass = 708.9 GeV) for RS graviton decay to $e^+e^-/\gamma\gamma$ from this analysis. Event display shows calorimeter energy in $\eta - \phi$ plane.

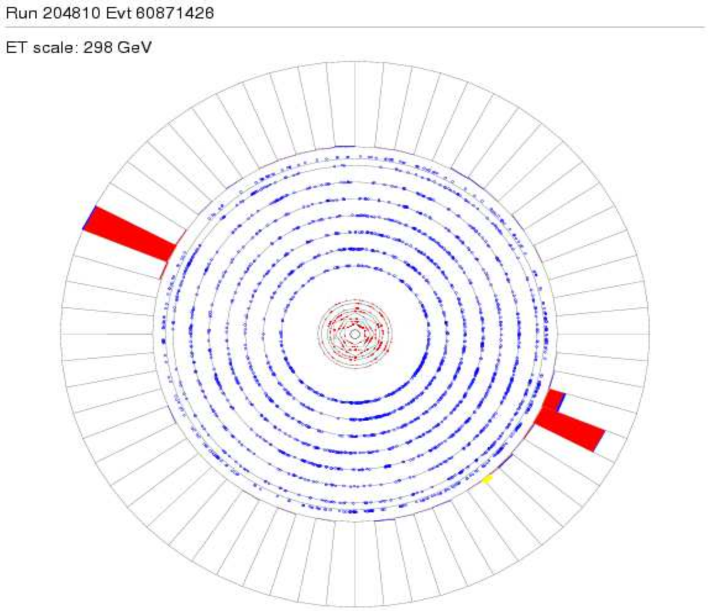

Figure 7·8: Highest mass candidate event (Mass = 708.9 GeV) for RS graviton decay to $e^{+}e^{-}/\gamma\gamma$ from this analysis. Event display shows calorimeter energy in $X-Y$ plane.

Source of Signal Uncertainty	Uncertainty
pdf uncertainty	$0.2\% - 5.5\%$
Resolution	$1\% - 11.1\%$
EM ID uncertainty	1.4%
Statistical uncertainty	0.5%
Total	$2\% - 12.4\%$
Source of Background Uncertainty	**Uncertainty**
k-factor mass dependence	5.2%
Error on f due to trigger	6%
Statistical uncertainty	2% - 24%
Uncertainty on relative cross-section due to pdf	2% - 10%
Total	8.4%-27%

Table 7.3: Sources of uncertainty for signal and background.

Chapter 8

SYSTEMATICS

The systematic uncertainties from different sources are listed in table 7.3. Here I describe in detail how they were determined.

8.1 Uncertainty due to trigger efficiency

From previous studies (34) it is known that the EM triggers are almost 100% efficient at high mass. In the previous RS Graviton search (18) at DØ the trigger was taken to be fully efficient mainly because this analysis is only concerned with high P$_T$ EM objects. In the following, we estimate the effect of the trigger thresholds and show that they are indeed small.

- We use data from eight different trigger conditions, that were in effect during different time periods at D0. Every time period corresponds to a trigger version. The eight triggers, their corresponding trigger versions and the integrated luminosity corresponding to each of these triggers, are listed in Table 8.1.
- The trigger efficiencies as a function of transverse momentum (p_T), were obtained from an independent trigger efficiency study done at DØ (29). Figure 8·1 shows the turn-on curves for the four single electron triggers used for this study.
- For a given single electron trigger, the total efficiency was calculated using the following equation:

$$\epsilon_{Total} = \epsilon_1 \times (1 - \epsilon_2) + \epsilon_2 \times (1 - \epsilon_1) + \epsilon_1 \times \epsilon_2. \tag{8.1}$$

Trigger	Trigger name	Trigger version	Integrated luminosity pb^{-1}
Single-EM	EM_MX_SH	V8 to V11	122
	E1_SH30	V12 and V13	596
	E1_SHT22	V13	377
	E1_SH35	V14	350
Di-EM	2EM_HI	V8 to V11	122
	E1_2L15_SH15	V12 and V13	596
	E1_2L20	V12 and V13	596
	E1_2L20_L25	V14	350

Table 8.1: List of triggers that pass 97% of the skimmed data.

Here, ϵ_1 and ϵ_2 are the trigger efficiencies for the two electromagnetic objects in a selected event. The total efficiency for a given event to fire a single electron trigger is the probability that one or both electromagnetic objects will pass the trigger.

- Calculate the integrated luminosity weighted average for the four trigger versions using the equation :

$$\mathcal{W}_{Total} = \frac{\epsilon_{Total}^{EM\_MX\_SH} \times 122pb^{-1} + \epsilon_{Total}^{E1\_SH30} \times 219pb^{-1} + \epsilon_{Total}^{E1\_SHT22} \times 377pb^{-1} + \epsilon_{Total}^{E1\_SH35} \times 350pb^{-1}}{1068pb^{-1}}. \tag{8.2}$$

  This gave the total probability (weight) that the selected event will pass a logical OR of these four single EM triggers.

- The total background invariant mass spectrum is obtained with non-weighted MC as described in chapter 6.

- Next, the Drell-Yan and Diphoton Monte Carlo invariant mass spectra are obtained applying the weights calculated ($\mathcal{W}_{Total}$) and then the total background invariant mass spectrum is obtained using these weighted MC.

- Compare the two distributions.

Figure 8·2 shows the plot comparing the mass spectra of the total background with weighted and non-weighted Monte Carlo. The effect of the trigger weights was checked in the low mass region, which is used to fit the misidentification background to calculate the

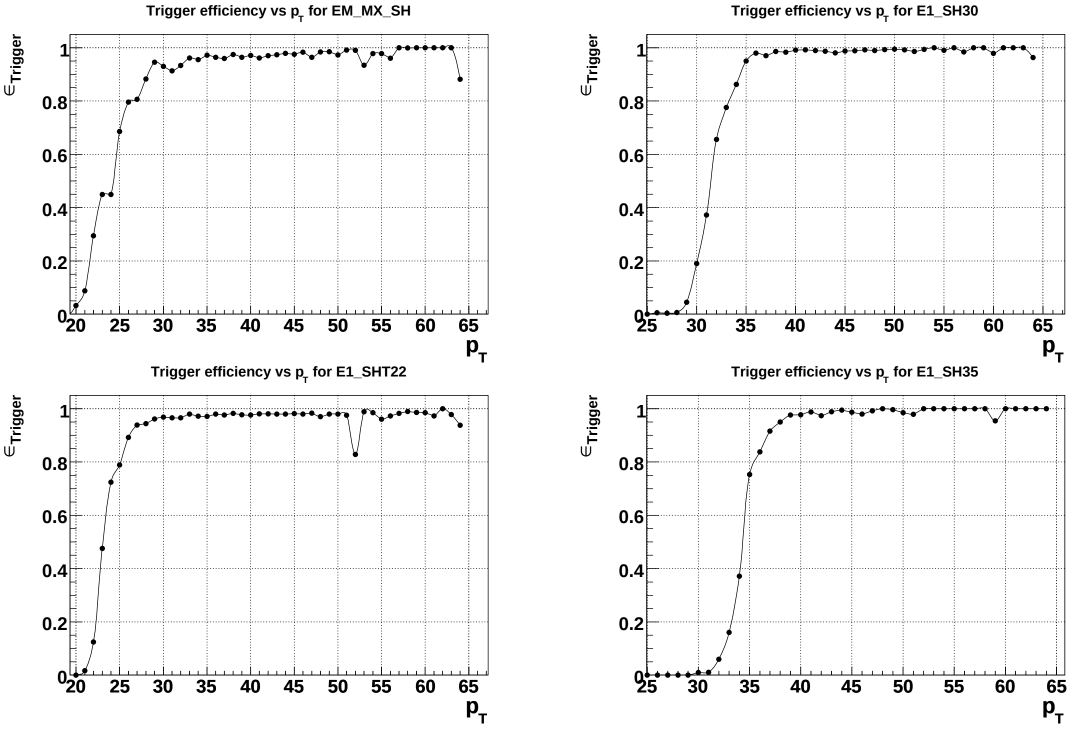

Figure 8·1: Trigger turn-on curves for EM_MX_SH (top left), E1_SH30 (top right), E1_SHT22 (bottom left), and E1_SH35 (bottom right)(29).

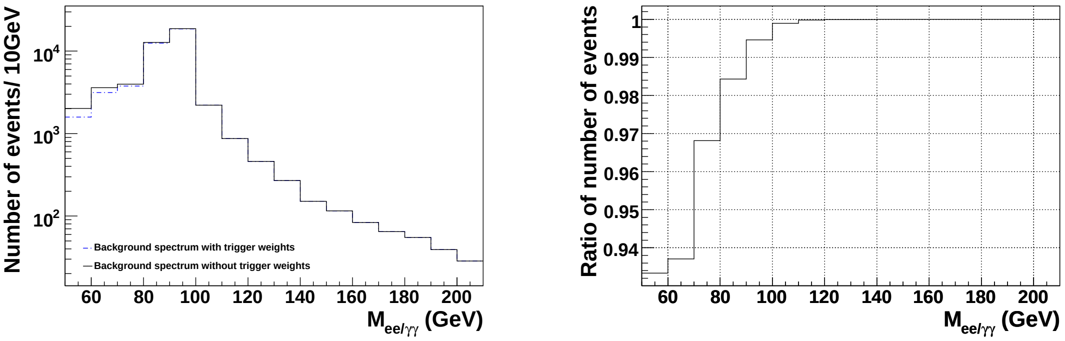

Figure 8·2: Comparison of the mass spectra for total background with trigger weights and without trigger weights. At higher masses the spectra are identical.

integrated luminosity as described in chapter 7. The difference in the integrated luminosity calculated using weighted Monte Carlo and non-weighted Monte Carlo came out to be less than 1% (Table 8.2). Also, the change in total predicted background with and without the trigger turnons is only a few percent as shown in Table 8.3. This exercise used only the single electron trigger. We also include dielelctron triggers which would further increase the trigger efficiencies and reduce the effect of the trigger.

	with trigger turnon	without trigger turnon	change (%)
f	0.211	0.199	6
Integrated luminosity	987 pb^{-1}	985 pb^{-1}	0.2

Table 8.2: Change in f and in integrated luminosity with and without trigger turnons.

8.2 Uncertainty due to resolution

To calculate the signal efficiency, a mass window cut is applied. The signal acceptance of this mass window depends on the resolution with which we measure the invariant mass of the two EM objects. The uncertainty in the acceptance of the mass window due to the energy resolution is estimated as follows. First the Δp_T distribution for the two electromag-

Graviton Mass (GeV)	Total background (with trigger turnon)	Total background (without trigger turnon)	$\Delta b/b$ %
200	86.2	83.8	2.8
300	27.4	26.9	1.8
400	5.97	5.89	1.3
500	5.38	5.33	0.9
600	1.85	1.84	0.5
700	0.84	0.84	0.0

Table 8.3: Change in total background (b) with and without trigger turnons.

netic objects is obtained. The variable Δp_T is the difference in the transverse momentum (p_T) between the two EM objects in a selected event. The idea behind this is, the two electromagnetic objects selected after the selection cuts are expected to be back to back with Δp_T of zero on average. The width of the Delta pT distribution then is an indicator of the resolution with which the EM energies are measured. In order to reduce the background in the Δp_T distribution, a delta phi cut of $2.6 \leq \phi \leq 3.6$ is also applied in addition to the selection cuts. After that, the distribution is fitted with a gaussian and the width is obtained. This is done for several mass points. Figure 8·3 plots σ vs mass for data and MC. The data and MC distributions are then fitted with first order polynomial.The parameters for the fits obtained for data and MC are listed in Table 8.4.

Sample	par[0] (GeV)	par[1]
Data	8.72	0.02
MC	6.48	0.02

Table 8.4: Parameters for the fit from figure 8·3.

Next the ratio of the width for data and MC is obtained as a function of the invariant mass $M_{ee/\gamma\gamma}$ of the two EM objects using the equation:

$$R = \frac{8.72\text{GeV} + M_{ee/\gamma\gamma}\text{GeV} \times 0.02}{6.48\text{GeV} + M_{ee/\gamma\gamma}\text{GeV} \times 0.02}. \tag{8.3}$$

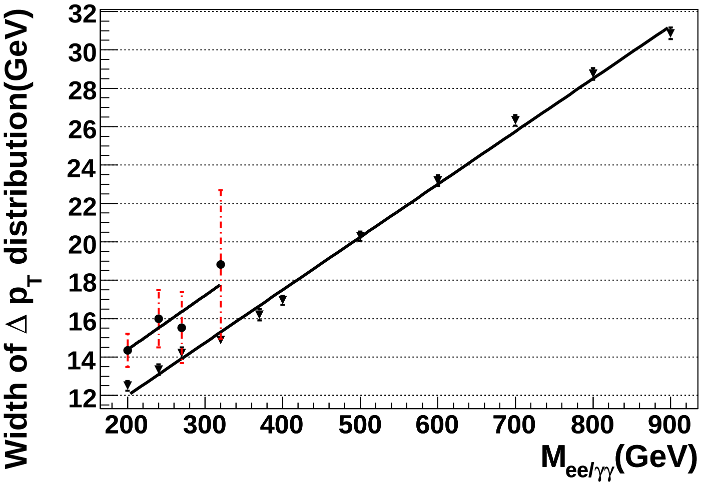

Figure 8·3: Width of the Δp_T distribution for data(circle) and MC(triangle).

Next, the mass window applied to get the signal efficiency for a given graviton mass is reduced by the corresponding factor R and the signal efficiency for the reduced mass window is obtained. The fractional error is calculated as $\Delta\epsilon/\epsilon$, where $\Delta\epsilon$ is the change in efficiency when the width of the mass window is changed.

The values for R and $\Delta\epsilon/\epsilon$ for the different graviton masses are listed in Table 8.5. For each graviton mass value the uncertainty from this table is used in the limit setting procedure.

8.3 EM ID uncertainty

This uncertainty originates from the difference in electron/photon identification efficiency between data and MC. The tag and probe method is used to get the ID efficiency for data. First events with two electromagnetic objects are selected. Then we require that the tag object passes all the cuts which are defined in section 5.1. In addition to these cuts, the tag object is also required to have a track match. The other object we probe, passed the following set of cuts:

Graviton Mass (GeV)	R	$\Delta\epsilon/\epsilon$ %
200	1.20	9.6
220	1.19	9.8
240	1.19	10.9
250	1.18	11.1
270	1.18	4.7
300	1.17	5.1
320	1.16	5.6
350	1.16	6.4
370	1.15	6.3
400	1.15	6.8
450	1.14	4.6
500	1.13	1.4
550	1.13	2.3
600	1.12	1.5
650	1.12	1.6
700	1.11	1.1
750	1.11	1.3
800	1.10	1.1
850	1.10	1.0
900	1.10	1.3
950	1.09	0.8

Table 8.5: Error on signal efficiency due to resolution.

- Loose cut for probe object
  - ID = 10 or 11
  - detector $|\eta| < 1.1$
  - $p_T > 25$ GeV
  - fraction of energy in electromagnetic calorimeter $f_{EM} > 0.9$
  - fraction of energy in isolation cone $f_{iso} < 0.2$

Counting the number of events with $85 < m(ee) < 100$ GeV gives the number of Z events with loose cuts on the probe electron N_{loose}. Next, all the selection cuts for electromagnetic showers defined in section 5.1 are applied on the probe electron to determine

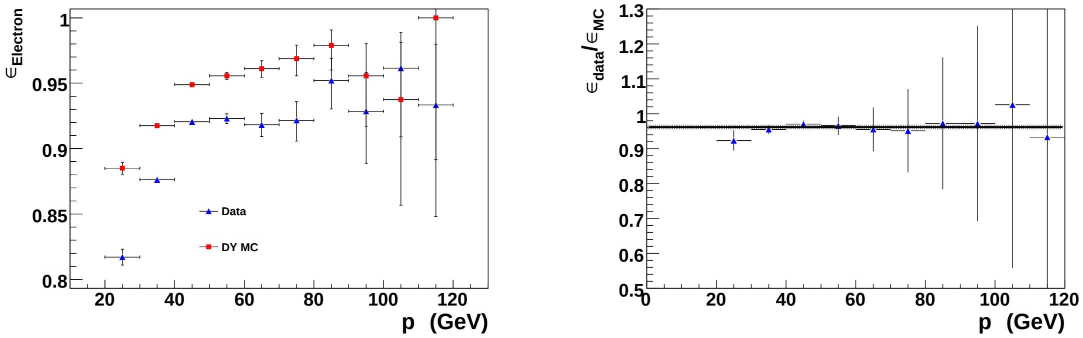

Figure 8·4: Comparison of electron efficiencies vs p_T for MC and data in CC. The left plot shows the ratio of data and MC efficiencies as a function of p_T. The line is a fit to a constant.

the number of Z events with selection cuts on the probe electron N_{sel} in exactly the same way. The electron ID efficiency is then given by

$$\epsilon_{ID} = \frac{N_{sel}}{N_{loose}}. \tag{8.4}$$

Exactly the same procedure is followed to get the efficiency for Drell-Yan MC sample. Then the electron ID efficiency is plotted as a function of p_T for both Data and MC (Figure 8·4). This shows the difference in the EM ID efficiency between data and MC. We fit the ratio of the EM ID efficiency for Data and MC to a constant. The value obtained from this fit is $r = 0.961 \pm 0.007$. The event efficiency is corrected by a factor of r^2. We quote a total EM object uncertainty of 1.4%.

8.4 Statistical uncertainties in MC and control data samples

The statistical uncertainty in the signal efficiency ϵ_{total} is given by

$$\delta_\epsilon = \sqrt{\frac{\epsilon_{total} \times (1 - \epsilon_{total})}{N_{total}}}, \tag{8.5}$$

where N_{total} is the total number of signal Monte Carlo events for a given graviton mass. This uncertainty is small (about 0.5%) and can be neglected.

The statistical uncertainty on the number of predicted background events is obtained for each mass window by propagating the statistical error in the DY, $\gamma\gamma$ and misidentification background distributions. The results for the different mass points are listed in Table 8.6.

Graviton Mass (GeV)	Total background	Statistical Error on total background	Relative uncertainty %
200	83.84	2.12	2.53
220	52.38	1.76	3.37
240	37.12	1.72	4.64
250	30.13	1.54	5.13
270	44.03	1.97	4.48
300	26.94	1.65	6.15
320	18.32	0.96	5.25
350	11.40	0.41	3.59
370	8.76	0.36	4.11
400	5.89	0.28	4.91
450	4.89	0.26	5.50
500	5.33	0.84	15.7
550	3.31	0.82	24.7
600	1.84	0.069	3.78
650	1.04	0.056	5.39
700	0.84	0.049	5.86
750	0.51	0.019	3.80
800	0.32	0.015	4.75
850	0.18	0.011	6.45
900	0.108	0.0088	8.18
950	0.059	0.0065	10.9

Table 8.6: Background statistical uncertainty.

8.5 Mass dependence of k-factor

To get the NLO cross-section, a mass independent k-factor of 1.34(41) is used. However, the k-factor is not exactly mass independent and hence, it is a source of uncertainty. Figure 8·5 shows the mass dependence of k-factor at next-to-leading order(35). We assign an uncertainty due to the mass dependence of the k-factor based on the difference between the massindependent value used and the NLO value for the k-factor. With an error band

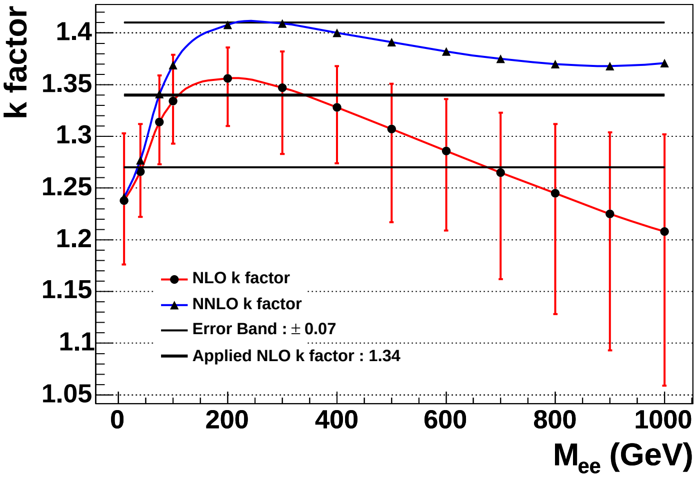

Figure 8·5: Mass dependence of k-factor(35).

of ±0.07 around 1.34, the uncertainty on the k-factor due to mass dependence is 5.2%.

8.6 Proton structure uncertainty

The parton distribution function (pdf) uncertainty is calculated by using the pdf reweight procedure as described in Ref.(36). For the CTEQ6.1M pdf set(37), a central pdf set and 2×20 sets of error pdfs are provided. The advantage of this method is, generating MC samples for the different pdfs is not required. Instead, for each error pdf, a weight is applied. A standard DØ program is used (38) for this study which provides the weight. The general method of calculating the pdf uncertainty for a given observable is explained below. For this analysis, the observables are efficiency and cross-section.

- The value of a given observable is obtained for the LO pdf (CTEQ6L1)(39) - A.
- The value of the observable for the NLO (CTEQ6.1M) central pdf is obtained - B.
- The value of the observable for the i=1-40 (2×20) error pdfs is obtained - B_i
- The deviation is calculated - $B - B_i$

- the positive error δ^{+}_{pdf} is the sum in quadrature of all positive deviations $(B - B_i) > 0$ scaled to the value of the LO observable:

  $$\delta^{+}_{pdf} = \frac{A}{B} \times \sqrt{\sum_i (B - B_i)^2},$$

  where the sum runs only over the positive deviations.

- the negative error δ^{-}_{pdf} is calculated similarly, except that the sum now runs only over the negative deviations.

The final result is quoted as $A + \delta^{+}_{pdf} - \delta^{-}_{pdf}$. In this analysis, following the method described above, the pdf uncertainty was calculated for the signal efficiency and the direct diphoton and Drell-Yan cross-section.

Signal efficiency uncertainty due to pdf

To define the efficiency ϵ_{pdf} for a given error pdf we define the subset $\mathbf{X}$ of all event indices $i \in [1, ..., N]$ for which the event passes the selection cuts. Then

$$\epsilon_{pdf} = \frac{\sum_{i \in X} W_i^{pdf}}{\sum_{i=1}^{N} W_i^{pdf}}.$$

Here W_i^{pdf} is the weight of event i for a given error pdf. The signal efficiency uncertainty due to pdf for different graviton masses is listed in Table 8.7. For the limit calculation, a mass dependent uncertainty on the efficiency due to the pdfs, is used and for each graviton mass, the larger of the two errors (positive or negative) is taken.

Uncertainty on cross-section due to pdf

The cross-section was obtained from the mean value of the root tuple for each MC sample. The cross section for the irreducible background of Drell-Yan and diphoton production for a given error pdf is given by:

$$\sigma_{pdf} = \sigma^0 \frac{\sum_{i=1}^{N} W_i^{pdf}}{\sum_{i=1}^{N} W_i^0}$$

RS Graviton Mass (GeV)	Positive error %	Negative error %
200	4.6	5.2
220	4.7	5.1
240	4.6	5.2
250	3.7	4.4
270	4.5	5.5
300	3.1	3.9
320	4.2	5.3
350	2.9	3.7
370	3.4	4.4
400	3.4	4.4
450	2.8	3.9
500	1.6	2.3
550	1.5	2.0
600	1.7	2.7
650	1.3	2.1
700	1.1	1.8
750	1.1	2.1
800	1.0	2.1
850	0.5	1.1
900	0.7	1.8
950	0.2	0.2

Table 8.7: Uncertainty (positive and negative) of signal efficiency due to pdf for different graviton mass.

.

Here W_i^0 is the weight of event i with the reference pdf set and σ^0 is the cross section for the reference pdf. The sum i runs over the N events in the MC sample. Finally the central value and the positive and negative error on the cross-section ($\sigma + \delta^+ - \delta^-$) is obtained for each of the Drell-Yan and diphoton MC samples. The central value and their corresponding errors for the different MC samples are listed in Table 8.8.

For this analysis, the uncertainty comes from the relative normalization of the cross-sections for the DY and diphoton samples which may vary with pdf choice. The ratio of the cross-sections for the different samples are calculated for four different combinations and then the relative error is calculated. The numbers are summarized in Table 8.9. In this

MC Sample	MassWindow (GeV)	Cross-Section(NLO) (pb)	δ^{+} (pb)	δ^{-} (pb)
DY	60-130	238.5	8.0	8.7
	130-250	1.74	0.060	0.064
	250-500	0.14	0.0064	0.0065
	>500	0.0060	0.00034	0.00043
$\gamma\gamma$	50-130	57.2	2.19	2.64
	130-250	4.1	0.18	0.20
	250-500	0.65	0.031	0.031
	>500	0.455	0.026	0.032

Table 8.8: NLO cross-section with error (due to PDF) for the DY and $\gamma\gamma$ MC samples.

Mass Window (GeV)	$\frac{\sigma_{DY}}{\sigma_{\gamma\gamma}}$	$\frac{\sigma^{+}_{DY}}{\sigma^{-}_{\gamma\gamma}}$	$\frac{\sigma^{-}_{DY}}{\sigma^{+}_{\gamma\gamma}}$	Error (%)
60-130	4.16	4.51	3.86	15.6
130-250	0.42	0.45	0.39	14.2
250-500	0.21	0.24	0.20	19.0
>500	0.013	0.014	0.011	22

Table 8.9: Ratio of DY and diphoton cross-section.

table we define $\sigma_{DY}+\delta^{+}_{DY}=\sigma^{+}_{DY}$, $\sigma_{DY}-\delta^{-}_{DY}=\sigma^{-}_{DY}$, $\sigma_{\gamma\gamma}+\delta^{+}_{\gamma\gamma}=\sigma^{+}_{\gamma\gamma}$ and $\sigma_{\gamma\gamma}-\delta^{-}_{\gamma\gamma}=\sigma^{-}_{\gamma\gamma}$. We make the conservative assumption that the two cross sections vary in a completely anticorrelated way with the pdfs. To estimate the effect of this variation, the k-factor for diphoton prediction is varied by ±20% from the actual value used (k=1.34) and the corresponding change in the total number of predicted background events is calculated. The relative change in the total background for the different k-factor is used as an uncertainty (Table 8.10).

Graviton Mass (GeV)	Total background (k=1.34)	Total background (k=1.61)	Total background (k=1.07)	$\Delta b/b$ %
200	83.8	86.2	81.39	2.9
300	26.9	28.3	25.5	5.2
400	5.89	6.31	5.47	7.1
500	5.33	5.68	4.98	6.5
600	1.84	2.00	1.68	8.6
700	0.84	0.90	0.77	7.1
800	0.32	0.35	0.29	9.3
900	0.108	0.117	0.098	8.3

Table 8.10: Change in total number of predicted background events for different k-factor for diphoton.

Chapter 9

CROSS CHECKS

As described in this thesis, while selecting events we did not distinguish between electrons and photons. This was done with an aim to have better sensitivity. As a cross-check, we also looked at the di-electron (ee) and di-photon ($\gamma\gamma$) channels separately. This was done by dividing the selected events, with the cuts as described in section 5.1, into three different samples. They were

- events with 2 electrons
- events with 2 photons
- events with 1 electron and 1 photon

The photons and electrons were distinguished by applying a spatial track match cut (section 3.3). The electrons, being charged particles, are expected to have a track in the tracking system of the detector and the photons, being neutral particles, are not expected to have any track. The background for the ee and $\gamma\gamma$ channels was estimated following the method described in chapter 6. Figure 9·3 and 9·6 show the full mass spectra for data, the total background and the misidentification background contributions in ee and $\gamma\gamma$ channels respectively.

Next, the limits for ee and $\gamma\gamma$ channels were calculated following the same method described in chapter 7. The results are listed in Table 9.1 and 9.2. Figure 9·7 and 9·8 show the 95% confidence level upper limit on $\sigma(p\overline{p} \rightarrow G + X) \times B(G \rightarrow e^+e^-)$ versus the graviton mass compared to the theoretical prediction for ee and $\gamma\gamma$ channels respectively. Figure 9·9 shows the contour exclusion plot for these two channels.

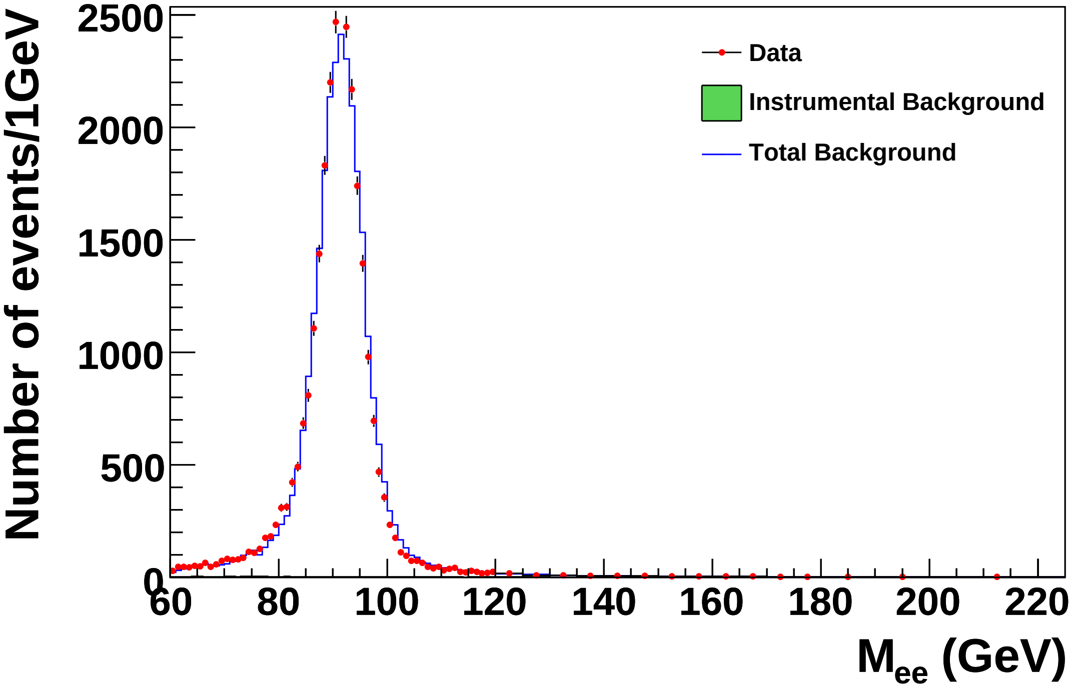

Figure 9·1: Invariant mass spectrum from data (points) with the fitted total background shape (open histogram) and the fitted c ontribution from misidentification backgrounds (shaded histogram) superimposed for ee channel.

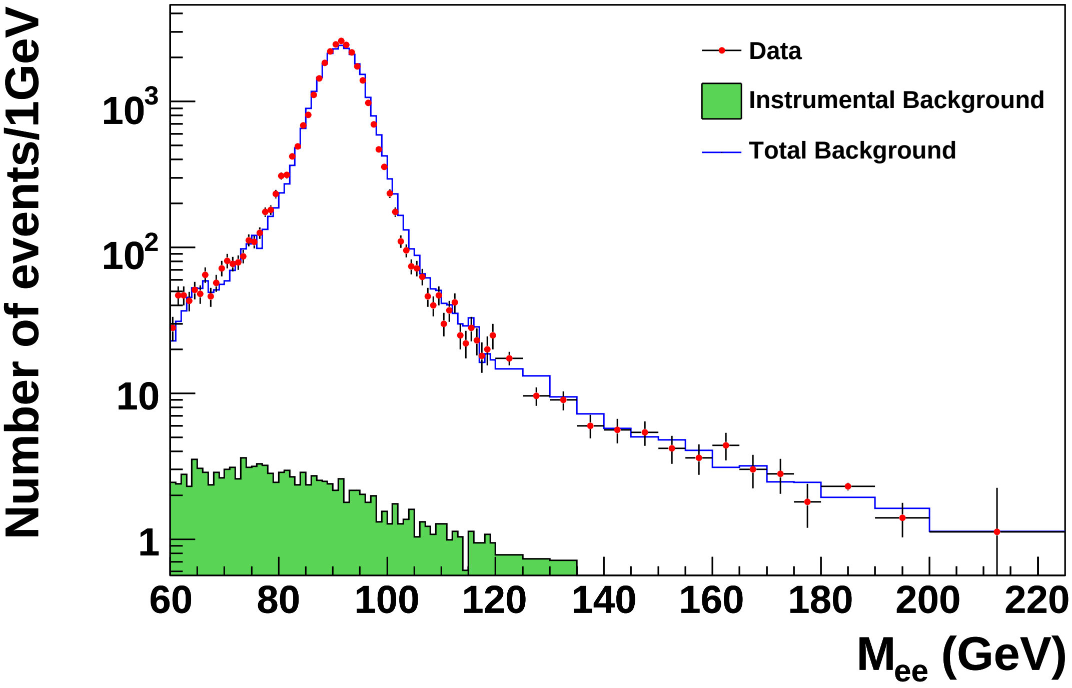

Figure 9·2: Invariant mass spectrum from data (points) with the fitted total background shape (open histogram) and the fitted c ontribution from misidentification backgrounds (shaded histogram) superimposed for ee channel.

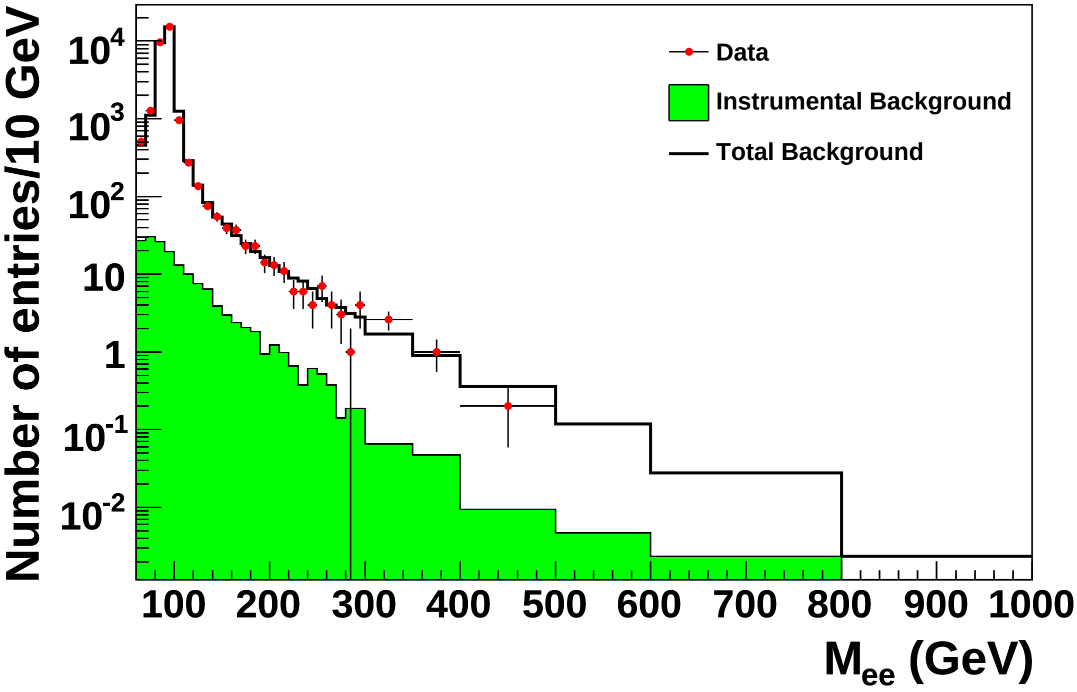

Figure 9·3: Invariant mass spectrum from collider data (points) with expected total background (open line histogram) and miside ntification background (shaded histogram) superimposed for ee channel.

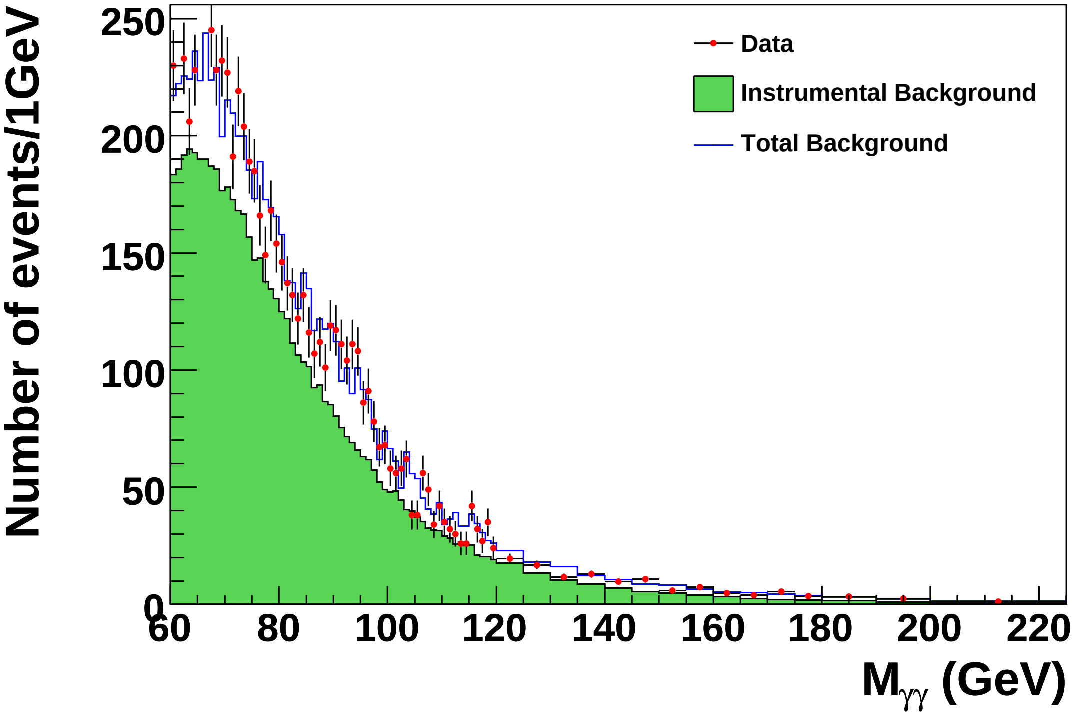

Figure 9·4: Invariant mass spectrum from data (points) with the fitted total background shape (open histogram) and the fitted c ontribution from misidentification backgrounds (shaded histogram) superimposed for $\gamma\gamma$ channel.

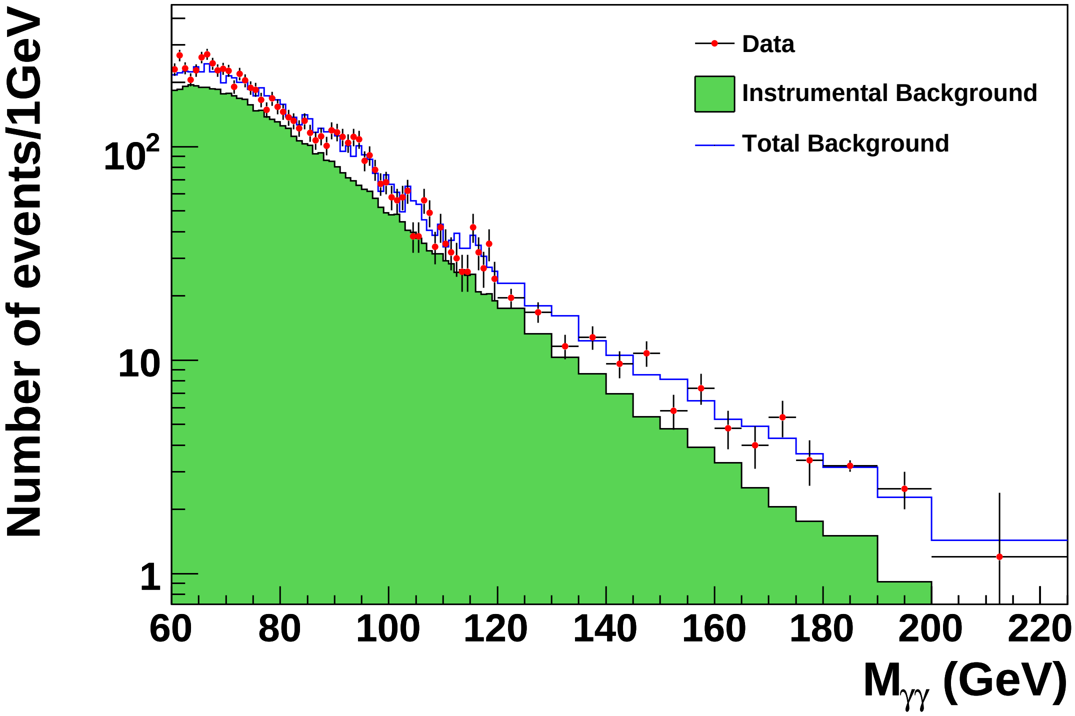

Figure 9·5: Invariant mass spectrum from data (points) with the fitted total background shape (open histogram) and the fitted c ontribution from misidentification backgrounds (shaded histogram) superimposed for $\gamma\gamma$ channel.

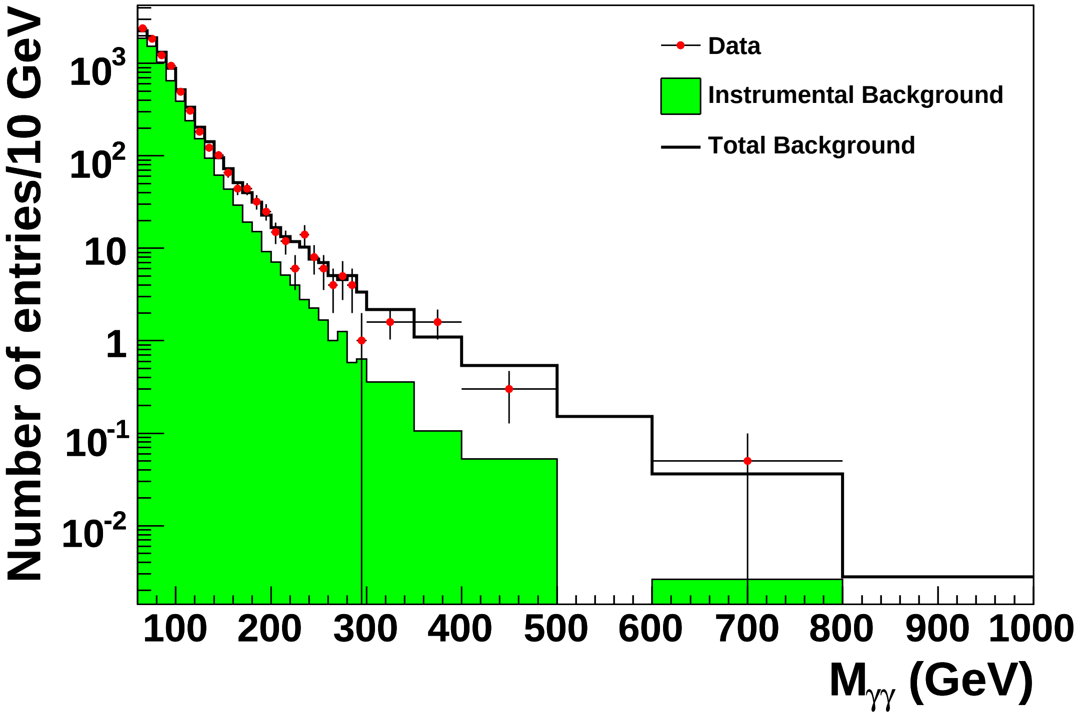

Figure 9·6: Invariant mass spectrum from collider data (points) with expected total background (open line histogram) and miside ntification background (shaded histogram) superimposed for $\gamma\gamma$ channel.

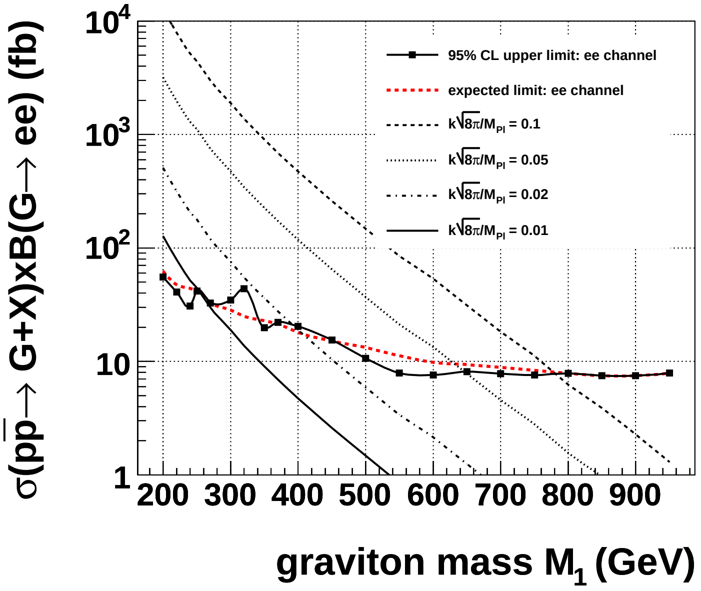

Figure 9·7: 95% confidence level upper limit on $\sigma(\overline{p} \rightarrow G + X) \times B(G \rightarrow e^+e^-)$ from $1\ \text{fb}^{-1}$ of data compared with the sensitivity and the theoretical predictions for different couplings $\kappa/\overline{M}_{Pl}$ for ee channel.

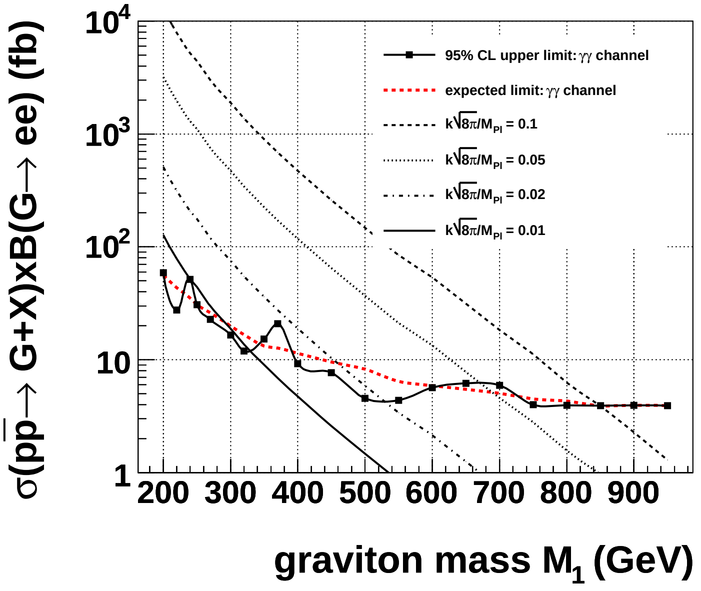

Figure 9·8: 95% confidence level upper limit on $\sigma(\overline{p} \rightarrow G + X) \times B(G \rightarrow e^+e^-)$ from 1 fb^{-1} of data compared with the sensitivity and the theoretical predictions for different couplings $\kappa/\overline{M}_{Pl}$ for $\gamma\gamma$ channel.

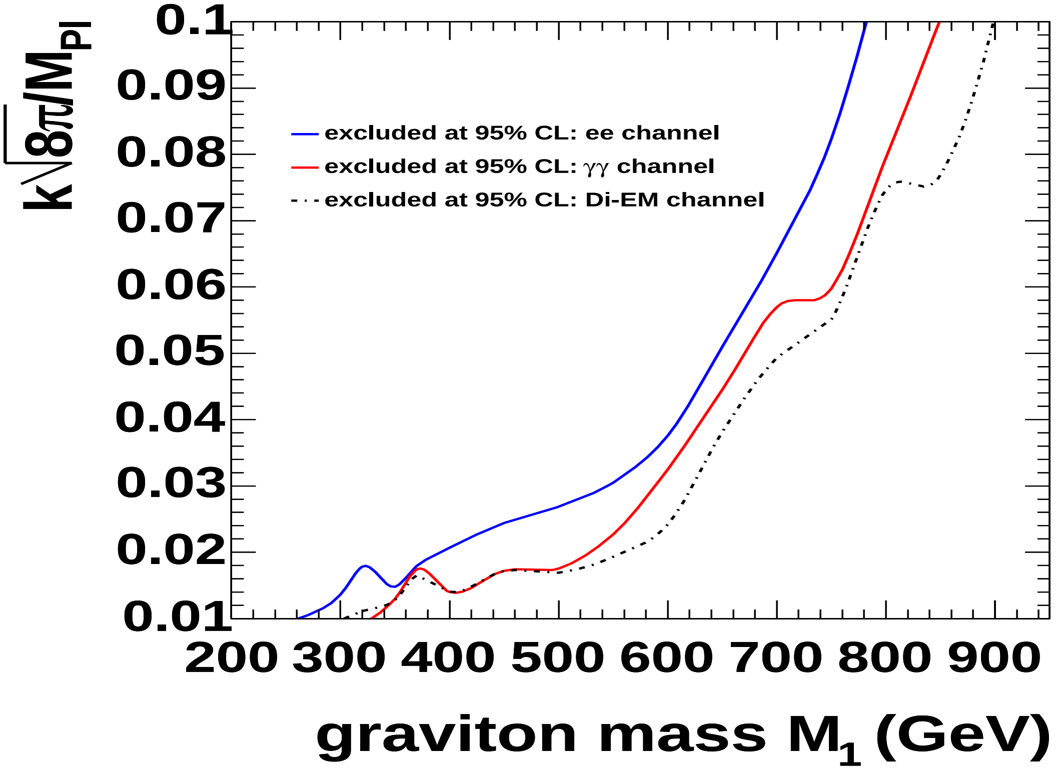

Figure 9·9: 95% confidence level upper limit on $\kappa/\overline{M}_{Pl}$ versus graviton mass exclusion contour for the di-electron channel, di-photon channel and di-em channel (my analysis).

Mass (GeV)	Mass Window (GeV)	Data	Total Background	ϵ_{Total} for signal	Cross Section (fb)			Coupling	
					theory	expected limit	observed limit	expected limit	observed limit
200	190-210	27	29.1±2.5	0.081±0.008	12730	62.5	55.4	0.0070	0.0066
220	210-230	17	19.7±1.8	0.085±0.009	7861	47.3	40.7	0.0077	0.0072
240	230-250	10	14.6±1.4	0.081±0.009	5181	43.8	30.8	0.0092	0.0077
250	240-260	11	11.3±1.1	0.078±0.009	4417	41.7	41.7	0.0097	0.0097
270	250-290	15	15.6±1.5	0.109±0.008	2988	32.7	32.7	0.0104	0.0104
300	280-320	12	10.0±1.1	0.110±0.007	1885	28.3	34.7	0.0122	0.0135
320	300-340	12	7.3±0.81	0.106±0.008	1371	24.9	43.7	0.0134	0.0178
350	330-370	4	4.8±0.51	0.105±0.007	902	22.8	19.8	0.0158	0.0148
370	350-390	4	3.8±0.42	0.102±0.007	688	21.4	22.1	0.0176	0.0179
400	380-420	3	2.4±0.28	0.106±0.008	473	17.9	20.3	0.0194	0.0207
450	420-480	2	1.99±0.23	0.117±0.007	259	15.1	15.4	0.0241	0.0244
500	450-550	1	2.02±0.38	0.133±0.004	147	13.2	10.6	0.0299	0.0269
550	500-600	0	1.18±0.31	0.140±0.004	84.9	11.2	7.9	0.0363	0.0305
600	540-660	0	0.86±0.10	0.146±0.004	53.6	9.7	7.5	0.0427	0.0376
650	590-710	0	0.51±0.06	0.136±0.004	31.3	9.3	8.1	0.0547	0.0510
700	620-780	0	0.42±0.05	0.142±0.003	18.3	8.8	7.7	0.0695	0.0651
750	660-840	0	0.24±0.02	0.146±0.004	11.2	8.3	7.5	0.0864	0.0823
800	700-900	0	0.16±0.02	0.141±0.003	6.2	7.8	7.8	0.1119	0.1119
850	750-950	0	0.086±0.011	0.148±0.003	3.9	7.4	7.4	0.1385	0.1385
900	790-1010	0	0.053±0.007	0.148±0.003	2.3	7.4	7.4	0.1810	0.1810
950	840-1060	0	0.029±0.004	0.140±0.002	1.3	7.8	7.8	0.2468	0.2468

Table 9.1: Number of expected and observed events in different mass windows, signal acceptance and upper limit on cross section × branching ratio for ee channel.

The most recent CDF result is based on analysing over 1fb^{-1} data in di-electron final state. Figure 9·10 shows the exclusion contour plot from the most recent CDF result(40). As summarized in Table 9.3, the observed CDF limits are comparable to our observed limits for the di-electron and di-photon channels. The CDF final result is quoted combining the di-electron and di-photon channels and excludes a graviton mass upto 889(267) at 95% confidence level for $\kappa/\overline{M}_{Pl} = 0.1(0.01)$.

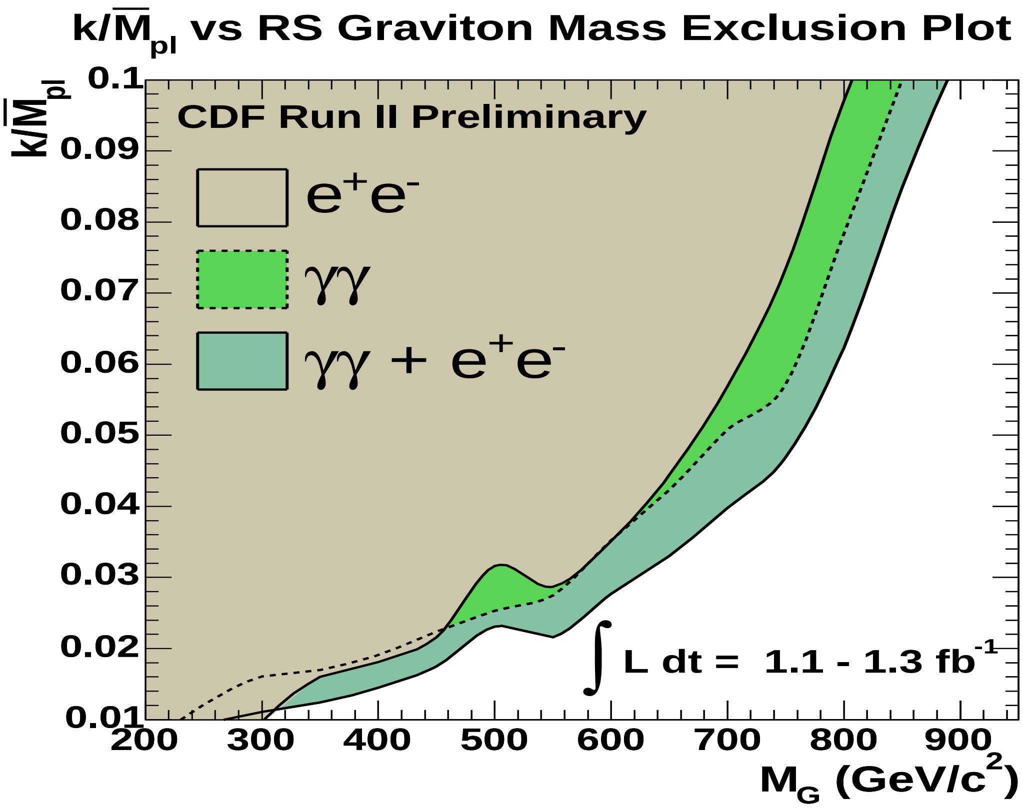

Figure 9·10: 95% confidence level upper limit on $\kappa/\overline{M}_{Pl}$ versus graviton mass exclusion contour from CDF(40).

Mass (GeV)	Mass Window (GeV)	Data	Total Background	ϵ_{Total} for signal	Cross Section (fb)			Coupling	
					theory	expected limit	observed limit	expected limit	observed limit
200	190-210	40	39.5±3.4	0.104±0.011	12730	56.0	58.8	0.0066	0.0068
220	210-230	18	25.1±2.2	0.109±0.012	7861	43.4	27.5	0.0074	0.0059
240	230-250	22	17.8±1.7	0.109±0.013	5181	35.2	51.4	0.0082	0.0099
250	240-260	14	14.6±1.5	0.116±0.013	4417	30.7	30.7	0.0083	0.0083
270	250-290	19	21.7±2.2	0.160±0.011	2988	26.1	22.7	0.0093	0.0087
300	280-320	11	13.9±1.5	0.167±0.010	1885	19.8	16.5	0.0102	0.0093
320	300-340	6	9.2±1.01	0.177±0.013	1371	16.6	11.9	0.0110	0.0093
350	330-370	6	5.8±0.61	0.170±0.012	902	13.2	15.2	0.0121	0.0130
370	350-390	8	4.4±0.49	0.182±0.014	688	12.6	20.8	0.0135	0.0174
400	380-420	2	3.1±0.36	0.180±0.014	473	11.4	9.2	0.0155	0.0139
450	420-480	2	3.19±0.38	0.214±0.013	259	9.5	7.6	0.0191	0.0172
500	450-550	0	2.8±0.54	0.243±0.007	147	8.2	4.5	0.0236	0.0175
550	500-600	0	1.51±0.40	0.253±0.008	84.9	6.4	4.3	0.0275	0.0227
600	540-660	1	1.19±0.14	0.264±0.008	53.6	5.9	5.6	0.0332	0.0325
650	590-710	1	0.67±0.08	0.254±0.007	31.3	5.4	6.2	0.0418	0.0445
700	620-780	1	0.55±0.06	0.269±0.006	18.3	5.0	5.9	0.0524	0.0569
750	660-840	0	0.33±0.04	0.277±0.007	11.2	4.4	3.9	0.0634	0.0598
800	700-900	0	0.21±0.02	0.280±0.007	6.2	4.3	3.9	0.0831	0.0794
850	750-950	0	0.12±0.01	0.282±0.005	3.9	3.9	3.9	0.1003	0.1003
900	790-1010	0	0.072±0.006	0.279±0.007	2.3	3.9	3.9	0.1318	0.1318
950	840-1060	0	0.037±0.004	0.281±0.004	1.3	3.9	3.9	0.1741	0.1741

Table 9.2: Number of expected and observed events in different mass windows, signal acceptance and upper limit on cross section × branching ratio for $\gamma\gamma$ channel.

Sample	Coupling	CDF observed limit (GeV)	DØ observed limit (GeV)
ee	0.01	302	260
	0.1	807	782
$\gamma\gamma$	0.01	230	328
	0.1	850	849

Table 9.3: Comparison of the observed limit from CDF and DØ for the ee and $\gamma\gamma$ channels.

Chapter 10

CONCLUSION

After analyzing 1 fb^{-1} data, I do not find any excess over standard model expectations and set mass limits on the lowest excited gravitons state of up to 898 GeV. The theory predicts the possible mass of the lowest excited state of such gravitons to be in between a few hundred GeV and a few TeV. Hence, if such gravitons excist, we still have the potential to find such gravitons analysing more data at the current experiment (Tevatron) as well as in the future experiments (LHC).

References

Chris Quigg. Gauge Theories of the Strong, Weak, and Electromagnetic Interactions. Addison-Wesley (1983).

Gordon L. Kane. Modern Elementary Particle Physics. Addison-Wesley. (1993) Updated Edition.

Peskin and Schroeder. An Introduction to Quantum Field Theory. Westview Press (1995).

S.L. Glashow, Nuclear Physics, **22**, 579 (1961); S. Weinberg, Physical Review Letters, **19**, 1264 (1967); A. Salam, Elementary Particle Theory, ed. N Svarholm (Almquist and Wiksells, Stockholm) p.367 (1969).

K. Riesselmann, "Limitations of a Standard Model Higgs Boson", hep-ph/9711456 (1997).

S. Dawson, hep-ph/9612229 (1997).

See, for example, Modern Kaluza-Klein Theories, edited by T. Appelquist, A. Chodos, and P. G. O. Freund, (Addison-Wesley, Reading, MA, 1987).

N. Arkani-Hamed, S. Dimopoulos and G. Dvali, Physics Letters B **429**, 263 (1998).

C. D. Hoyle *et al.*, "Submillimeter tests of gravitational inverse-square law", Physical Review D **70**, 042004 (2004).

S.Raychaudhuri, Pramana **55**: 171-182, (2000).

L. Randall and R. Sundrum, Physical Review Letters **83**, 3370 (1999); ibid., **83**, 4690 (1999).

T.Han *et al.*, Physical Review D **59**, 105006, (1999).

Talk by Santosh K. Rai, "Signals for RS-Gravitons at a linear electron-photon Collider", ILCWG Meeting, Indian Institute of Science, Bangalore, India (2002).

Kingman Cheung, hep-ph/0509028 (2004).

H. Davoudiasl, J.L. Hewett and T.G. Rizzo, Physical Review Letters **84**, 2080 (1999).

H. Davoudiasl, J.L. Hewett and T.G. Rizzo, Physical Review D **63**, 075004 (2001).

Tracey Pratt and Ray Culbertson, "Search for a High-Mass Diphoton State and Limits on Randall-Sundrum Gravitons at CDF", CDF Note 7098 (2004).

D0 Collaboration, V.M.Abazov *et al.*, Physical Review Letters **95**, 091801 (2005).

Joseph F. Kozminski, "Measurement of the ttbar Production Cross Section at sqrt(s)=1.96 TeV and Top Mass in the Dielectron Channel", Ph.D. Thesis (2005).

Ashish Kumar, " Measurement of ttbar Production Cross Section in the Dielecton Final States", Ph.D. Thesis (2005).

Prolay Mal, " Measurement of t-tbar cross section at sqrt(s)=1.96 TeV (e mu channel)", Ph.D. Thesis (2005).

Kevin M. Black, "A Precision Measurment of the Top Quark Mass", Ph.D. Thesis (2005).

James T. Linnemann, "The DØ Level 2 Trigger", International Journal of Modern Physics A (2000) `http://www.pa.msu.edu/hep/d0/ftp/l2/overview/dpf2000.pdf`.

D0 Collaboration. S. Abachi et. al., Nuclear Instruments and Methods in Physics Research A **338**, 185 (1994).

"The Upgraded D0 Detector", Fermilab-Pub-05/341-E (2005).

D. Chapin *et al.*, "Measurement of $Z \to e^+e^-$ and $W \to e^\pm\nu$ Production Cross Section Using One Tight Central Electron", DØ Note 4897 (2005).

T. Sjöstrand, L. Lönnbald, Pythia 6.2, hep-ph/0108264 (2001).

R. Brun and F. Carminati, CERN Program Library Long Writeup W5013 (1993).

J. Hays *et al.*, “Electron Trigger Efficiencies using Calorimeter Information in p17 Data”, DØ Note 5138 (2006).

O. Atramentov *et al.*, “Photon Identification in P17 Data”, DØ Note 4976 (2006).

Greg Landsberg and Konstantin T.Matchev, “Discovering a Light Higgs Boson with Light”, Fermilab-Pub-00/003-T, hep-ex/0001007 (2000).

I. Bertram, G.Landsberg, J. Linnemann, R.Partridge, M. Paterno and H.B. Prosper, “A Recipe for the Construction of Confidence Limits”, DØ Note 3476 (1998).

T. Sjöstrand, L. Lönnbald, Pythia 6.2, hep-ph/0108264 (2001).

H. Kim and J. Yu, “A Search for $Wb\bar{b}$ and WH Production in $p\bar{p}$ Collisions at $\sqrt{s} = 1.96$ TeV with Full Data Set of Pass2”, DØ Note 4706 (2006).

R. Hamberg, W. L. van Neerven, T. Matsuura, “A complete calculation of the order α_s^2 correction to the Drell-Yan K-factor”, Nuclear Physics B **359**, 343-405 (1991).

Volker Buescher *et al.*, “Conclusions of Mini-Workshop on PDF uncertainties and related topics”, DØ Note 4618 (2004).

Daniel Stump, Joey Huston, Jon Pumplin, Wu-Ki Tung, H. L. Lai, Steve Kuhlmann and J. F. Owens, Journal of High Energy Physics **0310**, 046 (2003).

Patrice Verdier and Kristian Harder, “PDF reweighting processor for CAF” (2006) `file:///d0dist/dist/packages/caf_pdfreweight/devel/doc/index.html`.

J. Pumplin, D.R. Stump, J. Huston, H.L. Lai, P. Nadolsky and W.K. Tung, Journal of High Energy Physics **0207** 012 (2002).

Joel Goldstein, Sam Harper and Peter Renton, “The Search for New Physics in High Mass Di-Electron Events in $p\overline{p}$ Collisions at $\sqrt{s}$=1.96 TeV”, CDF Note 8694 (2007).

P.Mathews, V. Ravindran, K. Sridhar, and W.L. van Neerven, Nuclear Physics B **713**, 333 (2005).

Greg Landsberg and Emmanuelle Perez, “Search for Randall-Sundrum Gravitons in the Dielectron and Diphoton Channel with 200 pb^{-1} of Data with the DØ Detector”, DØ Note 4533 (2004).

Curriculum Vitae

AMITABHA DAS

Office :
MS352 Fermilab
P.O. BOX 500
Batavia, IL 60510
Phone: (630) 840-2930
Email: adas@bu.edu

Home :
421 South Harvey Avenue
Apt. 18
Oak Park, IL 60302
Phone: (708) 267-4714

Education

- Ph.D., Physics, Boston University.
- M.S., Physics, Presidency College, University of Calcutta, India.
- B.S., Physics, Presidency College, University of Calcutta, India.

Research

- January 2002 - June 2007 : Graduate Research Assitant, Department of Physics, Boston University, Boston, MA.

    - As part of my thesis work, I performed a search for Randall-Sundrum graviton with 1fb^{-1} of data collected with DØ detector at Fermilab. This is done through graviton's decay to di-electron and di-photon final states.

    - While doing this analysis, I had good experience with event simulation and electromagnetic object identification.

- I was involved with the Silicon Track Trigger (STT) from its commissioning stage. STT is the custom electronics used in the DØ trigger system to provide real time identification of events having tracks consistent with the decay of b-flavored particles.

- Later, I became incharge of maintenance of part of the STT electronics, thus ensuring a smooth running of the STT.

- I took active part in the upgrade of STT during the 2006 shutdown. This involved hardware installation and testing the software to ensure proper running in Run2b.

- I was also involved with STT trigger studies.

Teaching Experience

- Teaching Assistant at Boston University, Fall 2001 (Undergraduate General Physics).

- Teaching Assistant at University of Oklahoma, Fall 1999 - Spring 2001 (Undergraduate General Physics and Advanced Physics Experiment).

Summer School

- Attended the XXXIV SLAC Summer Institute, held at Stanford Linear Accelerator Center (SLAC), Menlo Park, CA, USA from July 17 to July 24, 2006.

Computing & Software Experience

- Programming : C++, Root, Python, UNIX/LINUX shell programming.
- Word Processing : LaTex, Microsoft Word, EMACS.
- Platforms : Linux, Unix, Window.

Physics Outreach

- Did a number of undergraduate labs with high school students visiting the Physics department, as part of the LERNet program at Boston University.

Talk

- “Search for Randall-Sundrum gravitons with 1fb^{-1} of data” - Departmental Seminar, Boston University, November 2006.
- “Search for Randall-Sundrum gravitons with 1fb^{-1} of data” - Fermilab, Batavia, IL, February 2007.
- “Search for Randall-Sundrum gravitons with 1fb^{-1} of data” - APS April Meeting, Jacksonville, FL, April 2007.

Limited Authorship Paper

- “The DØ RunII Impact Parameter Trigger”, T.Adams *et. al.*, to be submitted to Nucl. Instr. and Methods.

Publications

- **"Search for Randall-Sundrum Gravitons in Dilepton and Diphoton Final States With 1 fb^{-1} od Data"**, A. Das, Doctoral Thesis, Boston University (to be submitted 2007).
- **"Direct observation of the strange b baryon Ξ_b^-"** V. M. Abazov *et al.*, [D0 Collaboration], FERMILAB-PUB-07-196-E(2007), Submitted to Physical Review Letters.
- **"Measurement of the ttbar production cross section in ppbar collisions using dilepton events"** V. M. Abazov *et al.*, [D0 Collaboration], FERMILAB-PUB-07-143-E(2007), Submitted to Physical Review D
- **"Search for third-generation leptoquarks in p anti-p collisions at s**(1/2) = 1.96-TeV"** V. M. Abazov *et al.*, [D0 Collaboration], FERMILAB-PUB-07-113-E(2007), Submitted to Physical Review Letters.
- **"Search for stopped gluinos from p-pbar collisions at sqrt(s)=1.96 TeV"** V. M. Abazov *et al.*, [D0 Collaboration], FERMILAB-PUB-07-100-E(2007), Submitted to Physical Review Letters.
- **"Measurement of the Lambda_b lifetime in the exclusive decay Lambda_b to J/psi Lambda"** V. M. Abazov *et al.*, [D0 Collaboration], FERMILAB-PUB-07-094-E(2007), Submitted to Physical Review Letters.
- **"Search for a Higgs boson produced in association with a Z boson in p anti-p collisions"** V. M. Abazov *et al.*, [D0 Collaboration], FERMILAB-PUB-07-076-E(2007), Submitted to Physics Letters B.
- **"Measurement of the branching fraction Br(B/s0 → D(s)(*) D(s)(*))"** V. M. Abazov *et al.*, [D0 Collaboration], FERMILAB-PUB-07-047-E(2007), Submitted to Physical Review Letters.